9-20-2018

Multi-Objective Drive-Cycle Based Design Optimization of Permanent Magnet Synchronous Machines

Philip Korta
University of Windsor

Recommended Citation

Korta, Philip, "Multi-Objective Drive-Cycle Based Design Optimization of Permanent Magnet Synchronous Machines" (2018). *Electronic Theses and Dissertations*. 7535.
https://scholar.uwindsor.ca/etd/7535

Multi-Objective Drive-Cycle Based Design Optimization of Permanent Magnet Synchronous Machines

By

Philip Korta

A Thesis
Submitted to the Faculty of Graduate Studies through the
Department of Electrical and Computer Engineering in Partial
Fulfillment of the Requirements for the Degree of Master
of Applied Science at the University of Windsor

Windsor, Ontario, Canada

2018

Multi-Objective Drive-Cycle Based Design Optimization of Permanent Magnet Synchronous Machines

by

Philip Korta

APPROVED BY:

B. Minaker
Department of Mechanical, Automotive & Materials Engineering

B. Balasingam
Department of Electrical and Computer Engineering

N. C. Kar, Advisor
Department of Electrical and Computer Engineering

August 30, 2018

DECLARATION OF ORIGINALITY

I hereby certify that I am the sole author of this thesis and that no part of this thesis has been published or submitted for publication.

I certify that, to the best of my knowledge, my thesis does not infringe upon anyoneôs copyright nor violate any proprietary rights and that any ideas, techniques, quotations, or any other material from the work of other people included in my thesis, published or otherwise, are fully acknowledged in accordance with the standard referencing practices. Furthermore, to the extent that I have included copyrighted material that surpasses the bounds of fair dealing within the meaning of the Canada Copyright Act, I certify that I have obtained a written permission from the copyright owner(s) to include such material(s) in my thesis and have included copies of such copyright clearances to my appendix.

I declare that this is a true copy of my thesis, including any final revisions, as approved by my thesis committee and the Graduate Studies office, and that this thesis has not been submitted for a higher degree to any other University or Institution.

ABSTRACT

Research conducted previously has shown that a battery electric vehicle (BEV) motor design incorporating drive-cycle optimization can lead to achievement of a higher torque density motor that consumes less energy over the drive-cycle in comparison to a conventionally designed motor. Such a motor indirectly extends the driving range of the BEV. Firstly, in this thesis, a vehicle dynamics model for a direct-drive machine and its associated vehicle parameters is implemented for the urban dynamometer driving schedule (UDDS) to derive loading data in terms of torque, speed, power, and energy. K-means clustering and Gaussian mixture modeling (GMM) are two clustering techniques used to reduce the number of machine operating points of the drive-cycle while preserving the characteristics of the entire cycle. These methods offer high computational efficiency and low computational time cost while optimizing an electric machine. Differential evolution (DE) is employed to optimize the baseline fractional slot concentrated winding (FSCW) surface permanent magnet synchronous machine (SPMSM). A computationally efficient finite element analysis (CEFEA) technique is developed to evaluate the machine at the representative drive-cycle points elicited from the clustering approaches. In addition, a steady-state thermal model is established to assess the electric motor temperature variation between optimization design candidates.

In an alternative application, the drive-cycle cluster points are utilized for a computationally efficient drive-cycle system simulation that examines the effects of inverter time harmonics on motor performance. The motor is parameterized and modeled in a PSIM motor-inverter simulation that determines the current excitation harmonics that are injected into the machine during drive-cycle operation. These current excitations are inserted into the finite element analysis motor simulation for accurate analysis of the harmonic effects. The analysis summarizes the benefits of high-frequency devices such as gallium nitride (GaN) in comparison to insulated gate bipolar transistors (IGBT) in terms of torque ripple and motor efficiency on a drive-cycle.

ACKNOWLEDGEMENTS

Firstly, I would like to thank my supervisor, Dr. Narayan Kar who guided me into and supported me throughout the masterôs program. He recognized my potential and gave me all the tools necessary to become an exceptional researcher. In addition, he provided me with an abundant amount of opportunities to attend technical conferences and meet with industries to gain confidence and help me grow as a professional in the field of electric vehicle applications.

I would like to thank Dr. Balakumar Balasingam who took the time to sit with me and have technical discussions. He provided me with many insights in the field of machine learning and clustering techniques. I would also like to acknowledge Dr. Bruce Minaker who provided me with feedback and motivated me to incorporate thermal analysis into my work.

I would also like to sincerely thank Dr. Lakshmi Varaha Iyer who mentored me throughout my masterôs program and guided me towards my research topics. He provided me with opportunities to work on novel and interesting topics and pushed me to accomplish things that I am proud of and would have never achieved otherwise.

I would also like to thank the entire CHARGE lab team, especially Ms. Himavarsha Dhulipati, Ms. Shruthi Mukundan, Dr. Aiswarya Balamurali, and Mr. Junxi Cai who selflessly helped me whenever I needed assistance. They taught me many core concepts in the field of electric machine design and control and made the duration of my masterôs enjoyable by being great friends.

TABLE OF CONTENTS

LIST OF TABLES

LIST OF FIGURES

LIST OF ABBREVIATIONS/SYMBOLS

BEV	Battery Electric Vehicle
DE	Differential Evolution
PMSM	Permanent Magnet Synchronous Machine
FEA	Finite Element Analysis
LPTN	Lumped Parameter Thermal Network
GaN	Gallium Nitride
IGBT	Insulated-Gate Bipolar Transistor
EV	Electric Vehicle
EPA	Environmental Protection Agency
UDDS	Urban Dynamometer Driving Schedule
HWFET	Highway Fuel Economy Driving Schedule
SSE	Sum of Squared Error
ECG	Energy Center of Gravity
GMM	Gaussian Mixture Modeling
EM	Expectation Maximization
MMDL	Mixture Minimum Description Length
CEFEA	Computationally Efficient Finite Element Analysis
FSCW	Fractional Slot Concentrated Winding
SPMSM	Surface Permanent Magnet Synchronous Machine
MTPA	Maximum Torque per Ampere
FW	Field/Flux Weakening
FEM	Finite Element Method
FFT	Fast Fourier Transform
PWM	Pulse-Width Modulation

NOMENCLATURE

F_D	Drag force
F_R	Tire friction force
F_A	Force of acceleration
F_G	Gravitational force
F_v	Resultant vehicle force
Ɉ	Chapter 2: Density of air
	Chapter 4: Resistivity of copper
C_d	Drag coefficient
A_v	Frontal vehicle surface area
f_{rr}	Coefficient of rolling resistance
M_v	Vehicle mass
v	Chapter 2: Speed in m/s
	Chapter 4: Harmonic order
g	Gravitational acceleration
Ŭ	Chapter 2: Road grade
	Chapter 3: Mixing probability or component distribution
r	Wheel radius
i_g	Gear ratio
T	Chapter 2: Torque
	Chapter 7: PI time constant
ɖ	Efficiency
N	Speed in rpm
P	Chapter 2: Power
	Chapter 4: Number of poles
	Chapter 6: Parent
	Chapter 7: PI gain
ɣ	Chapter 2: Speed in rad/sec
	Chapter 4: Specific core loss
E	Energy
S	Cluster of data points

m	Chapter 3: Clusterôs mean in K-means
	Chapter 4: Mass
µ	Gaussian mean
ů^{2}	Covariance
C	Covariance matrix
ɗ	Chapter 3: Parameter vector of a given component (µ$_{m}$, C_m)
	Chapter 4: Phase angle
	Chapter 5: Temperature
Ū$_{(K)}$	Parameter set defining a given mixture
ŭ$_{\mu}$	Stopping condition tolerance for Gaussian mean
ŭ$_{C}$	Stopping condition tolerance for Gaussian covariance matrix
A	Chapter 4: Magnetic vector potential
	Chapter 5: Isothermal surface area perpendicular to the direction of heat flow
ū	Radial flux per unit axial length for one turn of a coil placed around a stator tooth
ɚ	Flux linkage
◖$_{v}$	Harmonic phase angle
e_a	Back EMF
I	Current excitation
L	Motor length
V	Voltage
J	Current density
P_{Cu}	Copper loss
B	Flux density
t_w	Tooth width
y_w	Yoke width
k_h	Hysteresis loss coefficient
k_e	Eddy-current loss coefficient
f	Frequency
P_{Fe}	Core loss

P_{mech}	Mechanical loss
k_f	Viscous friction coefficient
c_m	Material cost index
H	Quantity of heat transferred
q	Heat transfer rate
k	Thermal conductivity of a medium
x	Direction of heat flow
h	Convective heat transfer coefficient
ů	Stefan-Boltzmann
Ů	Emissivity of a body
R_{th}	Thermal resistance
c_p	Specific heat capacity
C_{th}	Thermal capacitance
b_j^U, b_j^L	Upper and lower bounds of a design parameter
F	Mutation intensity
C_r	Crossover probability
c	Child
T_{coil}	Turns per coil
D_{ro}	Rotor outer diameter
W_t	Tooth width
W_{so}	Slot opening width
Ŭ$_{PM}$	Magnet angle
f_{sw}	Switching frequency
R_s	Phase resistance

CHAPTER 1

Introduction

Electric vehicles have captured a vast amount of attention in the past decade due to environmental concerns from fossil fuel emissions and the public's desire for innovation. Furthermore, auto manufacturers must meet government regulations to meet strict fuel efficiencies targets in next-generation vehicles [1], [2]. Permanent magnet synchronous machines (PMSMs) are currently leading the competition amongst other types of electric motors to replace the standard internal combustion engine due to their high power density and efficiency [3]. However, even as the most suitable electric machine, there is still opportunity to improve in areas of reliability, losses, temperature, size, cost, and active weight [4]. This is evident by the electric vehicle's requirements to be efficient over a wide speed operating range to obtain increased driving distance on a single battery charge and for the vehicle to be affordable for the mass population [5].

A PMSM uses permanent magnets in the rotor to create the field flux, which increases efficiency and reliability since contact brushes are not needed to supply an excitation to the rotor of the electric machine [6]. Figure 1.1 shows the torque and power characteristics of a typical PMSM. The constant torque region is obtainable until the rated speed of the machine where the maximum voltage is reached. In this region, the maximum torque is attainable by supplying rated current to the machine [7]. This torque characteristic is desirable for traction applications since maximum torque is most frequently required at low speeds for acceleration. Beyond rated speed, the air gap flux density is weakened to decrease the induced back electromotive force (BEMF), which in turns reduces the terminal voltage below the rated value. In this flux-weakening (FW) region, the power remains constant and the torque decreases as speed increases until maximum speed [8].

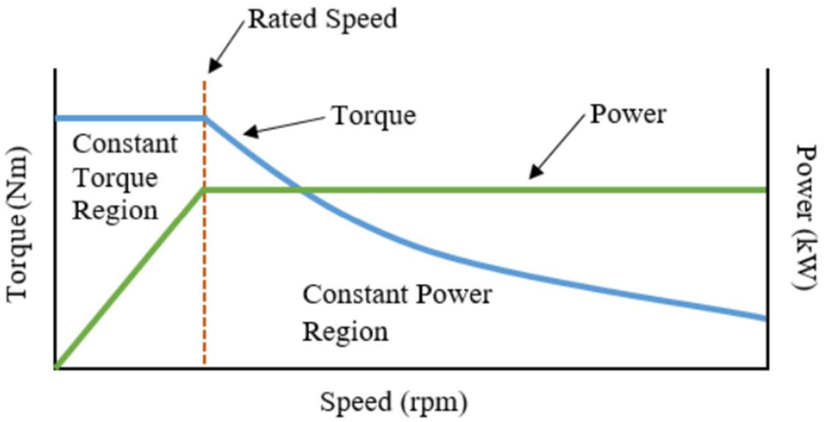

Fig. 1.1. Torque-speed and power-speed characteristics of a typical PMSM.

Although electric motors have been around for over a century, their use in traction applications for electric vehicles remains a modern and developing application that still requires a significant amount of research and development in terms of weight, cost, size, efficiency, reliability, and power density of the electric motor. This requires careful analysis of the electric vehicle to optimally design the electric motor for the specific application.

1.1 Objectives and Contributions of This Study

In electric motor design optimization procedures, the objective has commonly been to maximize the motor efficiency at rated conditions due to the computational demand of finite element analysis as in [9]. However, in a practical vehicle application, the motor performs at various torque and speed operating conditions while driving [10]. A PMSM is not able to deliver the peak efficiency across the entire operating range. Therefore, a new motor design procedure is required to evaluate machine performance across a wide range of operating conditions. This will ensure that an electric motor will perform with optimal efficiency in a practical vehicle application where it is subject to various torque and speed loading conditions.

Furthermore, many standard machine design procedures and simulations consider a pure sinusoidal current input as the motor excitation. In an actual implementation, an inverter that generates the three-phase power supply of the motor induces harmonics that affect the performance of the machine. These inverter-induced harmonics, named time harmonics, cause an increase in torque ripple and vibrations as well as additional harmonic losses [11]. Therefore, it is essential to model the inverter excitations that include harmonics to assess the negative effects that they have on the motor. Moreover, drive-cycle analysis is required to accurately evaluate the overall machine performance in a system that is prevalent in real driving conditions.

This thesis proposes modeling for torque, speed, and power characterization of the electric motor in a vehicle application. The vast amount of derived drive-cycle load points requires quantization by means of clustering or mixture modeling to make drive-cycle analysis computationally feasible by representing the entire cycle with a minimal number of load points.

Further, the thesis proposes a method to optimize an electric machine for this set of torque-speed load points that are most crucial for a given vehicle when executing a selected drive-cycle. This ensures that optimal motor energy efficiency will be obtained in a practical vehicle application. Additionally, a thermal analysis is included into the optimization to consider temperature variations in different motor topologies. Thereafter, to analyze the electric motor on a system level drive-cycle analysis, a performance comparison is introduced to rival the effects that different inverters have on an electric motor in terms of torque ripple and drive-cycle energy efficiency.

1.2 Organization of Thesis

Chapter 2 utilizes vehicle dynamic equations to analyze the forces experienced by a particular vehicle whilst performing a drive-cycle to derive torque, speed, and energy distribution experienced by the electric machine.

Chapter 3 focuses to reduce the computational burden that this vast amount of loading data contains by implementing machine learning algorithms such as K-means clustering and Gaussian mixture modeling to cluster and quantize the data. This will in turn produce a reduced number of representative points that retain the loading characteristics experienced by the machine across the drive-cycle.

Chapter 4 introduces an evaluation procedure to calculate the efficiency of the motor using an enhanced finite element analysis (FEA) technique to derive computationally efficient and accurate performance characteristics. This technique enables the continuous torque, back EMF, and flux density waveforms to be derived that contain nonlinearities such as harmonics and saturation by combining a limited number of FEA solutions with Fourier analysis to reconstruct the continuous waveforms. These characteristics are used in a loss model developed to determine the machine efficiency at a given operating condition.

Chapter 5 outlines the procedure for constructing a lumped parameter thermal network (LPTN) to analyze the temperatures of the machine at different locations in the motor structure. The model uses the losses calculated in Chapter 4 to determine the steady-state operating temperatures of the machine in different load conditions.

Chapter 6 introduces a multi-objective differential evolution optimization program that creates machine design candidates and evaluates the designs based on their performance across the drive-cycle representative load points. The evolutionary algorithm modifies the geometrical structure of the machine and converges to uncover models that are optimal in terms of cost, weight, torque ripple, and efficiency across the drive-cycle points. This ensures that the vehicle will operate with the lowest amount of energy consumption possible while satisfying stringent constraints on weight and torque ripple production.

Chapter 7 extends the research work to the system level by analyzing the effects of inverter-generated harmonics on an electric motor. Gallium nitride (GaN) and insulated-gate bipolar (IGBT) two-level inverter system simulations are created to obtain the current excitations with harmonic content at drive-cycle representative load points. FEA is used to analyze the inverter harmonic effects on the torque ripple and losses of the machine. A drive-cycle comparison of the GaN and IGBT inverter topologies with analytically calculated pure sinusoidal waveforms is conducted.

Chapter 8 summarizes the results and provides potential future work in this field of research.

CHAPTER 2

Vehicle Dynamics for Drive-Cycle Operating Characteristics

Vehicle dynamic simulations provide essential information to understand the torque and speed requirements of a motor while subject to different driving conditions [12]. The vehicle dynamic equations listed in (2.1) ï (2.4) analyze the forces that act on a vehicle in motion. The main forces can be analytically represented by the drag force associated with the aerodynamics of the vehicle and the extent of wind resistance the vehicle is experiencing, the static and dynamic tire friction force, the force of acceleration that is associated with the vehicleôs inertia, and the gravitational force that the vehicle experiences when there is a road grade present. The sum of these four forces describes the overall resultant force acting on the vehicle, expressed in (2.5) [13].

$$F_D = \frac{1}{2}\rho C_d A_v v^2 \tag{2.1}$$

$$F_R = f_{rr} M_v g \cos\alpha \tag{2.2}$$

$$F_A = M_v \frac{dv}{dt} \tag{2.3}$$

$$F_G = M_v g \sin\alpha \tag{2.4}$$

$$F_v = F_D + F_R + F_A + F_G \tag{2.5}$$

where Ɉ is the density of air, C_d is the drag coefficient, A_v is the frontal vehicle surface area, v is the vehicle speed, f_{rr} is the coefficient of rolling resistance, M_v is the vehicle mass, g is gravitational acceleration, and Ŭ is the road grade.

2.1 Drive-Cycles

Drive cycles are a series of data points that contain vehicle speed versus time. They are created to simulate real-life driving conditions and are most often used for performance assessment of an automobile in terms of vehicle mileage and emissions. Electric vehicles (EVs) do not generate emissions, but vehicle mileage is one of the principle design considerations since they are often restricted in energy storage capability because of the high battery cost, weight, and size.

The Environmental Protection Agency (EPA) developed the Urban Dynamometer Driving Schedule (UDDS) to simulate city driving and the Highway Fuel Economy Driving Schedule (HWFET) for highway driving [14]. Many other corporations and countries have various drive-cycles to represent common driving conditions as well as aggressive driving styles present in high traffic situations. They are used as a baseline for vehicle performance during prototype development to predict product functionality and lifespan once the vehicle enters the market. It is therefore essential that vehicle components be designed to withstand and perform most efficiently on suitable drive-cycles for specific vehicle applications. For this reason, the aforementioned vehicle dynamics are applied to a drive-cycle to analyze the forces acting on the vehicle and predict design targets, such as torque and speed requirements, to develop optimally efficient products for specific vehicle applications.

The UDDS and HWFET obtained from [14] are the standard tests conducted in Canada for city and highway evaluation of cars and light trucks. This thesis will focus specifically on the UDDS cycle to have a practical design target for vehicles in production in this area. The urban cycle displayed in Fig. 2.1 experiences a lower average speed of 34.1 km/h and 23 full stops. The cycle covers a total distance of 17.77 km over a duration of 1,874 seconds. The highway drive-cycle displayed in Fig. 2.2 has a higher average speed of 77.7 km/h, covering a total distance of 16.45 km, with a duration of 765 seconds [15].

2.2 Vehicle Parameters

In order to acquire machine design targets and analyze the loading conditions that the electric motor is subject to, vehicle parameters are required for which the electric motor will be integrated into. These vehicle parameters include the drag coefficient, frontal vehicle surface area, rolling resistance coefficient, vehicle mass, and wheel radius r_w. Other parameters required include the density of air, gravitational acceleration, and road grade, which are independent of the vehicle model selected. For this thesis, the 2014 Ford Fiesta is considered as the vehicle application for the electric motor design. All the corresponding vehicle parameters are listed in Table 2.1 [16].

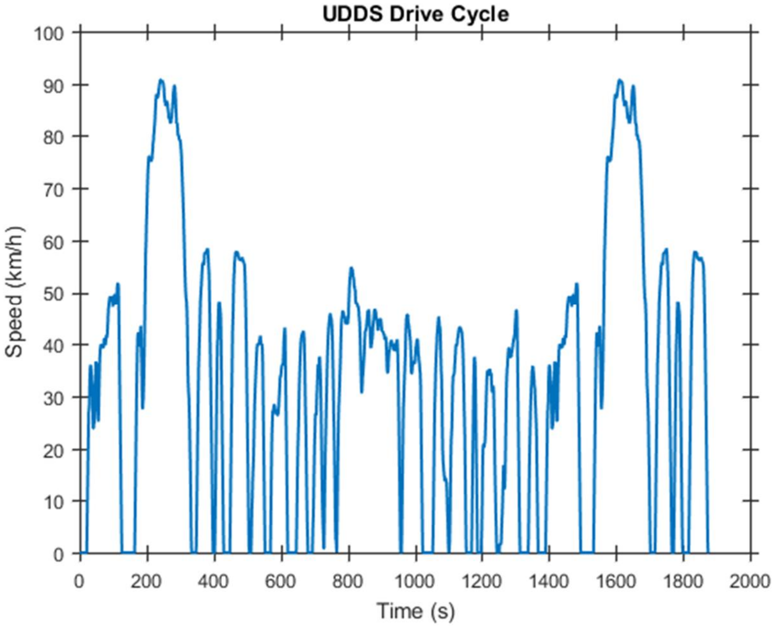

Fig. 2.1. Urban Dynamometer Driving Schedule (UDDS).

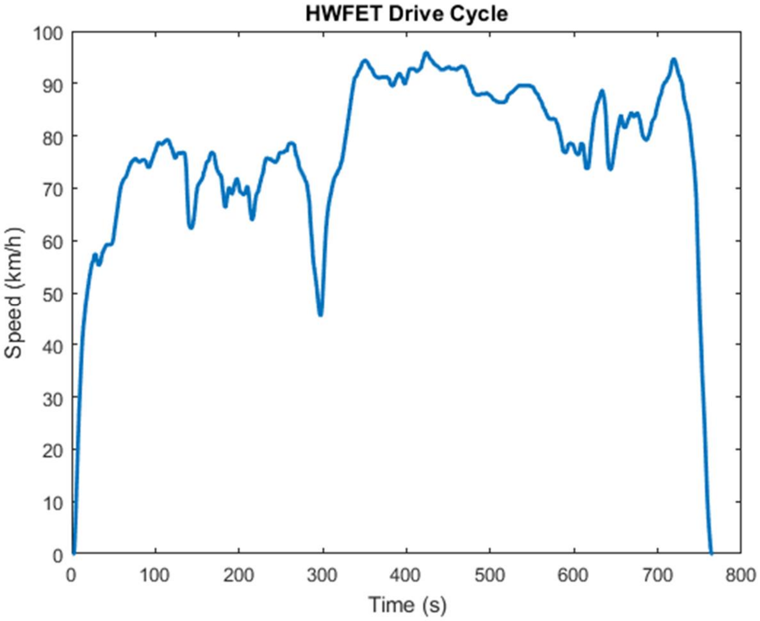

Fig. 2.2. Highway Fuel Economy Driving Schedule (HWFET).

2.3 Deriving Motor Load Characteristics with Vehicle Dynamics Model

The resultant vehicle force in (2.5) is obtained by calculating the individual forces at each discrete sample of the UDDS drive-cycle. The result can be seen in Fig. 2.3, which displays the change in vehicle force over the duration of the cycle.

TABLE 2.1

2014 Ford Fiesta Specifications

Symbol	**Description**	**Value**
Ɉ	Density of air	1.202 kg/m^3
C_d	Drag coefficient	0.33
A_v	Frontal vehicle surface area	2.536 m^2
v	Vehicle speed	varying
f_{rr}	Rolling resistance coefficient	0.013
M_v	Vehicle mass	1,570 kg
g	Gravitational acceleration	9.81 m/s^2
Ŭ	Road grade	0°
r_w	Wheel Radius (195/50R16)	0.3007 m
i_g	Gear Ratio	1

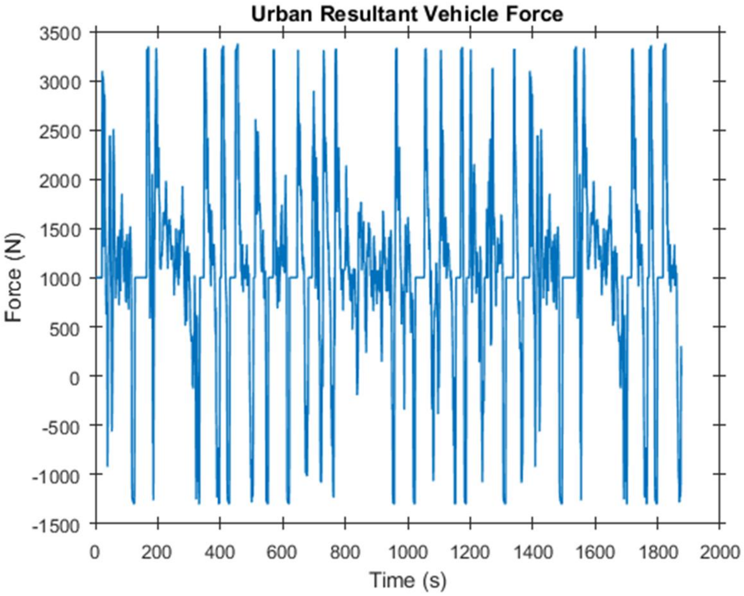

Fig. 2.3. UDDS resultant vehicle force for 2014 Ford Fiesta.

2.3.1 Motor Output Torque for UDDS Drive-Cycle

The vehicle force is applied at the wheel of the vehicle to drive the vehicle. However, the focus of this thesis is the motor, and thus, the resultant vehicle force must be translated back and converted into the output speed and torque of the electric motor. Equation (2.6) uses the resultant vehicle force and the moment arm of the wheel, shown in Fig. 2.4, to derive the torque T_w at the shaft of the vehicle [12].

$$T_w = F_v r_w \tag{2.6}$$

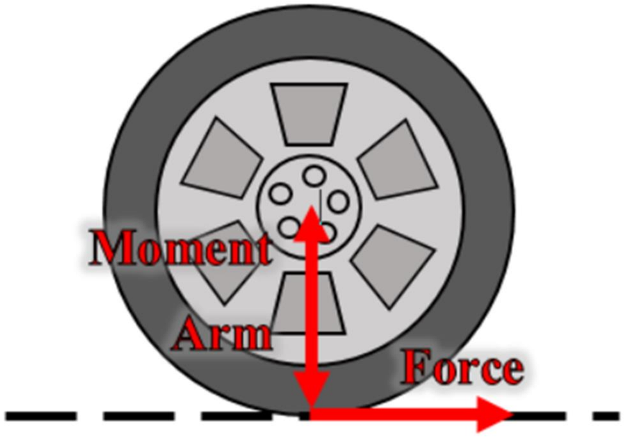

Fig. 2.4. Relationship between vehicle force and output torque.

The transmission system of an electric vehicle often includes a fixed gear ratio between the motor and the output shaft. This gear ratio is used to scale-down the amount of torque production and increase the speed required of the electric motor. The motor torque T_p is related to the torque at the wheel T_w as in (2.7) where i_g is the gear ratio and ɖ is the driveline efficiency [12]. The driveline efficiency includes all losses associated with the gears and the differential. A transmission system contributes losses that account for 2 ï 20% of the total output power in the vehicle depending on the operating speed and torque [17], [18]. Figure 2.5 illustrates the configuration of driveline components in a typical electric vehicle.

$$T_p = \frac{T_w}{i_g \eta} \tag{2.7}$$

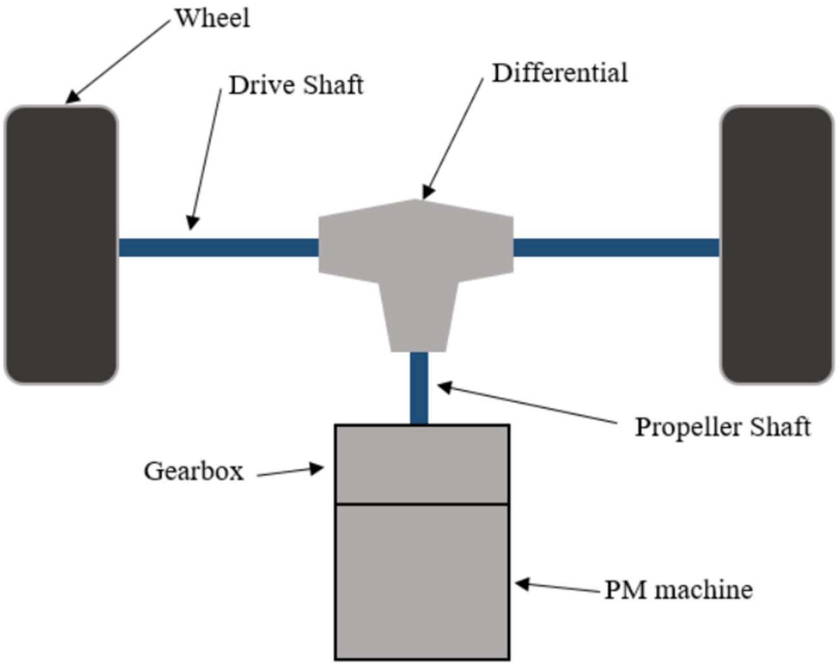

Fig. 2.5. Driveline components of a typical electric vehicle.

This thesis considers a direct-drive vehicle that has no gear ratio in the driveline. The direct-drive motor configuration requires a high-torque, low-speed machine since the motor torque and speed is directly transferred from the motor to the wheels of the vehicle. The direct-drive configuration is beneficial since it contains a lower component count, reduces the losses and noise, and has less maintenance and lubrication cost [19]. Consequently, this thesis considers a driveline efficiency of 98% since the gear ratio is removed from the driveline in a direct-drive machine, therefore reducing the losses. Figure 2.6 displays the output torque of the electric motor with the applied driveline efficiency and a gear ratio of one. Positive torque indicates that the vehicle is motoring to accelerate or drive at a consistent speed. Negative torque occurs when the vehicle is decelerating. In this scenario, the motor acts as a generator and is capable of capturing some of the energy to charge the battery through a process called regenerative braking.

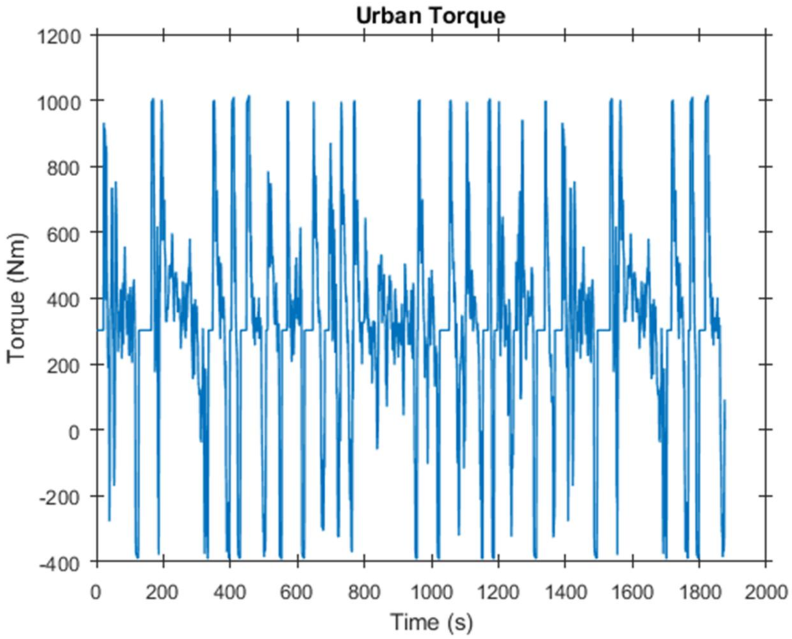

Fig. 2.6. UDDS torque profile for a direct-drive machine.

2.3.2 Motor Speed for UDDS Drive-Cycle

In addition, the output motor speed, N_p, is a function of the gear ratio and the wheel speed, N_w, as seen in (2.8). The wheel speed is converted from kilometers per hour to revolutions per minute using (2.9). Figure 2.7 displays the speed of the motor's rotor in revolutions per minute (rpm) [12].

$$N_p = i_g N_w \tag{2.8}$$

$$N_w = \frac{30v}{\pi r_w} \tag{2.9}$$

2.3.3 Motor Output Power for UDDS Drive-Cycle

The product of torque and speed in radians per second, ω, defines the instantaneous output power, P_{out}, of the electric motor as seen in (2.10) [13]. Figure 2.8 displays this characteristic across the urban drive-cycle. Similar to the torque profile, positive power flow denotes motoring and the negative regions display the magnitude of power that is available for regenerative braking. In this thesis, the electric machine is being analyzed for the motoring condition and only considers the positive torque and power regions.

$$P_{out} = T\omega \tag{2.10}$$

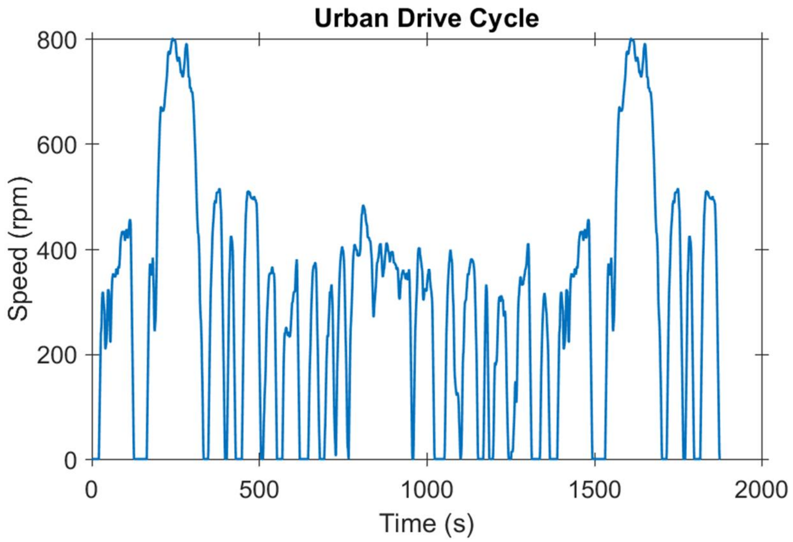

Fig. 2.7. UDDS motor speed in rpm for a direct-drive machine.

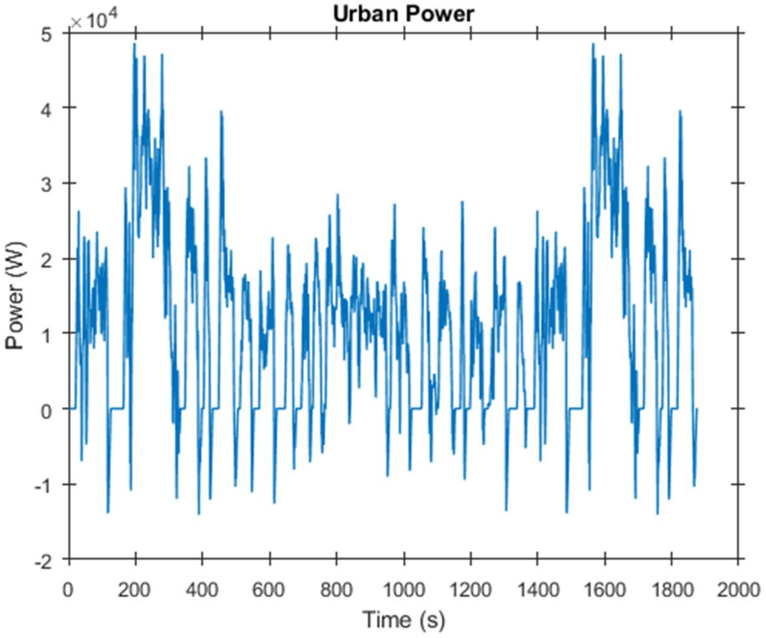

5

Fig. 2.8. UDDS output power profile.

2.3.4 Motor Energy Distribution on the Torque-Speed plane

An effective way to view the drive-cycle loading characteristic is on a torque-speed plane as seen in Fig. 2.9. This plot removes the loading conditionôs dependency on time and instead displays the instantaneous output torque and speed that the electric motor is subject to at each discrete sample point of the drive-cycle. This plot is also an effective way to determine motor design targets in terms of maximum torque and speed capability of an electric machine to satisfy real-life driving conditions [20].

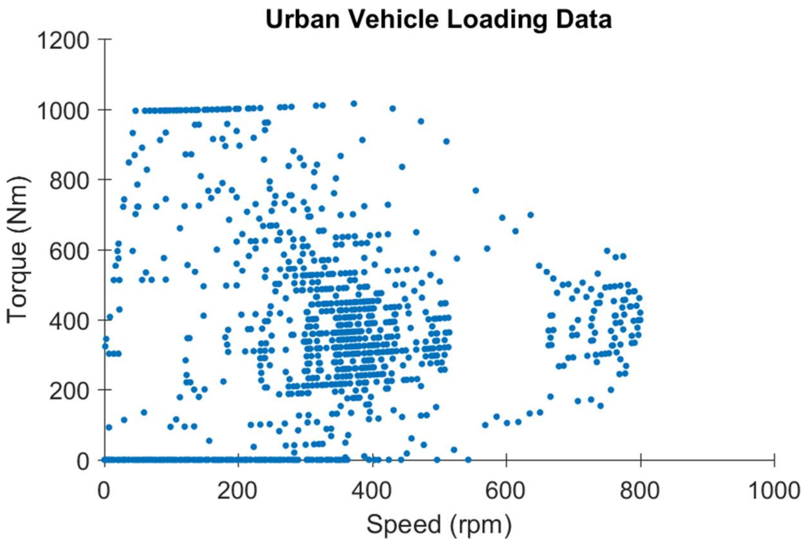

Fig. 2.9. UDDS torque-speed load characteristics for direct-drive machine.

Another significant characteristic of the loading conditions is their associated energy consumption. This is an important characteristic because the motor design must be optimally efficient in regions with high energy consumption to reduce the amount of battery consumption in driving scenarios [13].

Energy is defined as the integral of power over time and can be represented as (2.11) where the motor energy, E_{motor}, is equal to the summation of the discrete samples of power. Similarly, the energy associated with each load point on the torque-speed plane can be calculated using the number of occurrences of that condition in the drive-cycle multiplied by its associated power [13]. The overall energy distribution across the torque-speed plane is shown in Fig. 2.10.

$$E_{motor} = \sum_{t=0}^{t} P_{out}(t) \tag{2.11}$$

2.4 Conclusions

This chapter presented a vehicle dynamics model to derive a direct-drive motorǿs torque, speed, and energy characteristic for a 2014 Ford Fiesta completing the UDDS drive-cycle. The motor loading distribution is illustrated in Fig. 2.10 on a torque-speed plane to visualize the scattered location of load points and their associated magnitude of energy

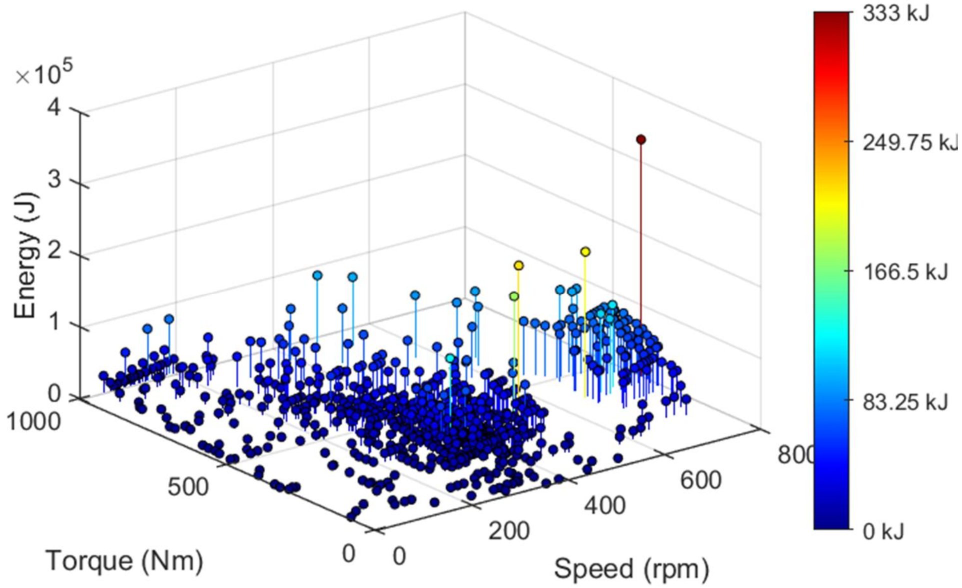

Fig. 2.10. UDDS energy distribution across the torque-speed plane for a direct-drive machine.

consumption. This torque-speed distribution can be used to assist in selecting a machineôs operating envelope when designing a machine by identifying maximum torque and speed requirements of the motor. Furthermore, regions with a high density of points and points with large magnitudes of energy consumption can be identified and targeted in the machine design process to ensure maximum drive-cycle operating efficiency. The regions with a high density of load points are produced when the vehicle is operating frequently around a target speed limit such as 50 km/h for city and 100 km/h for highway. Load points that have a large magnitude of energy consumption are caused by a number of repetitive occurrences and large value of instantaneous power.

It was found that regions of acceleration experience a high torque, but low speed for a short duration of time, therefore the magnitude of energy consumption during acceleration is not as significant as the regions of steady speed operation. The speeds associated with city driving have a larger value of occurrences, but the highway speeds have larger magnitudes of energy consumption due the higher value of instantaneous power. This trade-off makes it difficult to determine which of these regions contains more energy consumption and is more significant in terms of the machineôs operating efficiency. Due to this ambiguity of identifying key regions of operation, statistical data-mining techniques must be introduced to represent the cycle and identify the target regions that have high energy consumption.

CHAPTER 3

Clustering Techniques for Drive-Cycle Data Representation

To properly assess a machineôs performance across a drive-cycle, the motorôs efficiency must be determined at each load point on the torque-speed plane. However, this is computationally intensive due to the vast amount of individual sample points. Thus, statistical data-mining algorithms are introduced to quantize the load data into a minimal number of points that preserve and represent the characteristics of the full dataset. This creates a computationally efficient method of evaluating a machineôs performance across an entire drive-cycle and makes it feasible to implement this type of machine evaluation into an optimization algorithm [21].

3.1 K-Means Clustering

K-means clustering is a statistical algorithm proposed in [22] for drive-cycle data representation. The algorithm separates the data points into *K* clusters where each data point belongs to the cluster with the nearest mean. In an iterative process, the data points get assigned to the nearest mean and the new mean for each cluster is recalculated once all the assignments are complete.

The user defines the number of desired clusters by assigning random points in the torque-speed plane that act as the center of each cluster, known as centroids. The algorithm separates the data by assigning each point to the cluster with the nearest mean given by (3.1) [22].

$$S_i^{(t)} = \left\{ x_p \,\middle|\, x_p - m_i^{(t)2} \leq x_p - m_j^{(t)2} \forall j, 1 \leq j \leq k \right\} \tag{3.1}$$

where, S_i is a set of points that are assigned to the i^{th} cluster. The variable x_p represents a point in the dataset that belongs to subset S_i if its distance to that clusterôs mean, m_i, is shorter than the distance to all the other clustersô means, m_j. The number of clusters is represented by k and the iteration of the calculation is represented by t. In an iterative process, the algorithm reassigns the centroidôs position in each cluster by calculating the average torque and speed in that corresponding sub region using (3.2) [22].

$$m_i^{t+1} = \frac{1}{\left|S_i^{(t)}\right|} \sum_{x_j \in S_i^t} x_j \tag{3.2}$$

The data points are then reassigned and the centroids are recalculated until none of the data points change clusters. This algorithm provides a superior assignment of clusters and distribution of representative points among the dataset as seen in Fig. 3.1, where the various colors represent different clusters and the circular blue points signify the centroids. The torque-speed points are obtained from the vehicle dynamic results outlined in Chapter 2.

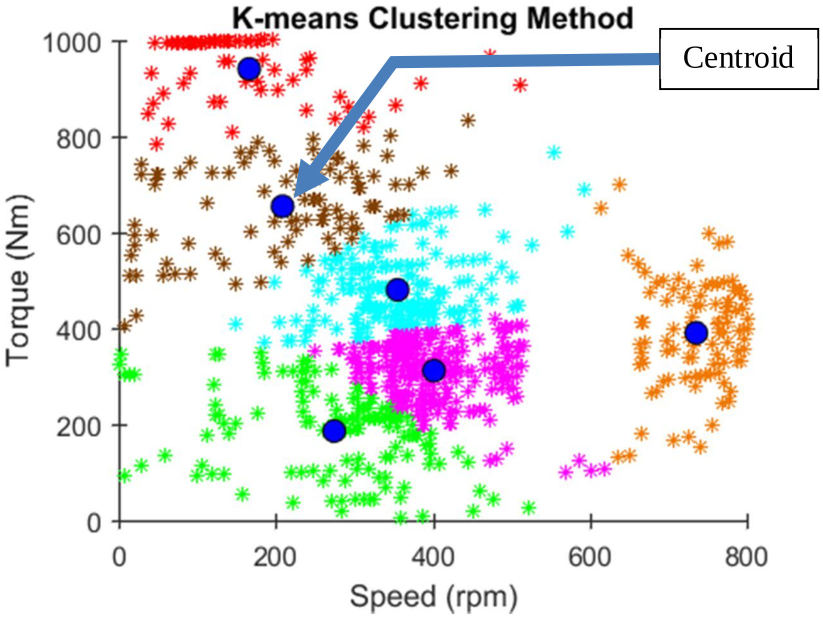

Fig. 3.1. K-means clustering result for torque-speed load data.

3.2 Selecting Number of Clusters in K-Means

In a machine-learning scenario, there is a possibility of over predicting the dataset by assigning too many clusters. This occurs when outliers in the dataset affect the clusters and consequently, having more clusters will inevitably decrease the accuracy of predicting new values. However, since this machine-learning algorithm is being implemented for a fixed dataset, increasing the number of clusters in K-means always increases the accuracy of representation. Therefore, selecting an appropriate number of clusters to use to represent the data becomes an ambiguous trade-off between accuracy of representation and computational efficiency.

3.2.1 Sum of Squared Error Analysis

Calculating the sum of squared error (SSE) for K-means clustering is a method used to assist in selecting an optimal amount of clusters. The equation quantifies the amount of variation between the data points and its groupôs mean [23].

$$SSE = \sum_{i=1}^{k} \sum_{x \epsilon m_i} dist\left(x, m_i\right)^2 \qquad (3.3)$$

The SSE equation is evaluated using the K-means clustering results for different possibilities of *k*. As the number of clusters increases, the value of SSE exponentially decays to zero at which point, the number of clusters is equal to the number of data points. This creates an ñelbow effectò in the SSE plot as seen in Fig. 3.2. The selection for the number of clusters is thus justified by the law of diminishing returns, where the increase in representational accuracy does not justify the increase in computational burden. From the plot, it is observed that six clusters are sufficient to represent the data while maintaining a small number of representative points for computational efficiency.

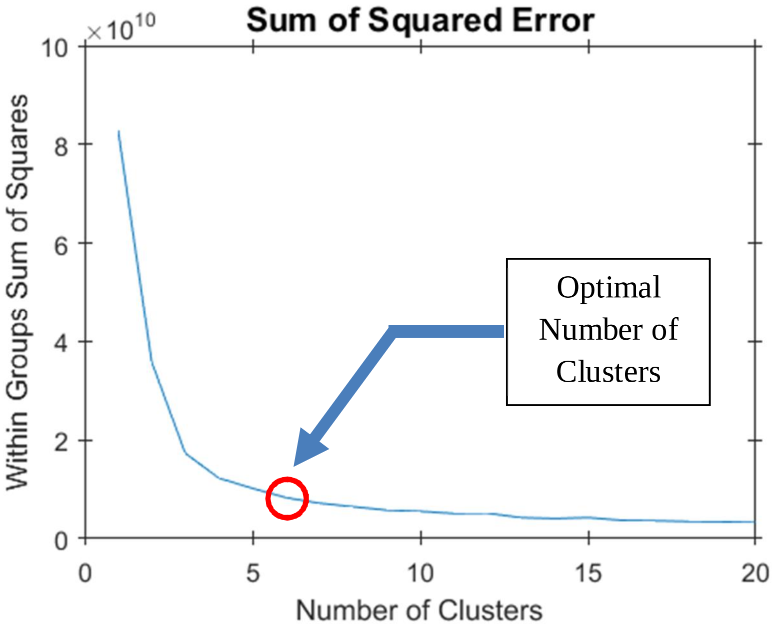

Fig. 3.2. Sum of squared error results for cluster selection.

3.3 Addressing Energy Significance in Clustering Algorithms

The K-means clustering method however, exclusively uses the torque and speed information to cluster the data and therefore, it fails to properly address the energy significance of the points within a given cluster. For this reason, it should be known that improvements can be made by proposing a new approach in order to achieve both optimal distribution and weighted significance of the representative data points.

3.3.1 Hybrid Clustering Technique

A proposed solution is to hybridize the K-means clustering algorithm with an ñEnergy Center of Gravity” (ECG) technique to get the best possible representation for any number of clusters on any drive-cycle. The ECG method is used in [24] ï [26] to perform a weighted mean on each cluster once the algorithm converges. Each pointôs associated energy E_{ij} is normalized to the total energy in that given cluster E_i as in (3.4) and is used as the weight within the ECG method. The weighted means in terms of torque and speed of each cluster are used as the representative data points. These calculated representative data point positions, ω_{mci} and T_{mci}, that factor in each pointôs energy significance are given by (3.4) and (3.5) [24].

$$E_i = \sum_{j=1,2,\ldots}^{N_i} E_{ij} \tag{3.4}$$

$$\omega_{mci} = \frac{1}{E_i} \sum_{j=1,2,\ldots}^{N_i} E_{ij}\omega_{mij} \tag{3.5}$$

$$T_{mci} = \frac{1}{E_i} \sum_{j=1,2,\ldots}^{N_i} E_{ij}T_{mij} \tag{3.6}$$

This method is significant as it considers the dataôs associated weight by positioning the representative point closer to regions with higher energy consumption, which is more valuable when attempting to obtain vehicle energy loss minimization. The K-means clustering algorithm is used to optimally cluster the data in the torque-speed plane and rather than using the centroids, the ECG method is applied to each of the segmented clusters to calculate the location of the representative point. The energy consumed in each cluster is normalized to the total energy consumed to assign weights to the representative points.

3.3.2 Results for Hybrid Clustering Technique

Figure 3.3 displays the result of both the K-means clustering algorithm and the hybrid method as a comparison. The blue points signify the K-means clustering result that uses the centroids as the placement of the representative points and the white points are the result of the hybrid method that have a different position but carry the same weighted significance as the K-means method. The results show that there is a significant change of torque-speed location for all the representative points which proves that the energy significance is an essential characteristic to consider while clustering. Table 3.1 presents the final results of speed and torque values for each cluster, along with their normalized energy.

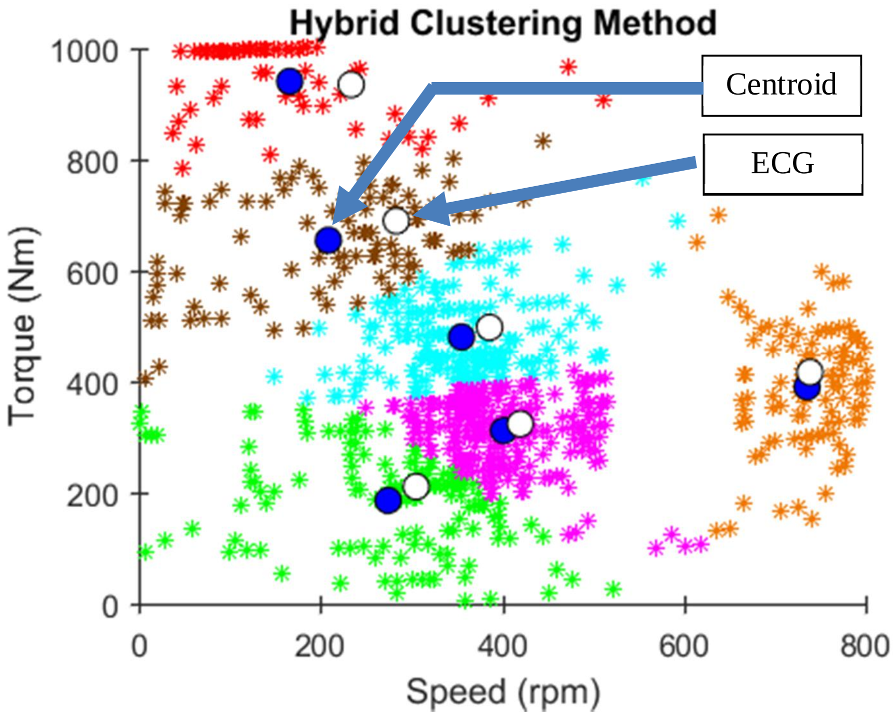

Fig. 3.3. Results for hybrid clustering approach.

TABLE 3.1

Hybrid Clustering Result

Speed (rpm)	Torque (Nm)	Normalized Energy (%)
233.85	934.91	7.89%
283.49	689.70	8.77%
305.39	210.68	4.23%
386.15	498.09	22.76%
419.95	323.66	26.28%
738.85	416.48	30.07%

3.3.3 Data Resampling Technique

Another method to accurately address the energy significance of the representative points is to utilize a method called ñresamplingò to modify the dataset. The resampling method finds the smallest magnitude of energy consumption in the dataset and uses it to increase the number of points at all other data point locations as in (3.7). This makes the dataset much larger but ensures that all points have an equal weight in terms of energy consumption.

$$n_{points,i} = \frac{|E_i|}{min(E)} \tag{3.7}$$

This method allows K-means to consider the energy significance when determining the location and size of the clusters on the torque-speed plane. This increases the accuracy of representation in comparison to the previous method since the energy significance is also considered in the grouping stage. The final representative point that is considered for machine evaluation is the centroid or mean since it is already a weighted average of the points in the cluster due to the applied resampling method.

3.3.4 Results for Data Resampling Technique

Employing the resampling technique and performing K-means clustering for an optimal value of clusters equal to six, gives the result displayed in Fig. 3.4. The representative load points with their corresponding energy significance are outlined in Table 3.2.

TABLE 3.2

K-Means Clustering Result for Resampled Data

Speed (rpm)	Torque (Nm)	Normalized Energy (%)
179.88	730.96	12.29%
293.08	393.57	17.79%
378.37	674.08	8.26%
396.18	150.21	28.62%
510.37	387.39	7.50%
743.61	197.81	25.54%

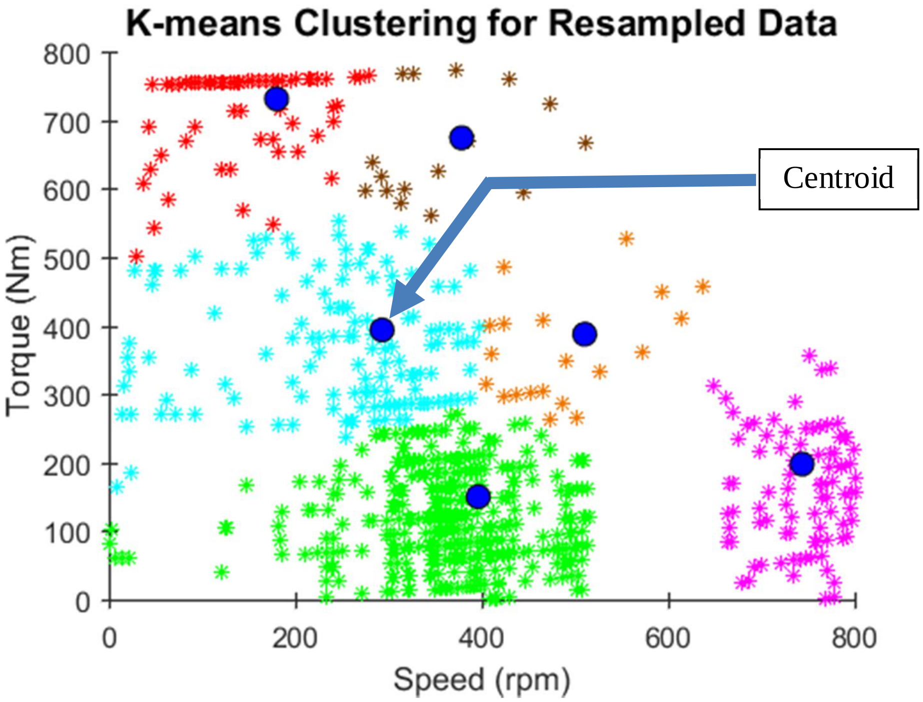

Fig. 3.4. Results for K-means clustering using the resampled dataset.

3.4 Gaussian Mixture Modeling

Gaussian Mixture modelling (GMM) is another technique used to characterize and group random variables based on continuous probability distributions. The probability distribution is called a Gaussian or normal distribution and is defined by (3.8) where µ is the mean and ů^2 is the covariance, which is a measure of the expected squared deviation of a data point from the mean [27]. These parameters determine the location and shape of the distribution as seen in Fig. 3.5.

$$f\left(x\middle|\mu,\sigma^2\right)=\frac{1}{\sqrt{2\pi\sigma^2}}e^{-\frac{(x-\mu)^2}{2\sigma^2}} \tag{3.8}$$

Mixture Modelling is a probabilistic model for representing subpopulations within a dataset. Figure 3.6 displays how several Gaussian distributions are used to increase the accuracy in characterizing the overall probability distribution of the data set.

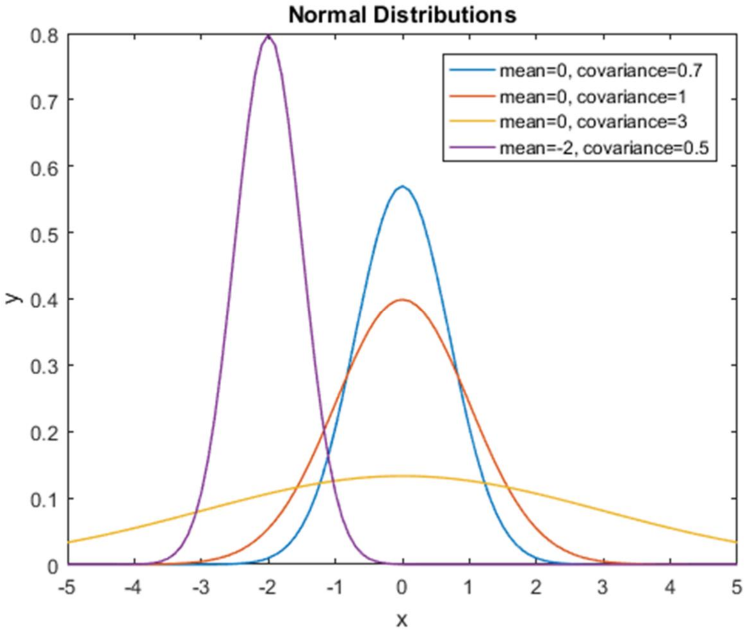

Fig. 3.5. Normal distributions with varying means and covariance.

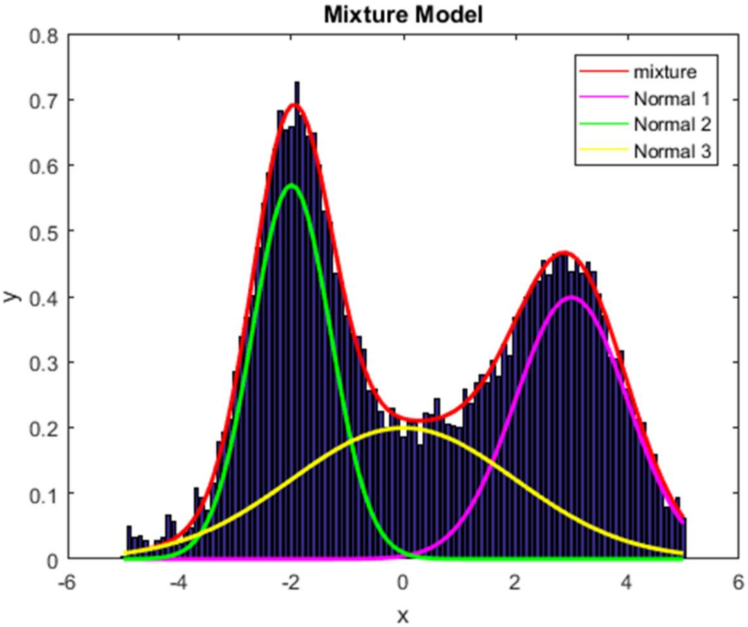

Fig. 3.6. Mixture model of normal distributions.

Gaussian mixture modelling is an unsupervised learning algorithm that contains K components (or Gaussians). It is different from K-means clustering since it is a soft clustering algorithm and it is less prone to outliers. Soft clustering indicates that a single data point can belong to more than one cluster. In Gaussian mixture-modelling, each point is assigned a probability of belonging to each component in the model. This eliminates the need for strict cluster assignments when points are located in a region that is equally spaced between two or more clusters. The algorithm is also less prone to outliers since points located far from regions with a high density of points are assigned a low probability and contribute less to the calculation of the Gaussianôs mean. This is an important attribute since it ensures that the Gaussian will remain located in high-density regions without being affected by random outliers.

A multi-dimensional probability density function is given as (3.9), where y is a data point with d dimensions and C is the covariance matrix [27].

$$g\left(\vec{y}\middle|\vec{\mu}_i, C_i\right) = \frac{1}{\sqrt{\left(2\pi\right)^K \left|C_i\right|}} e^{\left(-\frac{1}{2}\left(\vec{y}-\vec{\mu}_i\right)^T C_i^{-1}\left(\vec{y}-\vec{\mu}_i\right)\right)} \tag{3.9}$$

3.4.1 Expectation Maximization Algorithm

The Gaussian mixture model aims to maximize the log-likelihood function given in equation (3.10) where $ɗ_m = (µ_m, C_m)$ is the parameter vector of a given component, $\bar{\text{U}}_{(K)}$ is the parameter set defining a given mixture specified in (3.11), N is the number of observations in the dataset, and Ǚ_m is the mixing probability or component distribution. The maximum likelihood cannot be directly calculated since it requires differentiating the log-likelihood function which is analytically unfeasible, thus the expectation maximization (EM) algorithm is implemented. EM is an iterative algorithm that is guaranteed to increase the likelihood on each iteration and approach a local maximum [28].

$$L\left(\bar{\text{U}}_{(K)}, y_{obs}\right) = \sum_{i=1}^{N} \log \sum_{m=1}^{K} \alpha_m g\left(\vec{y}_i\middle|\theta_m\right) \tag{3.10}$$

$$\Theta_{(K)} = \{\theta_1, \ldots, \theta_K, \alpha_1, \ldots, \alpha_{K-1}\} \tag{3.11}$$

$$\sum_{m=1}^{K} \alpha_m = 1 \tag{3.12}$$

The initialization step is used to assign arbitrary model parameters in terms of the mean, covariance matrices, and component distribution for all Gaussians in the mixture model. The component means are set to randomly selected points within the dataset. Each covariance is set to the sample covariance as in (3.13) and a uniform component distribution is set as in (3.14) [27].

$$C_1 \ldots C_K = \frac{1}{(N-1)} \sum_{i=1}^{N} (y_i - \bar{y}) \tag{3.13}$$

$$\alpha_1 \ldots \alpha_K = \frac{1}{K} \tag{3.14}$$

The Expectation (E) step calculates the expectation of the component assignments for each data point using the updated model parameters as in (3.15) [27].

$$\hat{\gamma}_{ik} = \frac{\hat{\alpha}_k g\left(y_i \middle| \hat{\mu}_k, C_k\right)}{\sum_{j=1}^{K} \hat{\alpha}_j g\left(y_i \middle| \hat{\mu}_j, C_j\right)} \tag{3.15}$$

The Maximization (M) step maximizes the expectations determined in the E step by updating the model parameters [27]:

$$\alpha_k = \sum_{i=1}^{N} \frac{\hat{\gamma}_{ik}}{N} \tag{3.16}$$

$$\hat{\mu}_k = \frac{\sum_{i=1}^{N} \hat{\gamma}_{ik} x_i}{\sum_{i=1}^{N} \hat{\gamma}_{ik}} \tag{3.17}$$

$$\hat{C}_k = \frac{\sum_{i=1}^{N} \hat{\gamma}_{ik} \left(x_i - \hat{\mu}_k\right)^2}{\sum_{i=1}^{N} \hat{\gamma}_{ik}} \tag{3.18}$$

The algorithm iterates over the expectation and maximization steps until the parameters converge to a user-defined tolerance.

3.4.2 MMDL for Component Selection in GMM

Mixture minimum description length (MMDL) is reported to have outperformed existing criteria of component selection with comparable computational cost. MMDL is implemented with the EM approach to select the number of components to be used for the model. The MMDL cost function is displayed in equation (3.19) where *H(K)* is the number of parameters required to specify a *K*-component mixture. Given the number of dimensions and the number of components, *H(K)* is calculated using (3.20) [29].

$$C_{MMDL}\left(\hat{\text{Ū}}_{(k)}, y_{obs}\right) = -L\left(\text{Ū}_{(k)}, y_{obs}\right) + \frac{H(K)}{2}\log N + \frac{H(1)}{2}\sum_{M=1}^{K}\log \alpha_m \quad (3.19)$$

$$H(K) = (K-1) + K\left(d + d(d+1)/2\right) \quad (3.20)$$

To implement the MMDL criterion, a maximum and minimum number of components are selected. The EM algorithm is executed for each number of components and the cost function defined in (3.19) is evaluated and stored. The component number with the lowest MMDL criterion K_{MMDL} seen in (3.21) is selected and determines the parameter set, $\text{Ū}_{(K_{MMDL})}$ defining a given mixture [29].

$$\hat{K}_{MMDL} = \arg\min_{K}\left\{C_{MMDL}\left(\hat{\text{Ū}}_{(K)}, y_{obs}\right), K = K_{min}, K_{min}+1\ldots, K_{max}\right\} \quad (3.21)$$

3.4.3Results for GMM using Resampling Technique

The EM algorithm is stopped if the conditions in (3.22) are true given that ŭ_{μ} and ŭ_{C} are the tolerances that are set to 0.001 and *t* is the iteration of the EM algorithm [29]. This approach is applied to the resampled dataset to achieve the MMDL results plotted in Fig. 3.7. The results prove that a component number of six is the best number of Gaussians to model the dataset. The final mixture model is seen in Fig. 3.8 with the given representative loading points derived from GMM are summarized in Table 3.3. The mean of each component is assigned as the location of the corresponding representative load point and the normalized energy significance is equivalent to the component distribution.

$$\begin{cases} \max\limits_{m=1,2,\ldots,K} \dfrac{\hat{\mu}_m^{(t)} - \hat{\mu}_m^{(t-1)}}{\hat{\mu}_m^{(t)}} < \delta_\mu \\ \max\limits_{m=1,2,\ldots,K} \dfrac{\hat{C}_m^{(t)} - \hat{C}_m^{(t-1)}}{\hat{C}_m^{(t)}} < \delta_C \end{cases} \tag{3.22}$$

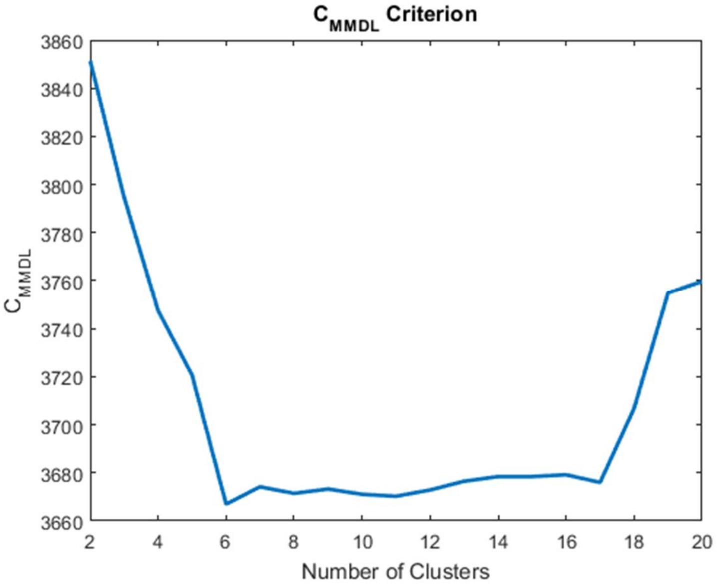

Fig. 3.7. Mixture minimum description length for component selection.

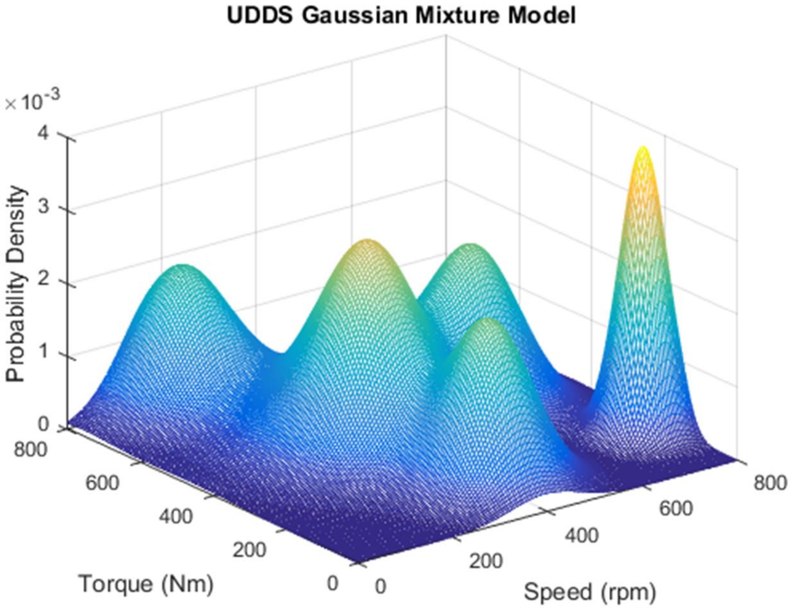

Fig. 3.8. Gaussian mixture modeling result for resampled dataset.

TABLE 3.3

Gaussian Mixture Modeling Result for Resampled Data

Speed (rpm)	Torque (Nm)	Normalized Energy (%)
207.52	760.03	10.35%
326.79	393.43	20.73%
344.37	471.29	15.26%
395.15	151.86	25.14%
593.46	451.22	4.91%
749.05	193.14	23.60%

3.5 Conclusions

K-means clustering and Gaussian mixture modeling are introduced as two different methods for performing drive-cycle data representation. The aim of these algorithms is to portray the characteristics of the entire drive-cycle with a reduced number of sample points. This identifies target areas of torque and speed motor operation that consume a large amount of energy consumption during the drive-cycle. In addition, these representative points are imperative for performing drive-cycle analysis in scenarios where maximum computational efficiency is required since evaluation can be performed by only considering a minimal number of samples.

The clustering techniques demonstrated that the regions of acceleration account for approximately 10 ï 13 percent of the total energy consumption in the drive-cycle. Furthermore, the loading points corresponding to high-speed operating regions account for about 23 ï 25 percent of the energy consumption. The most significant portion is characterised by multiple representative points in the mid-speed operating range around 300 ï 400 rpm with 50 ï 60 percent of the total energy consumption. This high value of energy consumption is caused by the large number of occurrences of operating points in the mid-speed range throughout the cycle.

This thesis focuses on the integration of these drive-cycle data representation techniques into two separate applications. This includes a multi-objective motor optimization for a drive-cycle and a system level motor-inverter simulation for drive-cycle assessment. The optimization scheme requires the execution of drive-cycle analysis for hundreds of machine topologies. Therefore, using a reduced number of drive-cycle representative points significantly increases the computational efficiency of the algorithm and makes drive-cycle optimization possible without the need for high performance computing. Similarly, a system level analysis that includes the FEA motor simulation with different inverter excitations is another distinct application that is computationally intensive. Therefore, the K-means clustering technique is used to make drive-cycle performance assessment feasible for the analysis of the effects of different inverter devices on motor performance.

CHAPTER 4

Computationally Efficient FEA Machine Evaluation Procedure

Chapter 3 introduced a method to determine a minimal number of representative load points to make it computationally feasible to evaluate a close approximation of a machine’s drive-cycle energy efficiency. The first aim of this thesis is to optimize a direct-drive machine using the energy efficiency across the drive-cycle as one of the objectives. Therefore, a computationally efficient finite element analysis (CEFEA) technique introduced in [30] is described in this chapter to evaluate the efficiency of the motor at different load conditions. The technique is required to make it computationally feasible to utilize finite element analysis results in an optimization program for machine evaluation. FEA is utilized because it is superior to analytical models for performing machine evaluation since it considers non-linear effects of materials such as saturation [31], [32]. The baseline machine and the CEFEA method employed for calculating torque ripple, drive-cycle energy efficiency, weight, and active material cost is presented.

4.1 Baseline Machine for Analysis

A baseline fractional slot concentrated winding (FSCW) surface permanent magnet synchronous machine (SPMSM) with 36 slots and 30 poles designed for a direct-drive battery electric vehicle (BEV) is considered in this thesis with the design targets listed in Table 4.1 [33], [34]. A direct-drive vehicle eliminates the fixed gear ratio that is commonly placed in electric vehicles between the motor and the output shaft connected to the wheels. Therefore, motor is required to deliver high torque for low speed operation. Using the procedure outlined in [33], the machine was designed to meet a continuous torque of 875 Nm and a peak torque of 1,750 Nm until a rated speed near 575 rpm. A rated motor speed of 575 rpm corresponds to a vehicle speed of nearly 55 km/h [35]. Maximum capability of the machine in terms of its torque, speed and output power was elicited using the electromagnetic model of the designed FSCW SPMSM machine in conjunction with FEA and maximum torque per ampere (MTPA) flux-weakening (FW) control algorithm both in the constant torque and power regions. Figure 4.1 shows the cross-section of the SPMSM motor and the flux density distribution while operating at

875 Nm under 165 A rms/phase. Figure 4.2 shows the torque and power characteristics over the entire speed range of the motor obtained using the electromagnetic model of the machine in conjunction with MTPA controls with voltage and current constraints of 450 V and 165 A rms/phase and maximum current of 400 A rms/phase. This motor will be used as a reference for benchmarking any improvements in the optimized motors that will be designed in this paper. Tables 4.2 ï 4.4 present details and dimensions for the stator, rotor, and slot respectively. A direct-drive machine has several design challenges including [36], [37]:

1. Size, weight, and cost since there is a high torque requirement.
2. Torque ripple that can no longer be dampened by the mechanical components of the transmission system.
3. Efficiency due to the high ampere loading required to get the large magnitude of average torque.

Optimization is employed in an attempt to address these design challenges in conjunction with drive-cycle energy efficiency.

TABLE 4.1

Design Targets for Direct-Drive FSCW SPMSM

Peak Power	91.6 kW
Peak Torque	1,750 Nm
Continuous Torque	875 Nm
Continuous Power	45.8 kW
Maximum CPSR Speed (16 inch tire)	2,000 rpm
Motor Weight	< 65 kg
Inverter Weight (existing EV inverter)	12 kg
Rated Current (A rms/phase)	< 180 A
Maximum Current (A rms/phase)	<= 400 A
Torque Ripple (% of peak torque)	< 5%
Rated Efficiency	> 94%

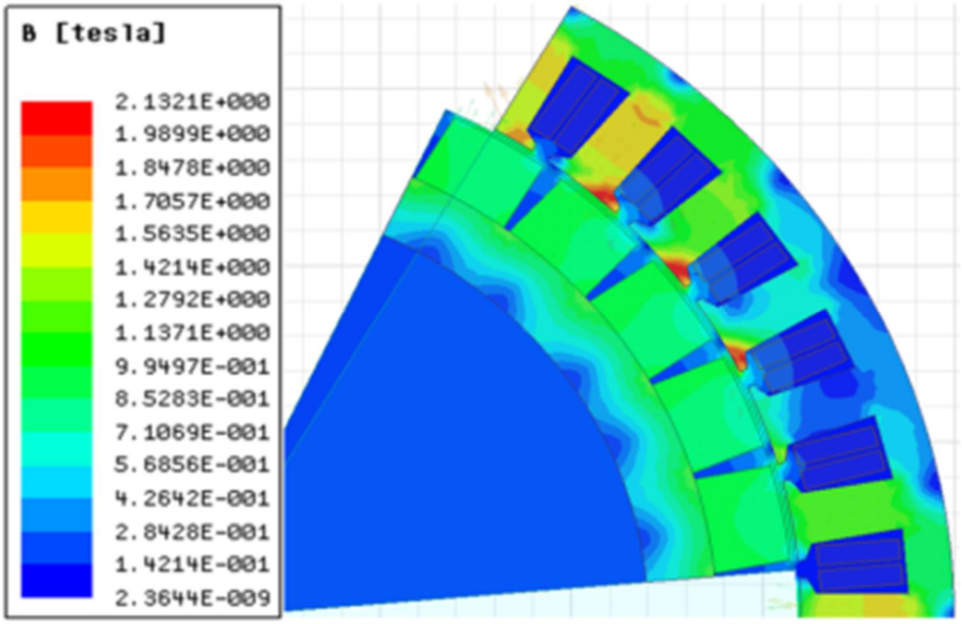

Fig. 4.1. Cross-section of 36/30 direct-drive baseline machine.

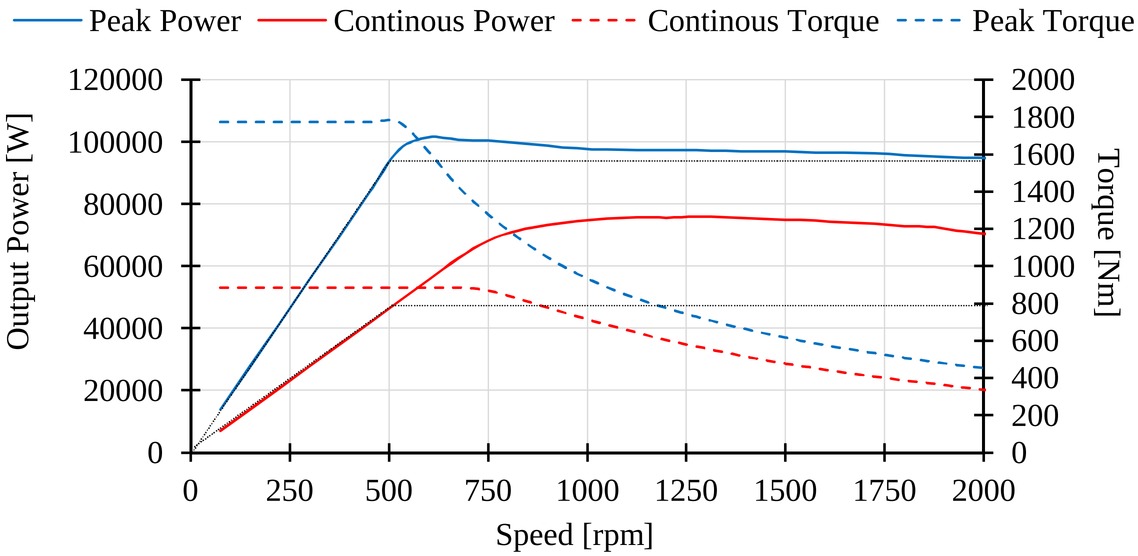

Fig. 4.2. Torque-speed and power-speed characteristics of the baseline direct-drive FSCW SPMSM.

TABLE 4.2

Stator Design Details of the Direct-Drive Machine

Stator Slots	36
Poles	30
Stator Outer Diameter	400 mm
Stator Inner Diameter	320 mm
Length of Stator Core	105 mm
Coils/phase	12
Current Density	7.5 A/mm^2
Winding Factor	0.933
Stator Teeth Flux Density	1.7 T
Turns/phase	84
Number of Parallel Paths	1
Rated Continuous Current (rms/phase)	165 A
Slot Fill Factor	75%

TABLE 4.3

Rotor Design Details of the Direct-Drive Machine

Thickness of Magnet	20 mm
Width of Magnet	27.1 mm
Type of Magnet	NdFeB 35
Air-gap with Banding Thickness	2 mm
Rotor Inner Diameter	240 mm
Length of Rotor	105 mm
Type of Steel	M19 29G
Mechanical Pole Embrace	0.82
Polar Arc Radius	158 mm
Residual Flux Density	1 T
Coercive Force (kA/m)	710.32

TABLE 4.4

Slot Design Details of the Direct-Drive Machine

Slot Opening (b_{s0})	5 mm
Slot width at top of slot	18.5 mm
Slot width at bottom of slot	14.0 mm
Average slot width at center of slot	16.5 mm
Slot height (h_s)	22.0 mm
h_2	2.0 mm
h_3	2.0 mm
h_4	2.0 mm

4.2 Computationally Efficient Finite Element Analysis

Finite element method (FEM) is a numerical method for solving complex problems in engineering. FEM involves generating a mesh to divide complex geometries into small pieces for analysis. While solving, FEM uses material definitions to address nonlinear characteristics of different materials such as the magnetic saturation of steel. These nonlinear characteristics are difficult to consider in analytical models and thus, FEM is a highly effective and accurate method for performing electromagnetic modelling of an electric machine.

CEFEA is a technique used to exploit the electric symmetry of PMSMs with sinusoidal current excitation to save on computation time. In addition, the technique merges a minimal number of 2-D magnetostatic finite-element simulations with analytical calculations to reduce simulation time and reduce computational burden. CEFEA can therefore, be implemented into optimization programs to analyze hundreds of machine models without the need for high performance computing [30].

4.2.1 Electric Symmetry of PMSMs

Figures 4.3 and 4.4 show how the 60-degree symmetry of the baseline machine converts 5 magnetostatic FEM solutions into 30 usable samples. Each magnetostatic FEM simulation provides three equally spaced samples because of the symmetry of the electromagnetic circuit. Therefore, phase *a* can be determined by applying a phase shift to the corresponding values of the other two phases as in (4.1) and (4.2) where *A* is the magnetic vector potential and ɗ is the phase angle. Furthermore, half-wave symmetry is applied to double the number of points and recreate the full 360-degree waveform [30].

$$\mathrm{A}_{a+}\left(\theta+60^{\circ}\right)=-\mathrm{A}_{c+}\left(\theta\right) \tag{4.1}$$

$$\mathrm{A}_{a+}\left(\theta+120^{\circ}\right)=\mathrm{A}_{b+}\left(\theta\right) \tag{4.2}$$

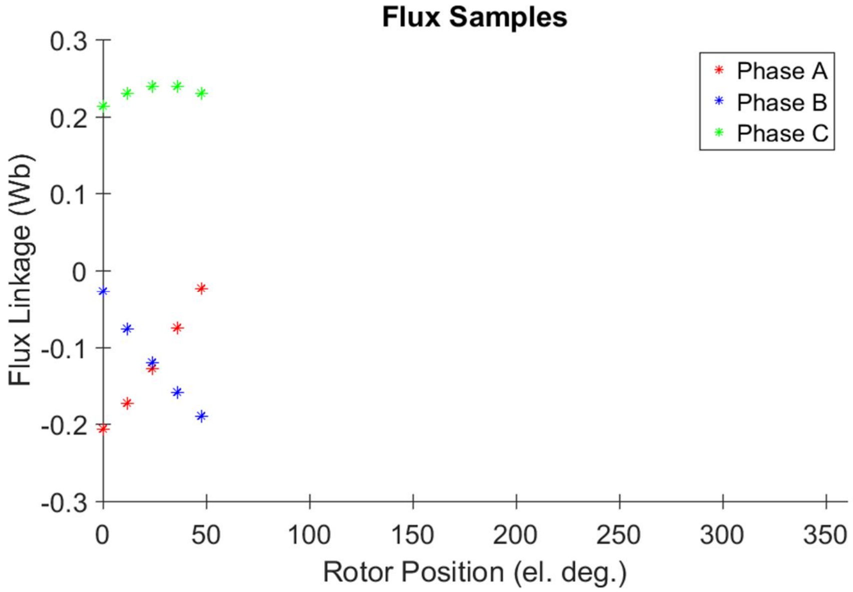

Fig. 4.3. Three phase flux-linkage waveform results obtained from five magnetostatic solutions.

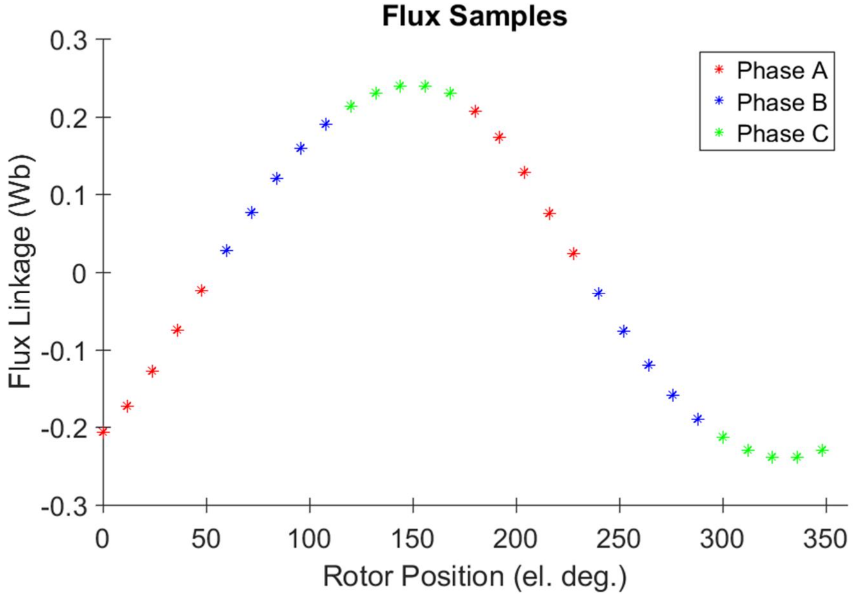

Fig. 4.4. 30 samples of the phase A flux-linkage waveform obtained from five magnetostatic solutions.

Magnetic vector potentials in the coil sides of the machine are the principal results of FEA that enable post-processing. From these results, analytical equations are used to derive important motor characteristics. Figure 4.5 shows how coils are placed around the teeth to obtain the required magnetic vector potentials with harmonic content for performing CEFEA.

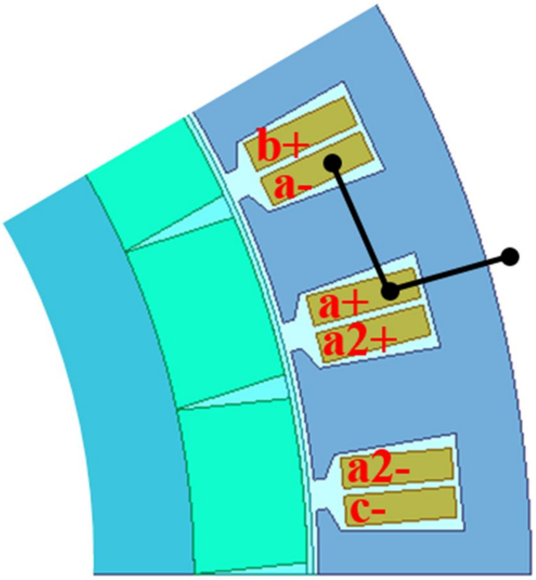

Fig. 4.5. Coil around tooth and virtual coil around stator back iron used in FEA.

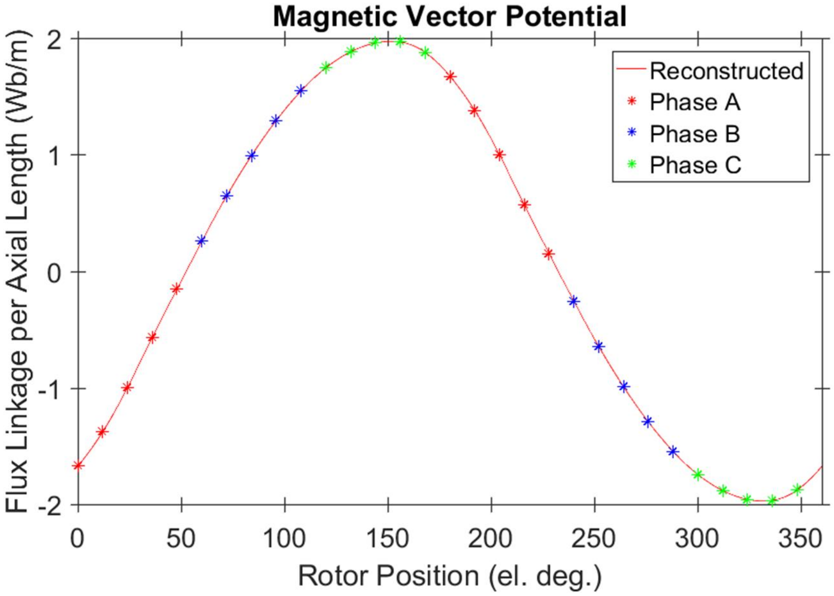

Fig. 4.6. Radial flux per unit axial length for one turn of a coil placed around a stator tooth.

4.2.2 Flux-Linkage, Back EMF, and Torque Derivation

The radial flux per unit axial length ū for one turn of a coil placed around a stator tooth seen in Fig. 4.6 is determined from the average magnetic vector potential in both coil sides as in (4.3) [30].

$$ū_{a+a-} = \mathrm{A}_{a+} - \mathrm{A}_{a-} \tag{4.3}$$

Multiplication with the number of series turns per phase derives the flux linkage per unit of axial length of the machine. Applying the axial length of the machine then generates the flux linkage waveform of the motor seen in Fig. 4.7. All three phases can be reconstructed by applying a 120-degree phase shift to the waveform. A fast Fourier transformation (FFT) is performed to obtain the fundamental and harmonic content in the waveform. The waveform can therefore be modelled as a Fourier series of the fundamental and harmonic components as seen in (4.4) where v is the harmonic order, ɚ is the flux linkage, and ◖$_{\mathrm{v}}$ is the phase angle for the v^{th} harmonic. The maximum harmonic order is a function of the number of magnetostatic solutions, s, as in (4.5). Using five solutions produces 30 useable samples, which provides results that account for harmonics up to the 14th order [30].

$$\lambda_a(\theta) = \sum_{v=1}^{v_M} \lambda_v \cos\left(v\theta + \phi_v\right) \tag{4.4}$$

$$v_M = 3s - 1 \tag{4.5}$$

The back EMF e_a waveform is obtained using (4.6) and is displayed in Fig. 4.8. Similarly, the electromagnetic torque T_{em} is derived using (4.7) where i is the current and P is the number of poles in the machine [38]. The electromagnetic torque waveform illustrated in Fig. 4.9 contains the average torque component and the torque ripple caused by the space harmonics in the machine. Torque ripple is calculated using the difference between the maximum and minimum value over the magnitude of average torque. Torque ripple causes oscillations, noise and can lead to early degradation of mechanical components within the machine. The desired value of average torque is determined in the early stages of machine

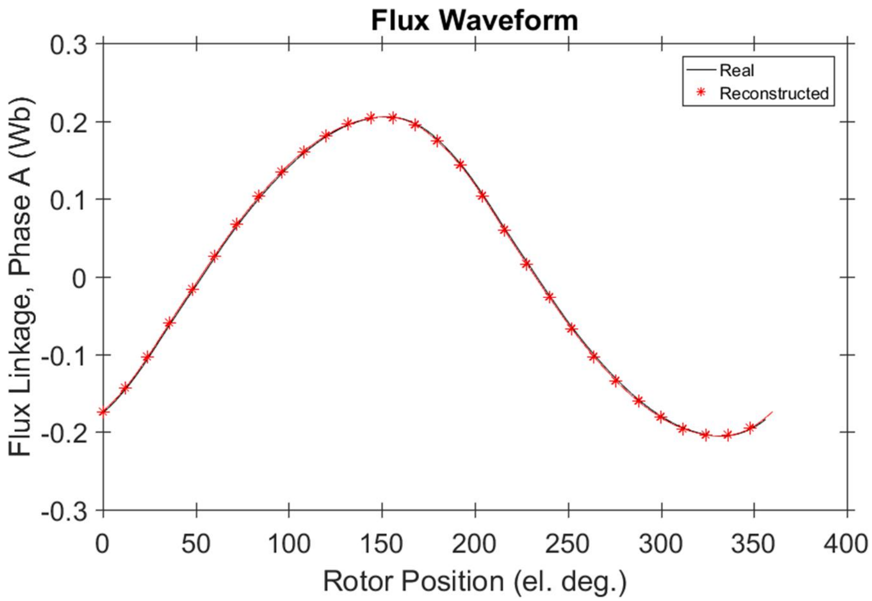

Fig. 4.7. Flux-linkage waveform derived from FEA.

design to ensure that the motor will satisfy all driving conditions in a specific vehicle application. In an optimization scheme, the machine geometry gets manipulated and performance characteristics such as the average torque capability vary. Therefore, it is essential to develop a technique to maintain the capability of delivering the desired amount of torque for each motor model being generated by the optimization program [22].

$$e_a(\theta) = -\frac{d\lambda_a}{d\theta}\frac{d\theta}{dt} = \omega\sum_{v=1}^{v_M} v\lambda_v \sin(v\theta+\phi_v) \tag{4.6}$$

$$T_{em} = \frac{P}{2}\left(\begin{array}{l} i_a(\theta)\sum_{v=1}^{v_M} v\lambda_v \sin(v\theta+\phi_v) + i_b(\theta)\sum_{v=1}^{v_M} v\lambda_v \sin(v\theta+\phi_v-120°) + \\ i_c(\theta)\sum_{v=1}^{v_M} v\lambda_v \sin(v\theta+\phi_v-240°) \end{array}\right) \tag{4.7}$$

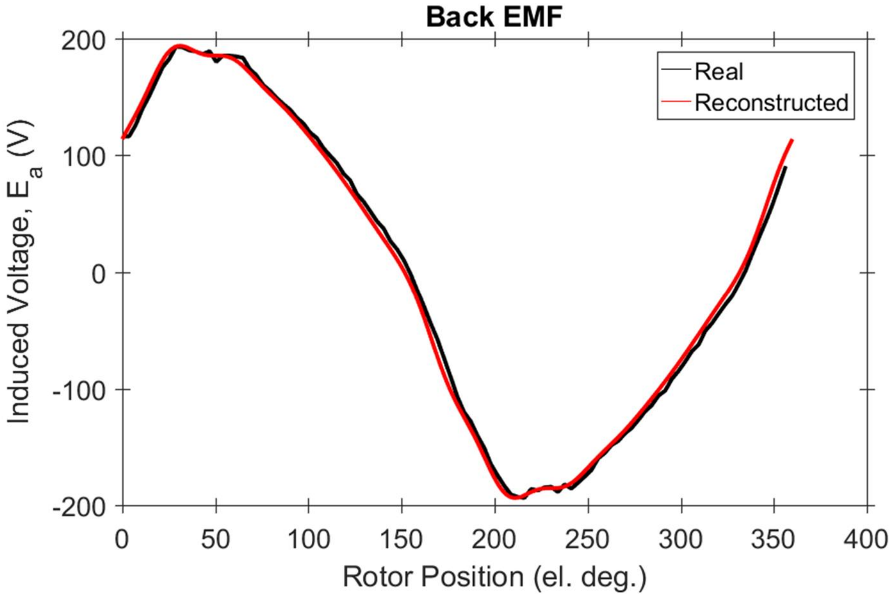

Fig. 4.8. Back EMF waveform derived from FEA.

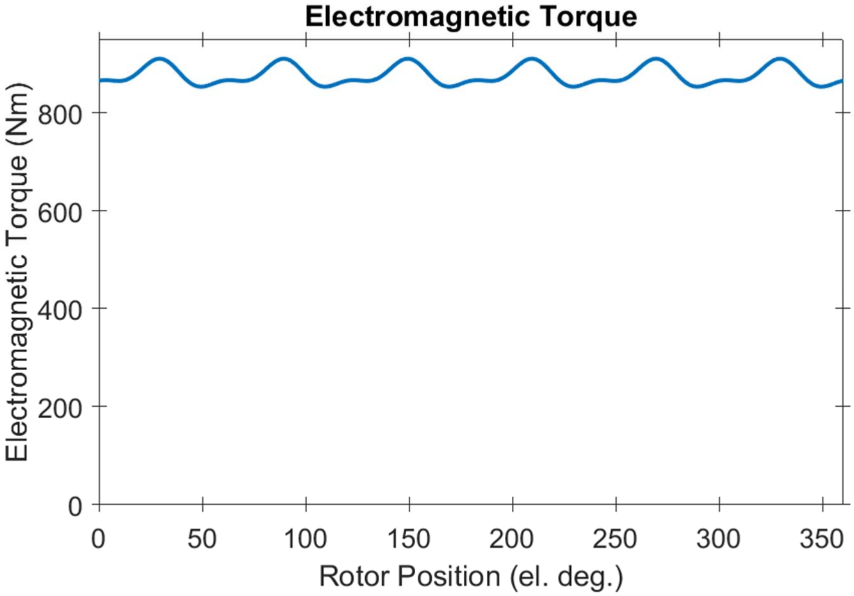

Fig. 4.9. Continuous torque waveform derived from FEA.

4.3 Scaling Stack Length for Desired Torque Production

To ensure that each machine created by the optimization has the same rated value of average torque, a single CE-FEA solution is performed at rated conditions to scale the stack length of the machine to produce the desired torque [22]. The electromagnetic torque produced by a PMSM is expressed as

$$T_e = \frac{3P}{4}\left(\lambda_d I_q - \lambda_q I_d\right) \tag{4.8}$$

where λ_d and λ_q are the d- and q-axis flux-linkages and I_d and I_q are the d- and q-axis current excitations. The flux-linkages can be re-written in terms of d- and q-axis inductances and permanent magnet (PM) flux-linkage λ_{PM} as in (4.9) [39].

$$\begin{cases} \lambda_d = \lambda_{PM} + L_d I_d \\ \lambda_q = L_q I_q \end{cases} \tag{4.9}$$

Using (4.9), the electromagnetic torque (4.8) can be re-written as (4.10), which expresses the torque in two components: magnetic torque and reluctance torque [39].

$$T_e = \frac{3P}{4}\left(\lambda_{PM} L_q + \left(L_d - L_q\right) I_d I_q\right) \tag{4.10}$$

In an SPMSM, the reluctance torque component is negligible since the d- and q-axis inductances are approximately equal in magnitude. Therefore, it can be assumed that the torque of the machine is entirely dependent on the value of PM flux-linkage and number of poles. Since the number of poles is fixed in the machine, the PM flux-linkage needs to be determined and scaled in order to produce the same amount of torque as the baseline machine [8]. To determine the PM flux-linkage, rated current is delivered in the q-axis and I_d is set to zero. Thus, the d-axis component of flux-linkage is equivalent to the PM flux-linkage and can be justified by simply substituting $I_d = 0$ into (4.9). A Park's transformation is applied to the three phase waveforms of flux-linkage obtained from CEFEA [6] as seen in (4.11) and (4.12) to evaluate the PM flux-linkage [8]. Finally, the length of the motor L is determined as in (4.13) to obtain the same magnitude of PM flux-linkage. This ensures that every motor model has an equal magnitude of average torque at rated condition and guarantees that all vehicle driving performance requirements are met [39].

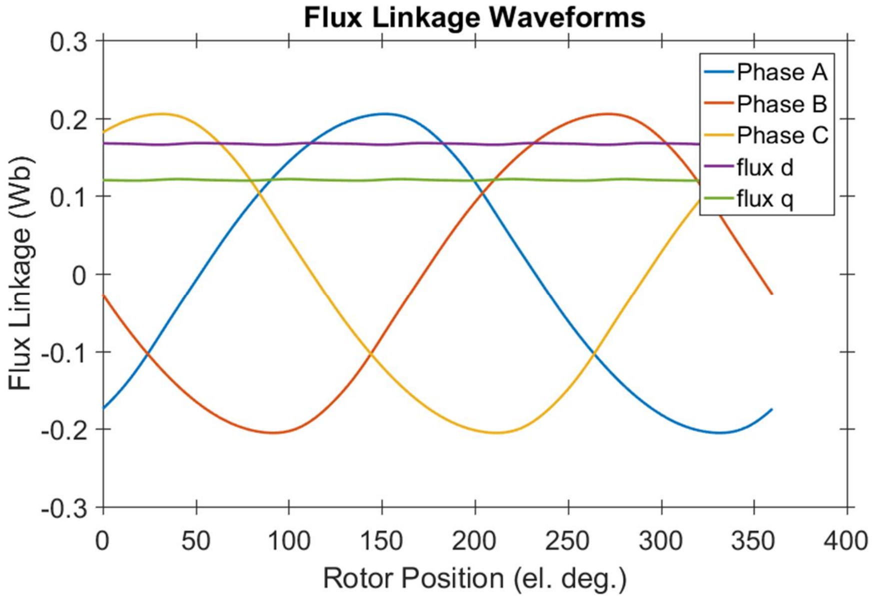

Fig. 4.10. *d*- and *q*-axis flux-linkages determined from the 3-phase flux-linkage waveforms.

$$\lambda_{PM} = \lambda_d = \frac{2}{3}\left[\cos(\theta)\lambda_a + \cos\left(\theta - \frac{2\pi}{3}\right)\lambda_b + \cos\left(\theta - \frac{4\pi}{3}\right)\lambda_c\right] \tag{4.11}$$

$$\lambda_q = \frac{2}{3}\left[-\sin(\theta)\lambda_a - \sin\left(\theta - \frac{2\pi}{3}\right)\lambda_b - \sin\left(\theta - \frac{4\pi}{3}\right)\lambda_c\right] \tag{4.12}$$

$$L_{Trial} = L_{Baseline}\left(\frac{\lambda_{PM,Baseline}}{\lambda_{PM,Trial}}\right) \tag{4.13}$$

4.4 Current Selection for Accurate Load Analysis

Evaluating the machine at a desired torque and speed point requires accurate selection of current excitation to get the required output torque. Since FEA requires excitation inputs to derive the torque output, MTPA and flux-weakening control strategies must be implemented to determine the excitation that will result in the desired machine output characteristics. For this reason, a current sweep is conducted across the *d*- and *q*-axis of current values to determine the flux-linkage variation in the machine. To do this CEFEA is performed at each of the current excitation values to obtain the winding three phase flux-linkages as previously described in section 4.2.2, and then a Parkôs transform is performed using (4.14) and (4.15) to get the *d*- and *q*-axis flux-linkage values [40].

$$\lambda_d = \frac{2}{3}\left[\cos(\theta)\lambda_a + \cos\left(\theta - \frac{2\pi}{3}\right)\lambda_b + \cos\left(\theta - \frac{4\pi}{3}\right)\lambda_c\right] \tag{4.14}$$

$$\lambda_q = \frac{2}{3}\left[-\sin(\theta)\lambda_a - \sin\left(\theta - \frac{2\pi}{3}\right)\lambda_b - \sin\left(\theta - \frac{4\pi}{3}\right)\lambda_c\right] \tag{4.15}$$

To perform the *d*- and *q*-axis current excitation sweep, the desired values of excitation are converted into the *abc* reference frame as:

$$I_m = \sqrt{({I_d}^2 + {I_q}^2)} \tag{4.16}$$

$$\gamma = \tan^{-1}\left(I_d / I_q\right) \tag{4.17}$$

The current in ANSYS is provided as pure sinusoidal excitation based on:

$$I_a = I_m \cos\left(t + \gamma\right) \tag{4.18}$$

$$I_b = I_m \cos\left(t + \gamma + \frac{2\pi}{3}\right) \tag{4.19}$$

$$I_c = I_m \cos\left(t + \gamma - \frac{2\pi}{3}\right) \tag{4.20}$$

To estimate the overall variation of the machine parameters, four equidistantly placed samples are obtained in the *q*-axis and three samples are evaluated in the *d*-axis to provide a total of 12 samples. From these samples, the variation of *d*- and *q*-axis flux-linkages is obtained with respect to *d*- and *q*-axis current excitations. Figures 4.10 and 4.11 display the look-up tables created for flux-linkage variation by curve fitting between the given sample points.

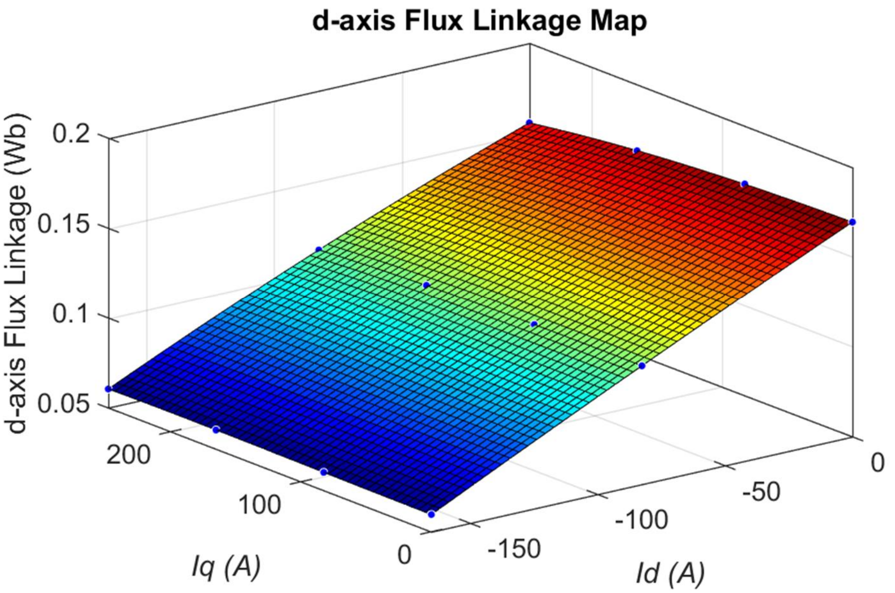

Fig. 4.11. *d*-axis flux-linkage map for varying *d*- and *q*-axis excitations.

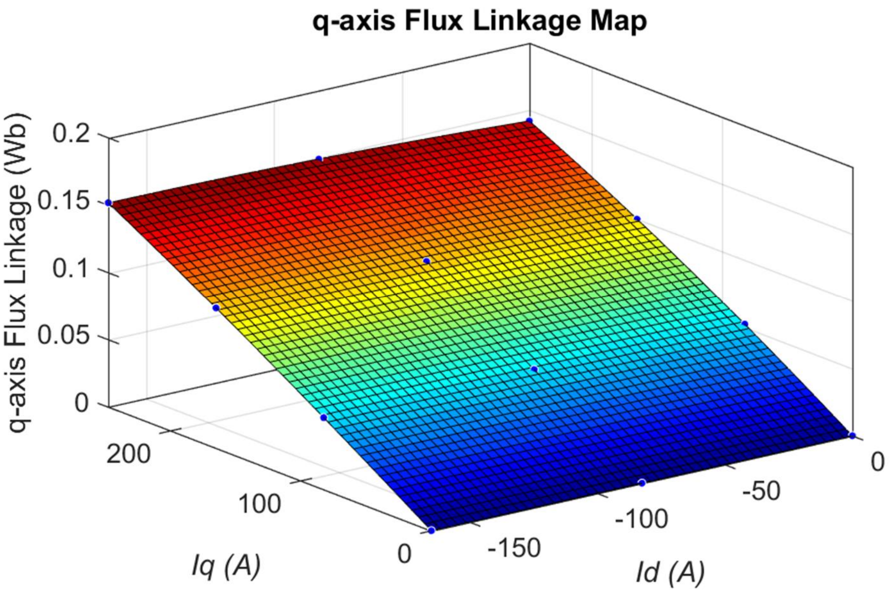

Fig. 4.12. *q*-axis flux-linkage map for varying *d*- and *q*-axis excitations.

From (4.8) and (4.21), the flux-linkages are used to obtain the torque and voltage V as a function of *d*- and *q*-axis current [40].

$$V = \frac{P}{2}\omega\sqrt{(\lambda_d{}^2 + \lambda_q{}^2)} \tag{4.21}$$

Further, curve fitting is implemented to create lookup tables for torque and voltage as a function of *d*- and *q*-axis current as seen in Figs. 4.12 and 4.13. MTPA is implemented by searching the torque lookup table for all possible combinations of *d*- and *q*-axis currents that will provide the desired value of torque and selecting the combination that experiences the lowest magnitude of current. In case of FW operation, the currents that have the lowest magnitude but also satisfy the inverter voltage limit are selected [40].

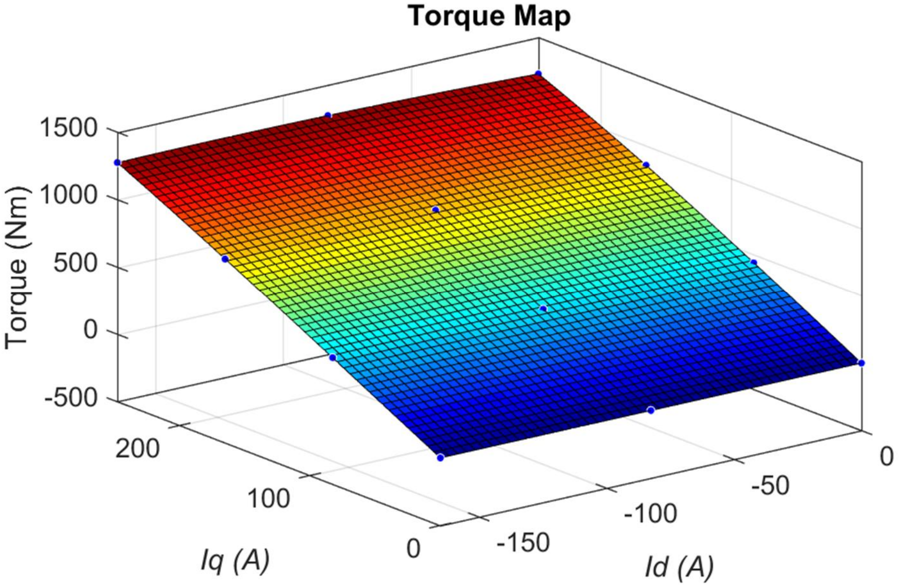

Fig. 4.13. Torque map for varying *d*- and *q*-axis excitations.

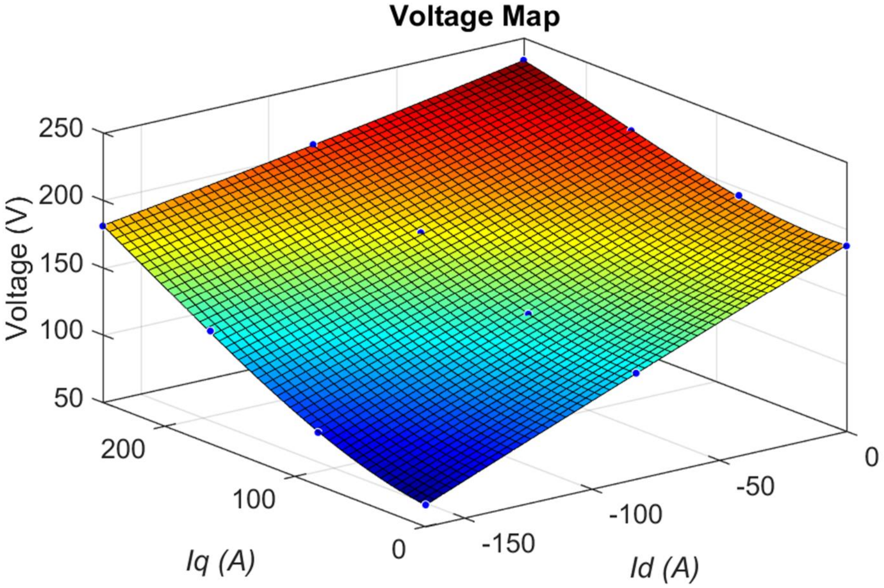

Fig. 4.14. Voltage map for varying *d*- and *q*-axis excitations.

Using the torque and voltage look up tables, the desired current excitations can be selected and the 2D FEA model can be evaluated at each specific loading condition. This guarantees that the desired output torque and speed targets will be met when evaluating the machine at the representative load points and ensures that a fair comparison of performance will be conducted for every generated motor model in the optimization program.

4.5 Loss Analysis

4.5.1 Copper Loss

Copper losses occur due to the electrical resistance associated with the stator windings. Copper losses P_{Cu} are calculated using (4.22), where v is the volume of copper including the end winding, J is the current density, and ρ is the resistivity of copper at the reference temperature of 22°C calculated using (4.23) [41].

$$P_{Cu} = v_{Cu} \rho J^{2} \tag{4.22}$$

$$\rho = 1.724\text{x}10^{-8}\left[1+0.00393\left(Temp-20\right)\right] \tag{4.23}$$

4.5.2 Core Loss

Core or iron loss can be classified into two components known as eddy current loss and hysteresis loss. Both losses are a result of non-ideal properties of the magnetic materials in a magnetic circuit. Eddy currents are closed path circulating currents that are induced in the stator core because of the rotating magnetic field. These circulating currents oppose the magnetic field producing them. Furthermore, the existing resistance produces eddy current losses that are dissipated in the form of heat. Hysteresis losses occur due to the changing magnetic field in the stator core. Ferromagnetic materials become magnetized when excited; however when the excitation is removed, a portion of the magnetization remains in the material. Therefore, extra work has to be performed to alter the direction of magnetization. This is the cause of hysteresis losses that are generated in the ferromagnetic core of the machine.

For core loss determination in the stator core, it is essential to derive the magnitude of flux density. From the magnetostatic solutions, the magnetic vector potentials are used to estimate the predominantly radial flux density in the stator teeth B_{th} and the tangential flux density in the stator yoke B_{yk} as in (4.24) and (4.25). The yoke flux density is determined from the virtual coil around the back iron of the stator that assumes that there is zero magnetic field outside of the motor [30].

$$B_{th} = \frac{A_+ - A_-}{t_w} \tag{4.24}$$

$$B_{yk} = \frac{A_+ - 0}{y_w} \tag{4.25}$$

where t_w is the tooth width and y_w is the yoke width. The resulting waveforms are illustrated in Figs. 4.14 and 4.15. The fundamental components of flux densities are implemented in (4.26) to calculate the specific core loss ɤ in (W/kg) [42].

$$\begin{cases} \omega_h = k_h f B^2 \\ \omega_e = k_e (fB)^2 \end{cases} \tag{4.26}$$

where k_h and k_e are the hysteresis and eddy-current loss coefficients, f is the frequency, and B is the peak flux density. The total core loss, P_{Fe} can be expressed as (4.27), where m_T and m_Y are the masses of the stator teeth and yoke.

$$P_{Fe} = \left(\omega_{hT} + \omega_{eT}\right) m_T + \left(\omega_{hY} + \omega_{eY}\right) m_Y \tag{4.27}$$

4.5.3 Mechanical Loss

In an electric motor, the mechanical losses P_{mech} are predominantly caused by friction and are proportional to ɤ ^{2} as in (4.28), where k_f is the viscous friction coefficient [43].

$$P_{mech} = k_f \omega^2 \tag{4.28}$$

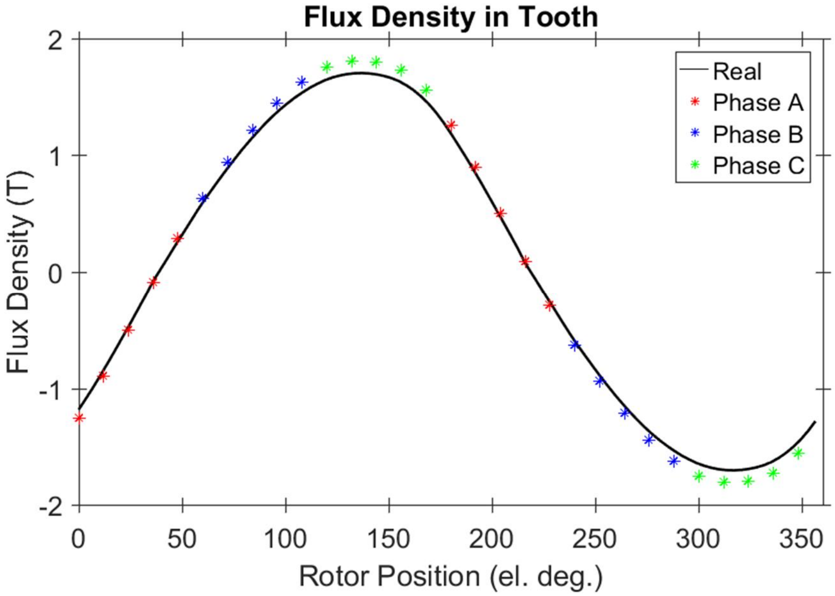

Fig. 4.15. Stator tooth flux density.

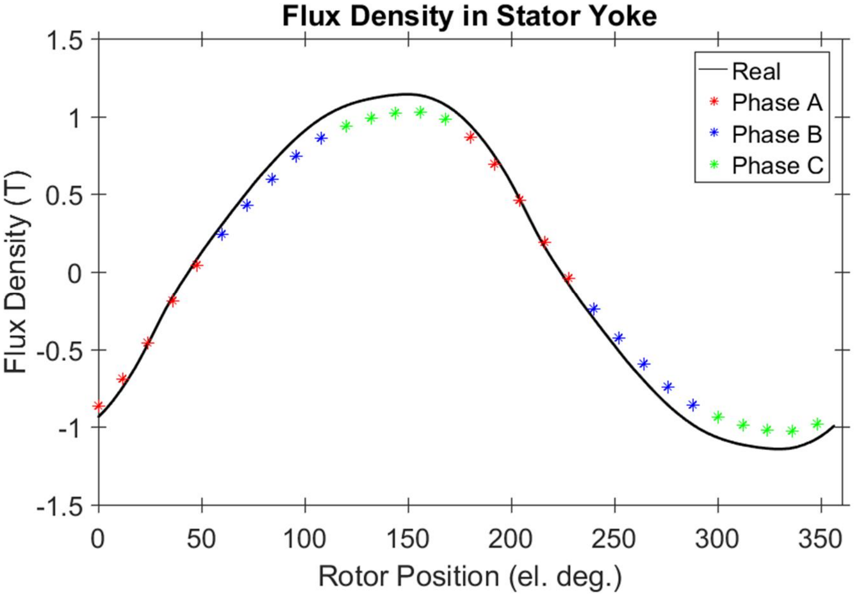

Fig. 4.16. Stator yoke flux density.

4.5.4 Efficiency Calculation

The output power of the machine is calculated using (4.29). The input power is obtained through the summation of the output power with the individual losses as in (4.30).

$$P_{out} = T\omega \tag{4.29}$$

$$P_{in} = T\omega + P_{Cu} + P_{Fe} + P_{mech} \tag{4.30}$$

Therefore, the machineõs efficiency at a given load condition is calculated as:

$$\eta = \frac{P_{out}}{P_{in}} \tag{4.31}$$

To determine the machineôs energy efficiency across the drive-cycle, a weighted efficiency is calculated as in (4.32), using the percentage of normalized energy consumption for each representative cycle point as the weighted significance. This provides a single value to represent the machineôs overall energy efficiency performance across the drive-cycle to be used in the optimization program as an objective [22].

$$\eta_w = \sum_i \frac{T_i \omega_i}{P_{in,i}} E_i \tag{4.32}$$

4.6 Weight and Component Cost Calculation

The weight of a machine is determined by analytically calculating the total volume of permanent magnets, copper, and steel, and multiplying by the density of the corresponding material. The densities of the three materials are listed in Table 4.5 [44] ï [46]. The volume is determined using the machine geometry selected in the optimization algorithm in conjunction with the calculated stack length of the machine.

TABLE 4.5

Density of Materials used in the Direct-Drive Machine

Material	**Density (kg/m^3)**
Magnet - NdFeB 35	7,500
Steel - M19 29G	7,330
Copper	8,616

The cost is calculated as an index based on the mass of material used in the machine. The mass of the permanent magnets m_{PM}, copper m_{Cu}, and steel m_{Fe} are multiplied by a factor dictating the relative cost of the material with respect to M-19 silicon steel used in the core. The manufacturing cost is assumed to be equal for every generated motor model. Therefore, the material cost index c_m calculated in (4.33) is used as a measure to determine whether a given motor topology will have a higher or lower production cost [22].

$$c_m = 24 m_{PM} + 3 m_{Cu} + m_{Fe} \tag{4.33}$$

4.7 Conclusions

The overall machine evaluation procedure is summarized in Fig. 4.16 and the results for the baseline machine using the outlined method is presented in Table 4.6. The CEFEA technique is implemented to make it computationally feasible to consider FEA evaluation results in an optimization program. FEA results provide accurate determination of average torque production and torque ripple generated by the space harmonics in the machine. Furthermore, the stator tooth and yoke flux densities are obtained from the CEFEA technique for core loss calculation.

TABLE 4.6

Baseline Machine Drive-Cycle Efficiency for Resampled K-means Cluster Points

Cluster Point	**Speed (rpm)**	**Torque (Nm)**	**Energy Consumption (%)**	**Efficiency (%)**	**Weighted Efficiency (%)**
1	179.88	730.96	12.29	87.72	10.78
2	293.08	393.57	17.79	94.79	16.86
3	378.37	674.08	8.26	93.60	7.73
4	396.18	150.21	28.62	96.75	27.69
5	510.37	387.39	7.50	96.34	7.23
6	743.61	197.81	25.54	97.18	24.82
Drive-cycle motor energy efficiency:					**95.10**

A *d*- and *q*-axis current sweep procedure that utilizes CEFEA is employed to accurately select current excitations that will provide the desired speed and output torque for the machine at various load conditions. The overall drive-cycle energy efficiency is determined by performing CEFEA at the various representative drive-cycle load points and calculating the copper, core, and mechanical losses in the machine. The drive-cycle energy efficiency, torque ripple, weight, and component cost are evaluated using the outlined procedure and are used as objectives in an optimization program.

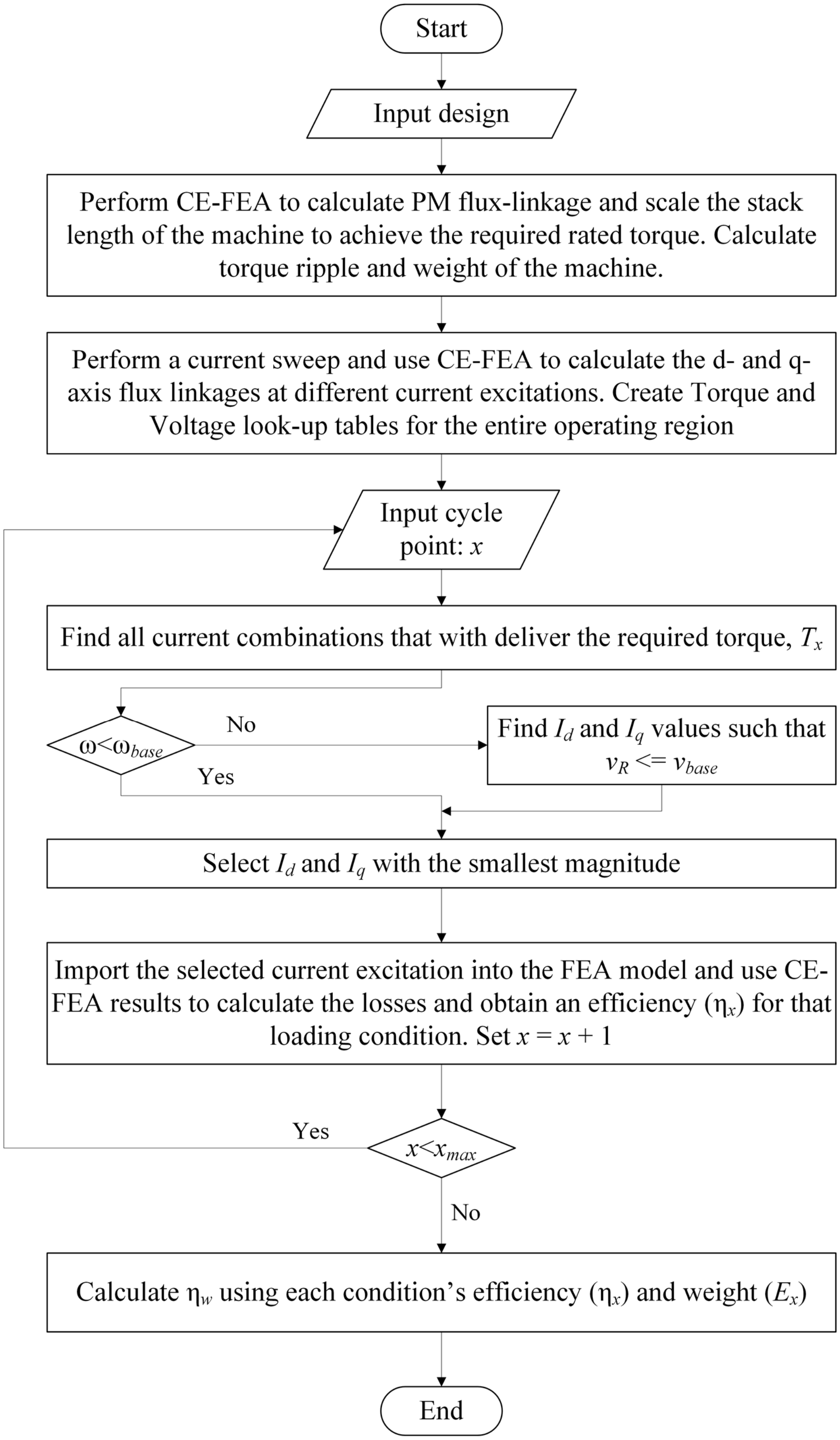

Fig. 4.17. Machine evaluation procedure.

CHAPTER 5

Steady-State Thermal Analysis of Electric Machines

Accurate temperature determination is a crucial aspect in the machine design procedure to ensure safe operating temperatures and to avoid potential motor failure. Temperature must be considered to prevent possible demagnetization of the rare-earth magnets, saturation of the stator and rotor core, and insulation failure in the stator windings [47]. Furthermore, high temperatures are undesirable since they increase the electrical resistance of copper as seen in (4.23). This decreases the overall efficiency of the motor due to the rise in copper loss and in turn, contributes more heat flow into the system.

In an electric motor the various losses detailed in chapter 4, act as a heat flow source and contribute to the temperature rise of the machine during operation. In most modern applications where high power density machines are being designed, a liquid cooling system is incorporated by placing water jackets into the casing of the machine to assist in removing heat from the system.

5.1 Modes of Heat Transfer

When two objects at different temperatures, ɗ, come into contact, heat flow occurs until an equilibrium point is reached where both objects settle at the same temperature. The quantity of heat transferred is represented by H and q defines the amount of heat flow, where $q=dH/dt$. Conduction, convection, and radiation are the three possible modes of heat transfer that occur in any thermal system.

5.1.1 Thermal Conduction

Thermal conduction is the transfer of heat through a medium caused by the collision of particles and molecular motion whenever a temperature gradient is present. Fourierôs law states that conductive heat flow is oriented in the direction of largest temperature difference and is proportional to the rate of decrease. Fourierôs law is given in (5.1), where A is the isothermal surface area perpendicular to the direction of heat flow, k is the thermal conductivity of the medium, and x is the direction of heat flow [48].

$$q = -kA\frac{\partial\theta}{\partial x} \tag{5.1}$$

5.1.2 Thermal Convection

Convection occurs when a surface and a circulating fluid at different temperatures come into contact. Convection is present when heat is flowing to a liquid or a gas where heat transfer occurs through diffusion and bulk fluid flow. Newtonôs law gives the equation for convective heat transfer as (5.2) where ɗ$_s$ is the surface temperature, ɗ$_\infty$ is the fluid temperature, h is the convective heat transfer coefficient. The convective heat transfer coefficient is characterized by the type of fluid motion, surface geometry, fluid thermodynamics and transport properties [48].

$$q = hA\left(\theta_s - \theta_\infty\right) \tag{5.2}$$

5.1.3 Thermal Radiation

Finally, thermal radiation occurs in every object by releasing energy in the form of electromagnetic waves. Stefan Boltzmann law characterizes the energy transfer from a heated object to its surroundings through radiation as in (5.3), where ɗ$_{sur}$ is the absolute temperature of surrounding, ů is the Stefan-Boltzmann, and Ů is the emissivity of the body. In an electric motor the effects of radiation can be neglected since the magnitude of the Boltzmann constant is very small and the temperature differences are not large enough to contribute significant heat transfer through radiation [48].

$$q = \epsilon\sigma A\left(\theta_s^4 - \theta_{sur}^4\right) \tag{5.3}$$

5.2 Lumped Parameter Thermal Network

Thermal systems are in many ways analogous to electric circuits where temperature ɗ is the equivalent on voltage V, heat flow q is equivalent to current I, and heat H is equivalent to charge Q. In this manner, a thermal circuit that models a system in terms of thermal sources, resistances, and capacitances can be constructed. This thermal system can be analyzed using Kirchoffôs circuit laws to calculate temperature at different nodes in the system and the magnitude of heat flow between components in the system. This methodology of constructing a thermal circuit is known as a lumped parameter thermal network. This model is an effective way of representing a thermal system for analytical calculation of temperatures and heat flows in a thermal system.

5.2.1 Thermal Resistance

In any medium, thermal impedance exists that restricts heat flow between two locations of different temperatures. This thermal resistance R_{th} is the ratio between a temperature difference and heat flow as shown in (5.4). Thermal resistance exists for all three modes of heat transfer.

$$\theta_{ij} = R_{th} q \tag{5.4}$$

The thermal resistances for conduction and convection are shown in (5.5) and (5.6) respectively [49].

$$R_{th} = \frac{x}{Ak} \tag{5.5}$$

$$R_{th} = \frac{1}{Ah} \tag{5.6}$$

For conduction through a cylindrical wall, common in an electric motor, the thermal resistance is calculated as [50]:

$$R_{th} = \frac{\ln\left(r_2 / r_1\right)}{2\pi L k} \tag{5.7}$$

5.2.2 Thermal Capacitance

A material's ability to store heat is specified by its specific heat capacity, c_p. Considering a body with a temperature of θ_i and mass m, the heat transferred into the object can be expressed as [50]:

$$q = mc_p \dot{\theta}_i \tag{5.8}$$

Using (5.9) the thermal capacitance C_{th} can be represented as a thermal impedance as in (5.10) where s is the Laplace operator, and θ_{io} is a constant reference temperature.

$$C_{th} = mc_p \tag{5.9}$$

$$\theta_{io} = \left(1/sC_{th}\right)q \tag{5.10}$$

5.2.3 Thermal Sources

An ideal temperature source maintains a constant temperature difference between its terminals. One terminal is allocated to be a reference node. Outdoor or room temperature is often modelled by an ideal temperature source since a thermal system will not cause a temperature change regardless of how much heat it transfers into the atmosphere. A temperature source is analogous to a voltage source in an electrical circuit.

An ideal heat flow source maintains a constant flow of heat q into a node of the thermal system. In an electric vehicle, the losses being generated by the machine are ideal heat flow sources that are injected into the system at the location where they are produced. A heat flow source is analogous to a current source in an electrical circuit.

5.3 Steady-State Temperature Analysis of Electric Machines

To develop a LPTN model for an electric motor, it is essential to understand the machine geometry and the location of the sources of heat flow. Figure 5.1 shows the heat flow path of winding losses through a simplified cross section of a motor. It is important to understand the potential paths of heat flow when creating the network and the different modes of heat transfer the path consists of. In this simple scenario, the heat flow travels through the winding, the core, and the casing through conduction. There is a thermal resistance and capacitance associated with each one of these components on the heat flow path. The thermal resistance dictates the temperature drop between the various materials and the capacitance models the materials ability to heat up or cool down over a duration of time. Finally, from the casing the motor is cooled by convection with the ambient air. As previously stated, the ambient air is an ideal temperature source that does not get affected by the magnitude of heat flow exiting the motor casing. Figure 5.2 shows the full Simulink thermal circuit of the machine that includes the winding heat flow path with the addition of a heat flow source connected at the stator core to represent the core losses. It also contains the rotor loss path that flows through the front and rear bearings to the end caps and finally to the motor casing. It also includes a convection path through the air found in the air gap and around the windings at the end caps of the machine.

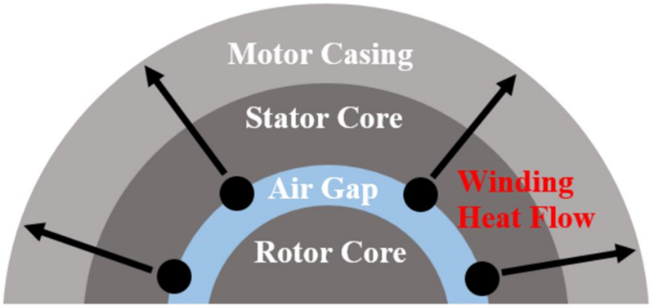

Fig. 5.1. Heat flow path for copper losses in an electric machine.

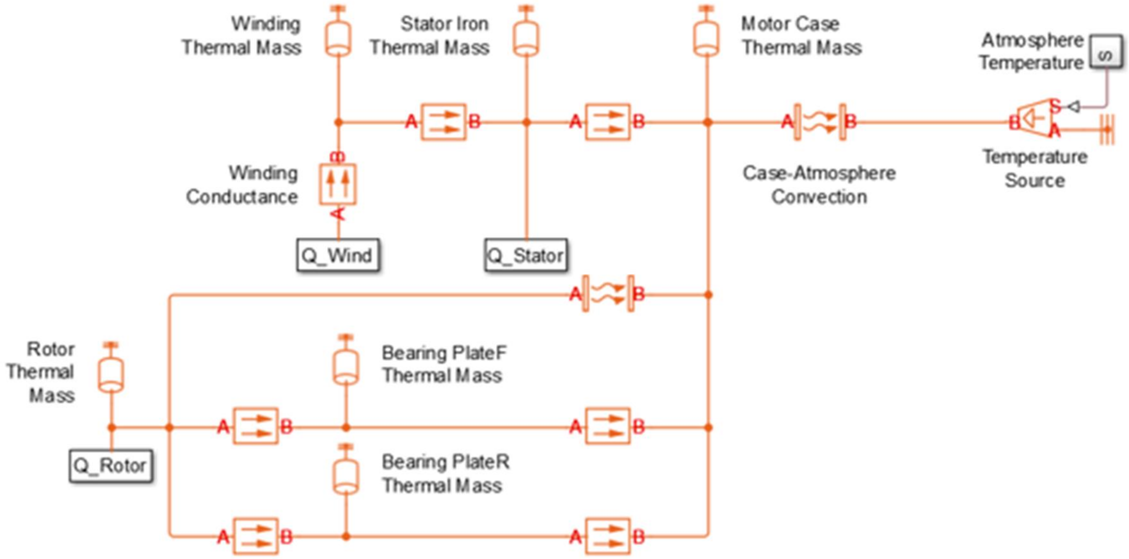

Fig. 5.2. LPTN Simulink model of an electric motor.

Another variation of the thermal can be seen in Fig. 5.3. The thermal capacitances make analytically solving the thermal circuit difficult because of its transient behaviour. Therefore, the steady-state solution is used to evaluate the final value for the temperatures at each node within the machine. This type of solution is sufficient for being implemented into an optimization algorithm since it is computationally efficient and the steady-state value is the most severe and significant point to consider in an operational machine.

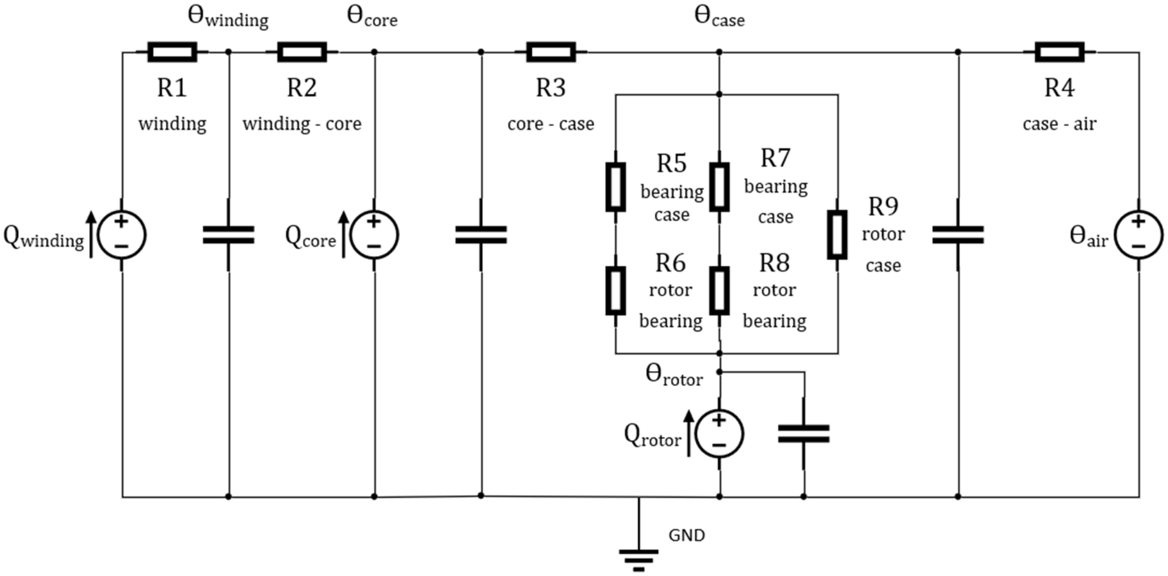

Fig. 5.3. Thermal circuit of an electric machine.

Figure 5.4 displays the steady-state thermal circuit, where the capacitors become fully charge and can be replaced with an open circuit. Using superposition theorem, the steady-state temperatures can be derived at various nodes in the machine as in (5.11) ï (5.14). These equations are implemented into the optimization algorithm and are considered as another design criteria when selecting the optimized machine.

$$\theta_{case} = \left(\left(Q_{winding} + Q_{core} + Q_{rotor} \right) R_4 \right) + \theta_{air} \tag{5.11}$$

$$\theta_{rotor} = \left(Q_{rotor} \, R_{eq} \right) + \theta_{case} \tag{5.12}$$

$$\text{where: } R_{eq} = \left[\left(R_5 + R_6 \right) \left(R_7 + R_8 \right) \right] R_9$$

$$\theta_{core} = \left(\left(Q_{winding} + Q_{core} \right) R_3 \right) + \theta_{case} \tag{5.13}$$

$$\theta_{winding} = \left(Q_{winding} \, R_2 \right) + \theta_{core} \tag{5.14}$$

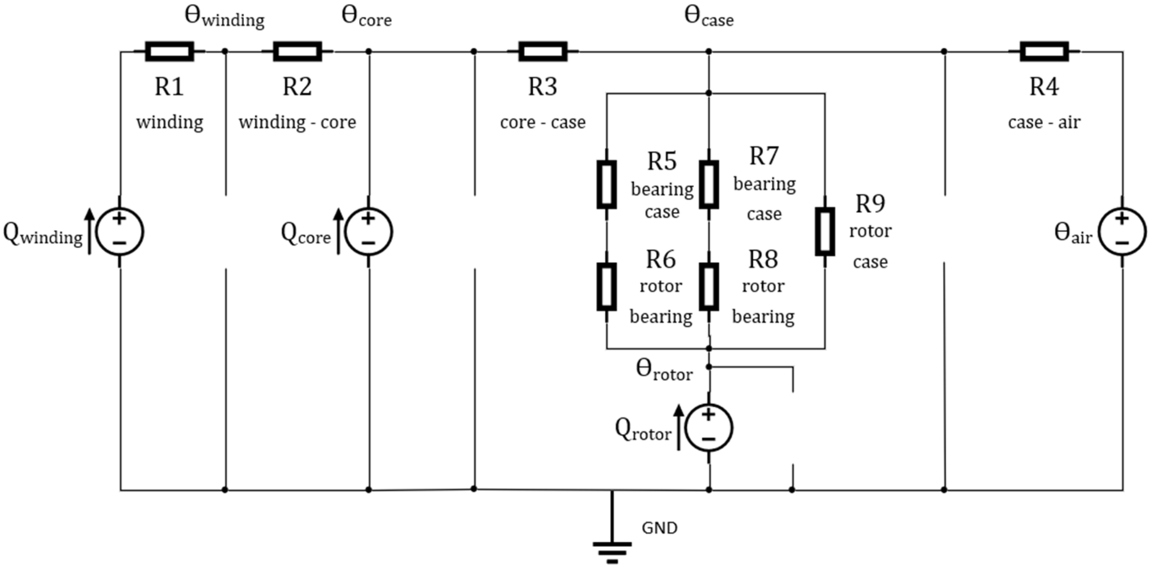

Fig. 5.4. Steady-state thermal circuit of an electric machine.

To calculate the thermal resistances the thermal conductivities listed in Table 5.1 are used for the materials used in the baseline SPMSM [46], [51]. The convective heat transfer coefficient of 40 W/m^{2}K is assumed for natural convection and 120 W/m^{2}K is used for forced air cooling at 20 m/s [51]. The steady-state temperature results for the winding, rotor, core and motor casing with forced air cooling are summarized in Table 5.2. The table shows results for numerous drive-cycle load conditions to indicate temperature variations within the machine with respect to the output torque and speed of the machine.

TABLE 5.1

Thermal Conductivity of Components in the Direct-Drive Machine

Material	**Thermal Conductivity (W/m·K)**
Copper	403
Steel - M19 29G	22.8
Aluminum	167
Bearings	44.5
Shaft	49.8

TABLE 5.2

Steady-State Temperature Results of the Direct-Drive Machine at Various Load Conditions

Operating Condition	Speed (rpm)	Torque (Nm)	$\theta_{winding}$ (°C)	θ_{rotor} (°C)	θ_{case} (°C)	θ_{core} (°C)
Rated Conditions	575	857	101.66	106.65	84.88	87.14
Cluster Point 1	179.88	730.96	74.69	68.52	62.70	64.26
Cluster Point 2	293.08	393.57	42.37	44.08	39.04	39.51
Cluster Point 3	378.37	674.08	70.96	72.08	60.81	62.17
Cluster Point 4	396.18	150.21	31.17	33.20	30.64	30.77
Cluster Point 5	510.37	387.39	44.58	49.95	41.31	41.81
Cluster Point 6	743.61	197.81	35.91	41.32	34.96	35.21

5.4 Conclusions

This chapter proposed a steady-state thermal analysis for a computationally efficient method of determining temperatures in different regions of the machine at different operating conditions. The proposed method calculates the thermal resistances for different paths in the machine by considering the motor geometry and the material properties. Further, the losses determined in the machine evaluation procedure outlined in chapter 4 are injected into the thermal circuit as heat sources. Superposition theorem is applied to calculate the steady-state operating temperatures in the machine for a given load condition.

The results displayed in Table 5.2 illustrate the temperature variation at the different cluster points for the baseline direct-drive machine. The temperatures are generally proportional to the magnitude of output torque since there is a large value of current in these conditions that generate copper losses in the machine. The geometry of the machine will have an effect on the values of temperature by modifying the thermal resistances in the thermal circuit. A large machine will reduce the temperatures since there will be a larger cooling surface for heat to dissipate.

CHAPTER 6

Multi-Objective Drive-Cycle Based Optimization

6.1 Multi-Objective Differential Evolution

Chapters 4 and 5 introduced design evaluation techniques for drive-cycle energy efficiency, torque ripple, weight, component cost, and temperature determination that will be implemented into an optimization algorithm to evaluate and select optimal machine design candidates in terms of those objectives. Optimization algorithms are employed to find a globally optimal design based on set of optimization parameters, constraints, and objectives. Differential evolution is an evolutionary algorithm that optimizes by iteratively creating new design candidates that compete against a parent population to determine the offspring. Differential evolution optimization is selected based on an improved convergence rate compared to other optimization schemes such as genetic algorithm [52].

6.1.1 Initial Population

To initialize the optimization, a population, P that contains N_p individuals is generated with randomly selected design parameters, x. For electric motor optimization, the individuals of this population are various motor topologies and the design parameters are the various geometrical attributes of the machine that are being manipulated. The geometrical parameters are confined within an upper and lower limit to ensure that feasible design candidates are being generated. The process for randomly selecting a design parameter within the set boundaries is shown in (6.1) where $\alpha_j \in [0, 1]$ is a random number and b_j^U and b_j^L are the upper and lower bounds of the j^{th} design parameter. This is repeated for each design parameter of a machine and for each motor in the population.

$$x_j = b_j^L + \alpha_j \left(b_j^U - b_j^L \right) \tag{6.1}$$

The initial population is evaluated using the procedure outlined in chapter 4 to measure the effectiveness of the individual motor models in terms of the objectives. This population is used to create the next group of trial designs with which they will compete to form the offspring population.

6.1.2 Creation of Trial Design Candidates

The generation of a mutant vector, x^v is the first step to creating a trial design. This requires taking three randomly selected members of the population such as x^0, x^1, and x^2 to create the design parameters of the mutant vector using (6.2).

$$x^v = x^0 + F\left(x^1 - x^2\right) \tag{6.2}$$

$$x^0 \neq x^1 \neq x^2$$

where $F \in [0, 1]$ is the mutation intensity. The design parameters of the base vector x^0 are altered by the difference between the two individuals x^1 and x^2. This initially produces a large variation of design parameters in the early stages of the optimization algorithm by mixing the design parameters to search the entire design space. However, it also allows for convergence in the later stages of the optimization when there is little variation between the population members.

A crossover operation is performed between the parent P and the mutant vector expressed in (6.3) to generate the child c where $C_r \in [0, 1]$ is the crossover probability.

$$c_j = \begin{cases} x_j^v \; if \; \alpha_j \leq C_r \\ P_j \; otherwise \end{cases} \tag{6.3}$$

Finally, a regularization of infeasible mutants is performed to ensure that all generated design parameters are fixed within the corresponding upper and lower boundaries. The design parameter in the mutant vector is randomly assigned a feasible value if it violates an upper or lower limit as in (6.4). The child must compete with the parent from the present population to join the next generation. Each of these machines is evaluated for the set constraint and objectives using the evaluation method outlined in chapter 4.

$$c_j = \begin{cases} x_j = b_j^L + \alpha_j\left(b_j^U - b_j^L\right) if \; c_j < b_j^L \\ x_j = b_j^L + \alpha_j\left(b_j^U - b_j^L\right) if \; c_j > b_j^U \end{cases} \tag{6.4}$$

6.1.3 Logical Dominance Function

A logical dominance function is utilized to determine whether child is dominant over the parent. This determines whether the parent will be replaced by the child that was created by the optimization in the following generation. The main focus of the logical dominance function is the constraints and objectives. Constraints allow the optimization to exclude certain design candidates that are of no interest to the optimizer. For example, having an electric motor that produces less than 5% torque ripple for industry standards is a constraint. Objectives are the main targets of optimization such as maximizing efficiency and minimizing cost. Thus, the logical dominance function replaces the parent with the child in the following conditions [52]:

1. If both c and P are infeasible, but c violates fewer constraints.
2. If c is feasible while P is infeasible.
3. Both c and P are feasible, but c is better than P in terms of objective function values.

6.1.4 Termination Condition

The termination condition allows the iterative optimization algorithm to break its loop. For this electric machine optimization, it is set to exit when there is no longer any variation in the population or until a maximum number of generations is met. The overall flowchart of the optimization procedure is shown in Fig. 6.1.

6.2 Optimization Parameters, Constraints, and Objectives

The 2D cross section of the machine in Fig. 6.2 displays the parameters selected to be manipulated during the optimization. The program utilizes five parameters to optimize the machine, which include: turns per coil (T_{coil}), rotor outer diameter (D_{ro}), tooth width (W_t), slot opening (W_{so}), and magnet angle ($\breve{U}_{PM}$). As a consequence of these variations, variables including the stator and rotor inner diameter, slot widths and height, and stator yoke width are indirectly affected. These changes are made to maintain a constant slot fill factor of 60% and a constant air gap length, magnet height, and rotor yoke width.

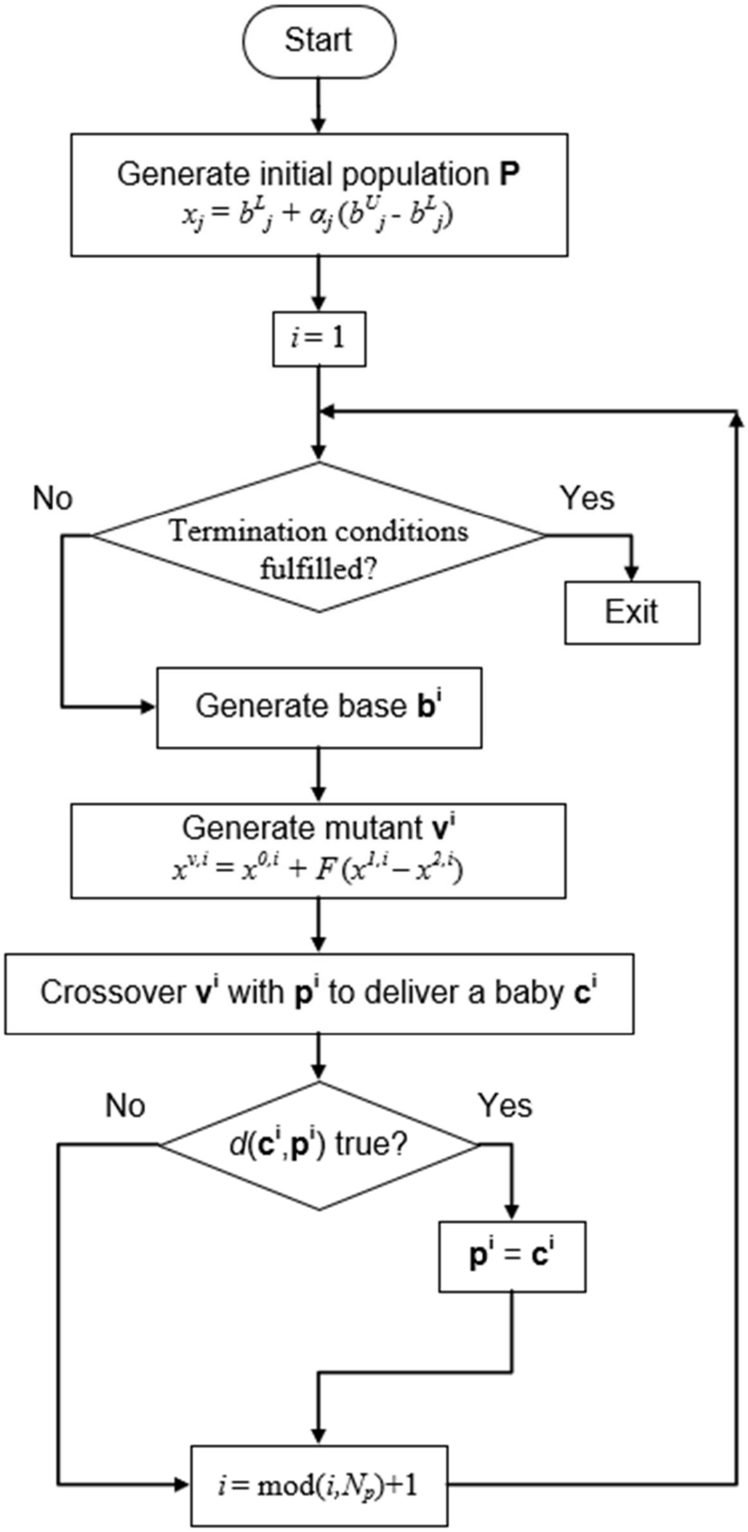

Fig. 6.1. Multi-objective differential evolution flowchart.

The torque capability of the machine is affected by the turns per phase and the rotor outer diameter. These parameters are selected in an attempt to reduce the volume, weight, and cost of the machine [53]. A FSCW winding configuration is also known to produce a large amount of space harmonics that cause torque ripple and are a large contributor to magnet loss. The tooth width, slot opening, and magnet angle are selected as optimization parameters in an attempt to reduce the amount of space harmonics present in the machine [54].

The parameters and their constraints are summarized in Table 6.1. These constraints are created to keep the design variables within allowable limits and ensure that every machine design created in the optimization program has a viable configuration with no overlapping components. The upper limit of the tooth width is calculated to have a minimum of 5 mm for the stator yoke depth after the slot depth is calculated to satisfy the area requirement necessary to get a 60% slot fill factor.

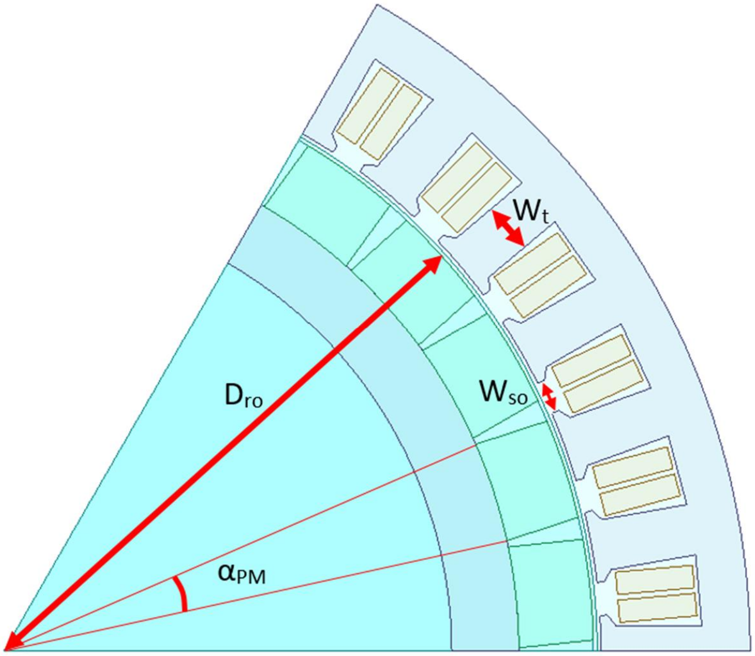

Fig. 6.2. Optimization parameters selected for baseline machine.

TABLE 6.1

Optimization Parameters and Limits

Parameter	Minimum	Maximum
T_{coil}	5	9
D_{ro}	286 mm	346 mm
W_t	8 mm	Variable
W_{so}	5 mm	11 mm
$Ŭ_{PM}$	6ę	12ę

The machine is constrained to a torque ripple that is less than 5% at rated conditions and a weight that is less than 65 kg. The overall objectives of the optimization are to:

- Maximize drive-cycle energy efficiency
- Minimize torque ripple at rated conditions
- Minimize weight
- Minimize component cost
- Minimize average steady state drive-cycle winding temperature

These objectives are evaluated based on the FEA procedure outlined in Chapter 4.

6.3 Optimization Results

The optimization program uses an initial population size of 25 candidates and executes for 25 generations to evaluate a total of 625 machine models. The optimization is performed for the two drive-cycle representation methods summarized in chapter 3 in order to perform a comparative analysis of the effectiveness of drive-cycle representation based off the optimization results.

A Pareto front of optimal solutions using the resampled K-means clustering method is created and displayed in Fig. 6.3. A design candidate is excluded from the Pareto set if it is lower for every objective compared to other designs. A Pareto front is utilized to observe the trade-offs that exist between the multiple objectives. It assists in selecting optimal solutions. Figure 6.3(a) shows how efficiency increases almost proportionally with weight and cost. Figure 6.3(b) displays the variation in torque ripple is mainly caused by the changes in slot opening width and overall slot dimensions. Finally, Figure 6.3(c) shows how the average steady-state winding temperature across the drive-cycle points decreases with an increase in efficiency and size of the machine. This is explained by the decrease of heat production with increasing efficiency and the increase in surface area for cooling in larger machines.

Tables 6.2 and 6.3 contain the optimization results for the two drive-cycle representation methods that maximize each objective. The trade-off between the objectives is evident by the large variation in objective evaluations between each of the maximized results. Figure 6.4 shows the continuous torque waveforms obtained using FEA to compare the baseline machine to the optimized motor in terms of torque ripple. The reduced torque ripple will also increase the efficiency by reducing the harmonic losses that are not considered in the proposed loss model.

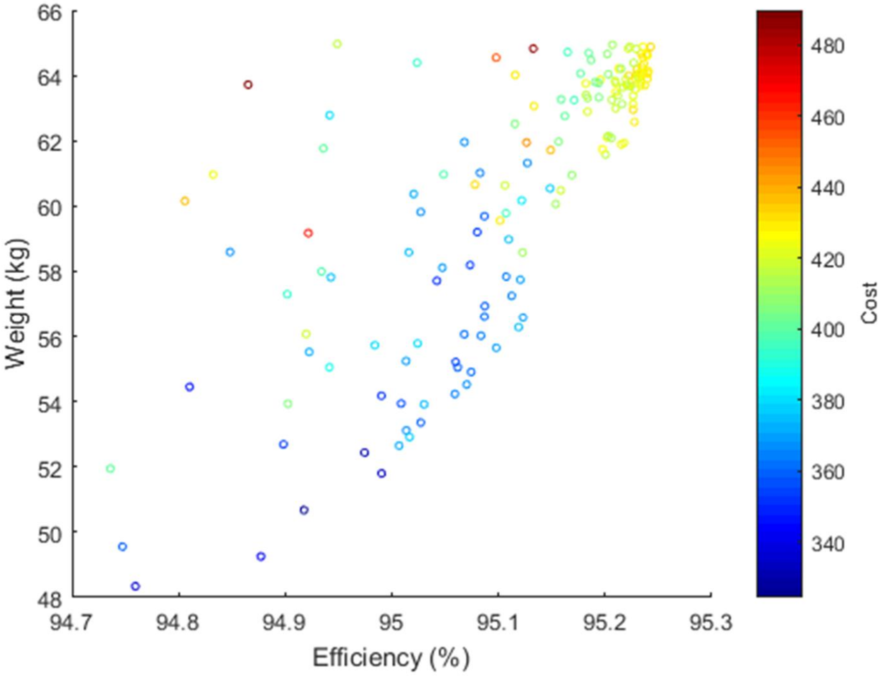

(a) Weight vs. drive-cycle energy efficiency with colour coded cost.

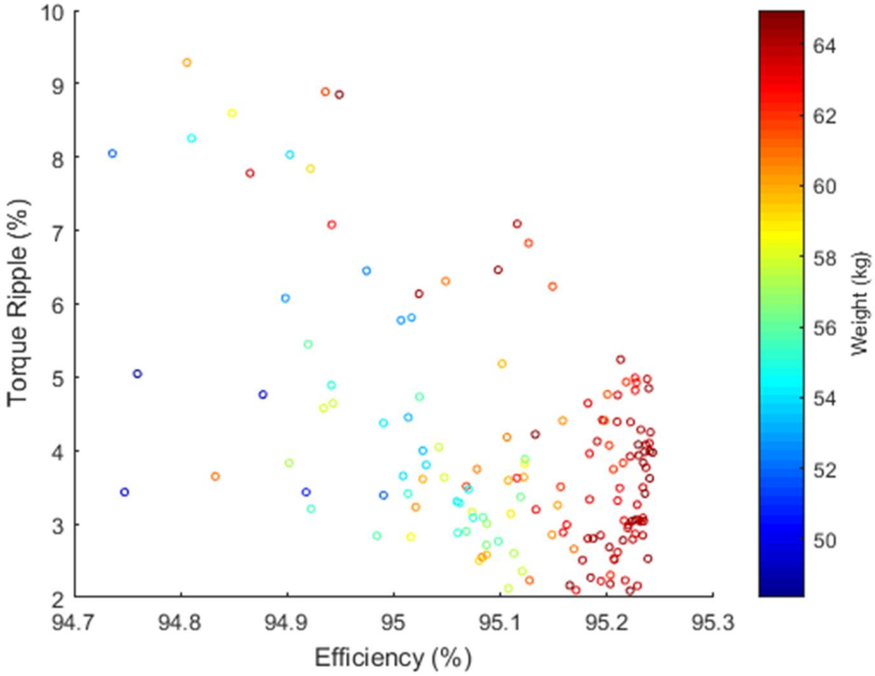

(b) Torque ripple vs. drive-cycle energy efficiency with colour coded weight.

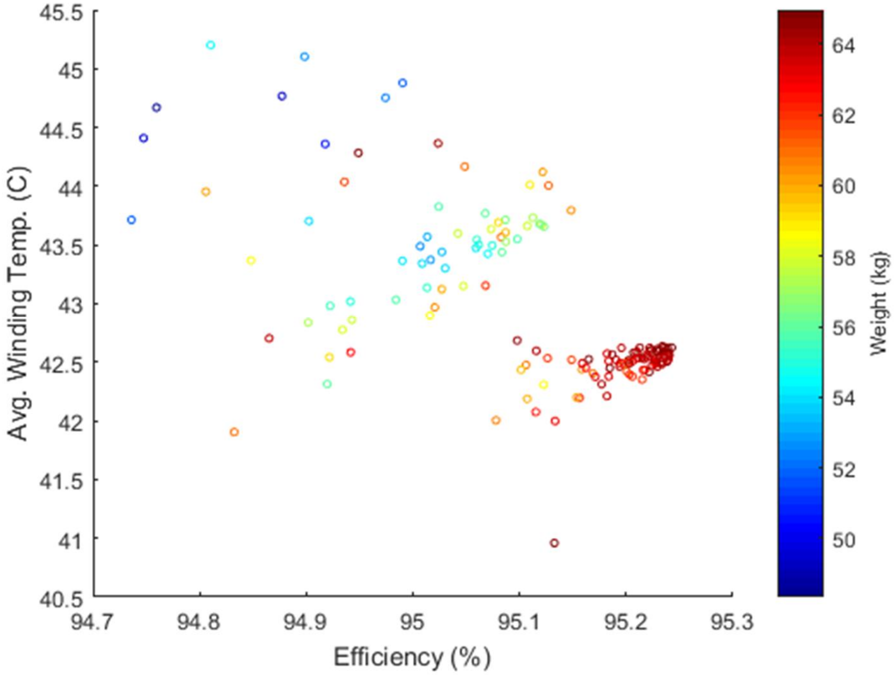

(c) Average steady-state winding temperature vs. drive-cycle energy efficiency with colour coded weight.

Fig. 6.3. Optimization results using the resampled K-means clustering drive-cycle points.

TABLE 6.2

K-means Results for Maximized Objectives

Weighted Eff. (%)	**95.24**	95.22	94.76	94.92	95.13
Torque Ripple (%)	3.97	**2.09**	4.98	3.43	4.22
Weight (kg)	64.87	64.82	**48.34**	50.67	64.83
Cost	431.95	421.92	337.04	**324.35**	487.17
Avg. Winding Temp. (C)	42.62	42.41	44.67	44.36	**40.96**

TABLE 6.3

GMM Results for Maximized Objectives

Weighted Eff. (%)	**95.47**	95.34	95.01	95.19	95.35
Torque Ripple (%)	3.71	**2.07**	4.28	4.18	4.92
Weight (kg)	64.31	63.19	**48.19**	54.44	64.42
Cost	424.62	368.99	336.18	**319.39**	508.06
Avg. Winding Temp. (C)	41.94	43.12	43.93	43.44	**40.51**

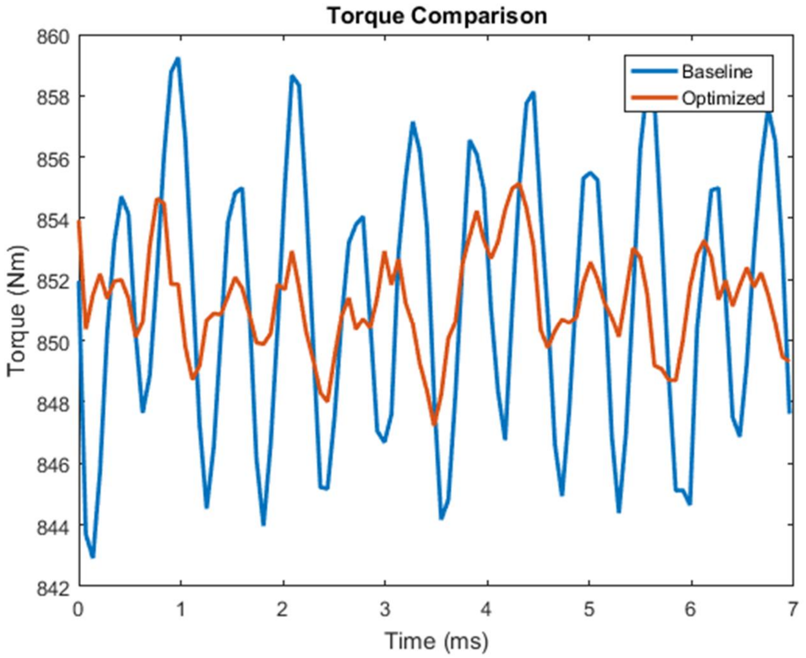

Fig. 6.4. FEA waveforms displaying torque ripple of baseline and optimized machine.

Table 6.4 displays the increase in motor drive-cycle energy efficiency between the baseline machine and the maximized efficiency results of each drive-cycle representation method. The columns display the performance evaluation based on the weighted efficiency for both the baseline and optimized machine for each representation method.

TABLE 6.4

Drive-Cycle Energy Efficiency Derived from Representative Load Points

Method	**Baseline Efficiency (%)**	**Optimized Efficiency (%)**
Resampled K-means	95.10	95.24
Resampled GMM	95.34	95.47

From Table 6.4, it can be seen that the baseline machine experiences a different value of efficiency for each method. Therefore, for an accurate comparison of the results, the machines must be tested in the same manner to properly assess the overall effectiveness of each approach. For this reason, each machine is evaluated at all points of the drive-cycle rather than the representative points using the evaluation method explained in chapter 4. This type of analysis is computationally intensive, however it possible since there are only three optimal machine topologies that need to be evaluated. The results for both the dimensions and weighted energy efficiencies are summarized in Table 6.5.

TABLE 6.5

Optimized Motor Parameters for Drive-Cycle Efficiency

Parameter	**Baseline Machine**	**Resampled K-means**	**Resampled GMM**
T_{coil}	7	6	6
D_{ro}	316 mm	319 mm	319 mm
W_t	13.6 mm	14.9 mm	15.6 mm
W_{so}	8.9 mm	7.7 mm	7.0 mm
Ŭ_{PM}	8.59ę	9.83ę	9.87ę
Eff. (%)	94.64	95.55	95.62

6.4 Conclusions

The optimization was performed twice to optimize drive-cycle energy efficiency using the resampled dataset for both K-means clustering and Gaussian mixture modelling. The GMM method provided the optimal results for drive-cycle motor energy efficiency by increasing from 94.64% to 95.62% across the entire cycle. The plots of optimized solutions in Fig. 6.3 contain all the trade-offs that exist to enhance the machine in terms of drive-cycle energy efficiency, torque ripple, weight, cost, and average winding temperature. It can be seen from the results in Tables 6.2 and 6.3 that a more drastic improvement can be obtained in terms of the weight and cost of the machine or with the torque ripple and average winding temperature in comparison to the efficiency improvement. Machines with a lower weight will require less power across the drive-cycle by reducing the tire friction force, force of acceleration, and gravitational force in the vehicle dynamics equation. A reduced torque ripple will decrease the noise and vibrations of the machine, but will also lessen the amount of harmonic losses in the machine. Therefore, these objectives may lead to further improvements in the overall drive-cycle motor energy efficiency.

The optimization results prove the effectiveness of the drive-cycle representation methods for evaluating drive-cycle motor efficiency. In addition, the multi-objective optimization program that utilizes CEFEA is found to provide accurate performance evaluations for the most suitable machines in the design space. It is an essential component of a machine design procedure to eliminate any assumptions in the design process and ensure that optimal motors are being designed for a certain set of objectives.

CHAPTER 7

Drive-Cycle Analysis of Inverter Fed Machines

An inverter that employs pulse-width modulation (PWM) to produce a three-phase voltage excitation to the motor is used to supply power to modern PMSMs in an electric vehicle. This PWM excitation seen in Fig. 7.1 is a series of varying width square-wave pulses that gets applied to the terminals of the electric machine. Switches that control the polarity of the DC excitation supplied at the motor terminals generate the PWM signal. The switches are toggled on and off by gate pulses that are determined by comparing a triangular carrier waveform to the desired sinusoidal voltage waveform as seen in Fig. 7.2. The motor leakage inductance acts as an inductive low-pass filter operating on the stator winding excitation to produce a relatively sinusoidal waveform. Existing harmonics in the current waveform being supplied to the motor from the inverter are classified as time harmonics [55].

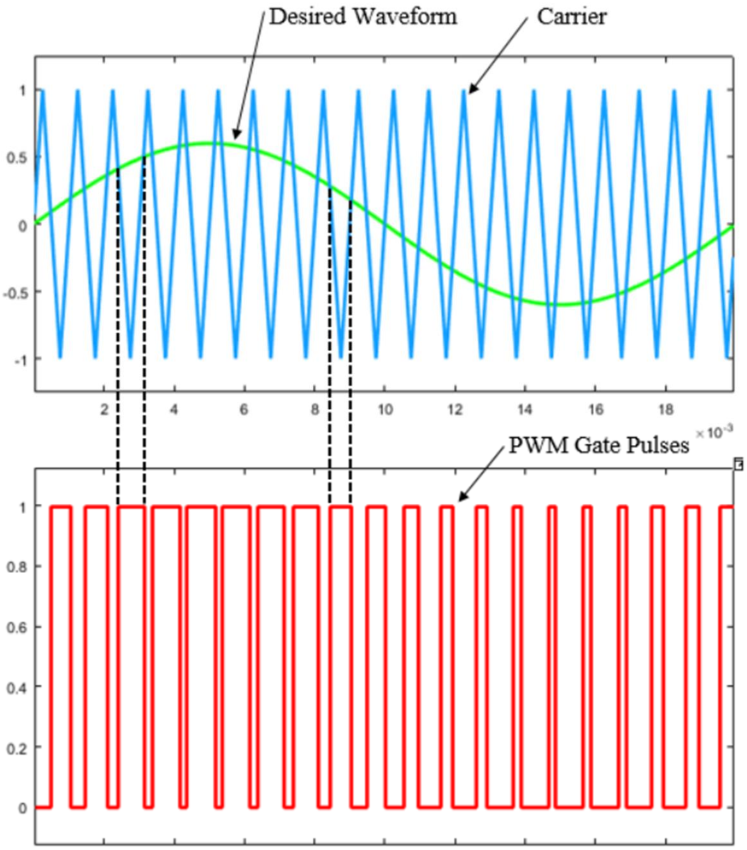

Fig. 7.1. PWM gate pulses generated by comparing a triangular carrier wave with the desired waveform.

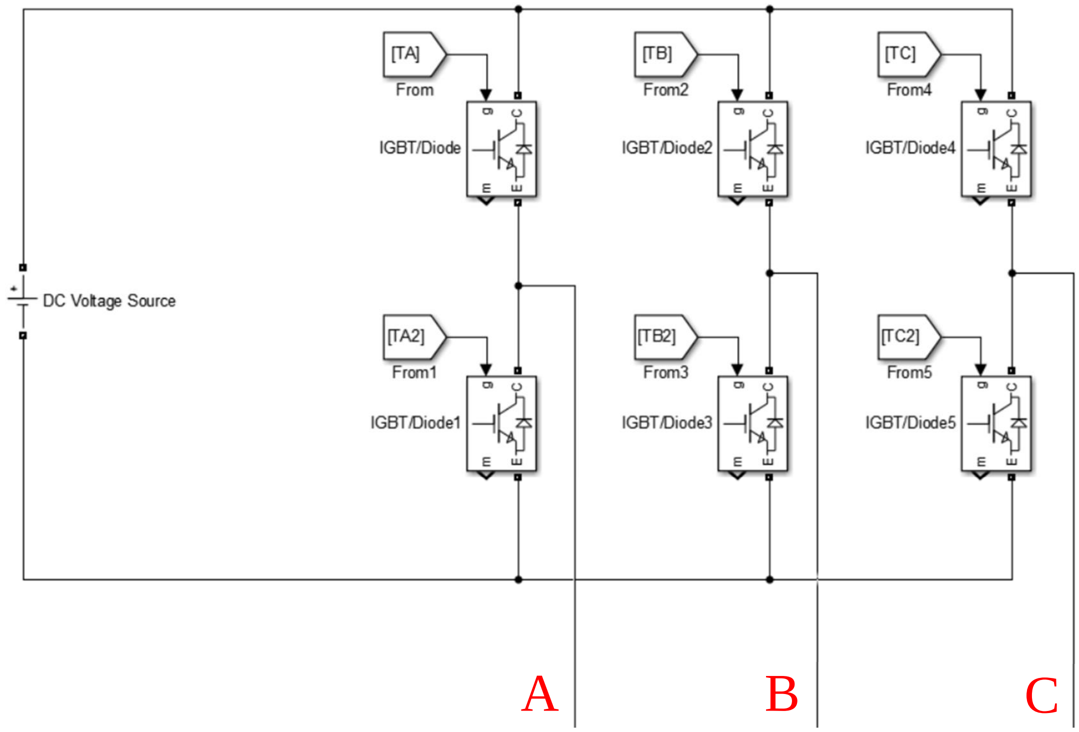

Fig. 7.2. Typical configuration of a two-level inverter.

Research is being conducted on gallium-nitride high electron mobility transistors (HEMT) to replace the commonly implemented insulated-gate bipolar transistor switches in automotive inverters [56]. GaN is an appealing candidate for automotive inverter implementation due to its reduced switching losses, weight, and volume [57], [58]. Furthermore, GaNôs fast switching characteristics enable for high frequency operation that is beneficial for the reduction of time harmonics in the current excitation supplied to the electric motor. This implies that GaN inverters will improve motor operation by minimizing torque ripple and losses produced by the time harmonics being injected from the inverter [59].

This chapter introduces a method of using simulation tools to quantify the benefit of GaN inverters in comparison to IGBT inverters with respect to motor performance. Figure 7.3 outlines the procedure to conduct this comparative analysis. Initially, the vehicle loading analysis and K-means clustering technique outlined in chapter 3 is applied to obtain drive-cycle representative points and predict the efficiency improvement that will be obtained from employing GaN devices in a real vehicle drive-cycle application. This will significantly reduce the drive-cycle evaluation time since the simulations are realistically too computationally intensive to evaluate for the entire cycle. ANSYS is used to determine machine parameters at the representative load points to properly model the current excitations and motor load in PSIM considering the machine non-linearities. Further, a current controlled inverter fed motor simulation is developed in PSIM to obtain motor-fed current excitations that include the time harmonics produced by the PWM voltage excitation. Finally, the harmonic rich current excitations are fed into ANSYS to assess the torque ripple and loss variation in the machine. This procedure is conducted for an IGBT and GaN two level inverter and the results are compared with analytically determined pure sinusoidal current excitation.

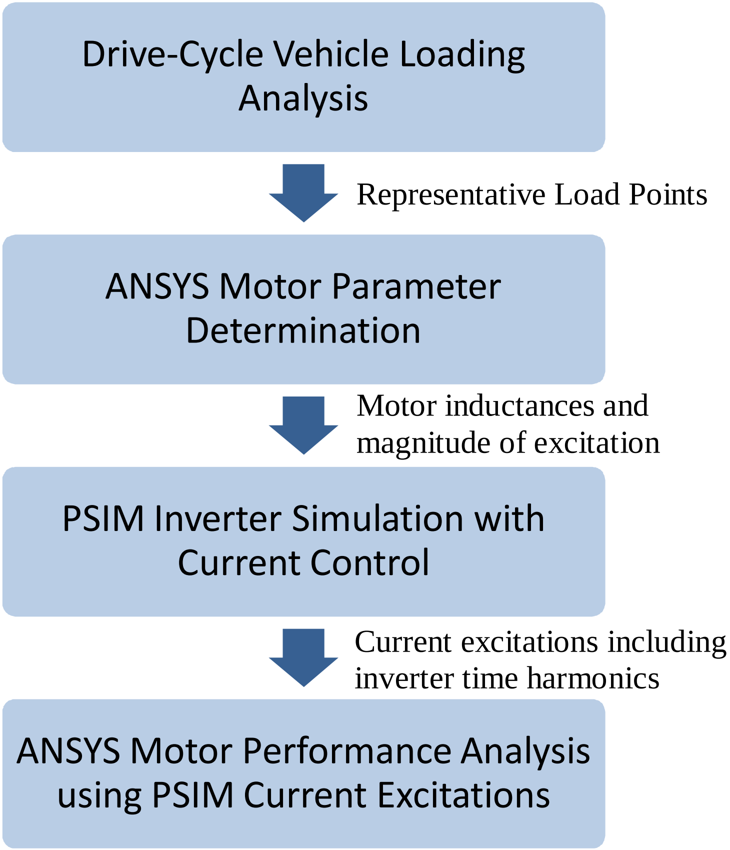

Fig. 7.3. Flowchart for IGBT and GaN comparison on motor performance.

7.1 UDDS Drive-Cycle Vehicle Loading Analysis

For the analysis of the effects of inverter generated on an electric motor, a 12-slot 14-pole FSCW SPM machine is used. The motor ratings are listed in Table 7.1 and a cross-sectional view of the machine is shown in Fig. 7.4.

TABLE 7.1

Motor Specifications for Inverter Simulation

Slots	12
Poles	14
Peak Power	92 kW
Peak Torque	293 Nm
Base Speed	3000 rpm
Max. Speed	9000 rpm

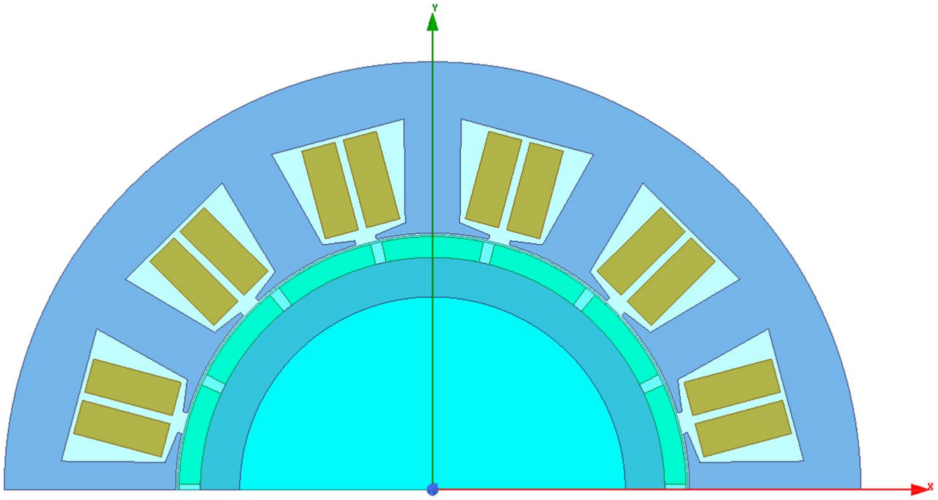

Fig. 7.4. Cross-section of 12/14 SPM used for the system level investigation.

For a drive-cycle evaluation the loading analysis procedure outlined in chapter 2 is repeated for the vehicle parameters listed in Table 7.2.

TABLE 7.2

Vehicle Specifications

Symbol	**Description**	**Value**
Ɉ	Density of air	1.202 kg/m^3
C_d	Drag coefficient	0.33
A_v	Frontal vehicle surface area	2.77 m^2
v	Vehicle speed	varying
f_{rr}	Rolling resistance coefficient	0.013
M_v	Vehicle mass	1700 kg
g	Gravitational acceleration	9.81 m/s^2
Ŭ	Road grade	3°
r	Wheel Radius	0.3284 m
i_g	Gear Ratio	7.25

The results for shaft speed, torque, mechanical output power, and energy distribution are shown in Figs. 7.5 ï 7.8. The motor has a fixed gear ratio between the motor shaft and the wheel of the vehicle. Therefore the electric motor operates at higher speed and lower torques in comparison to the direct-drive machine described in chapter 4.

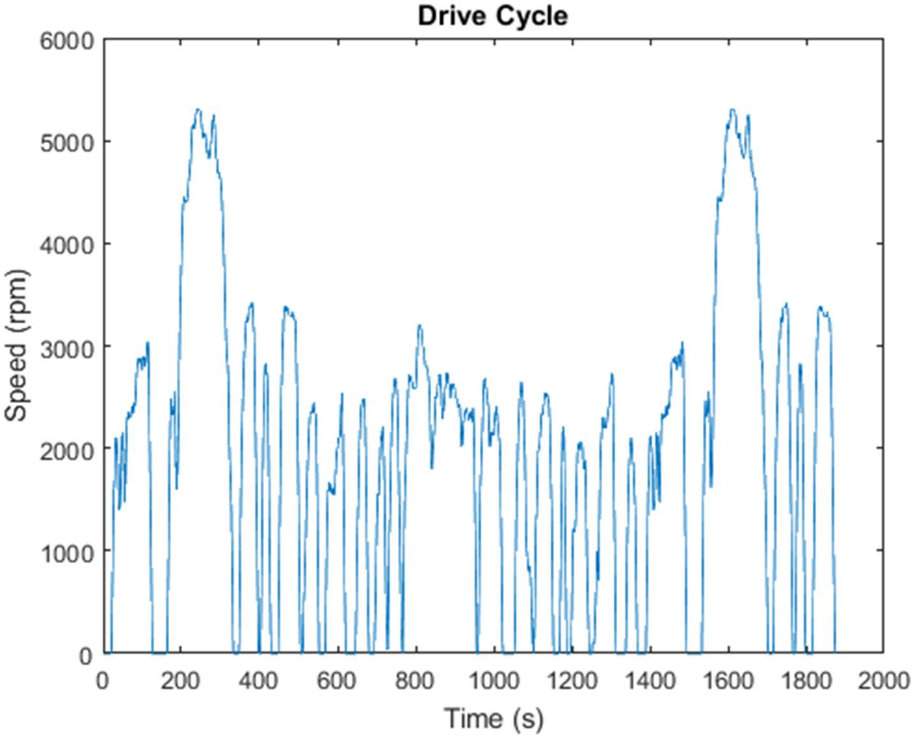

Fig. 7.5. UDDS motor speed obtained for 12/14 SPM.

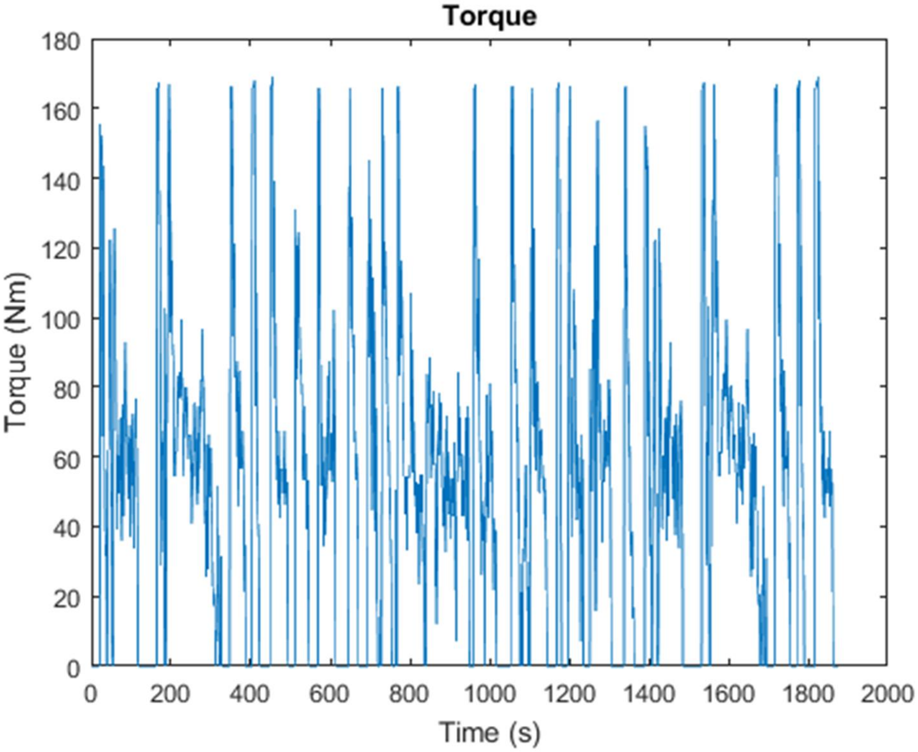

Fig. 7.6. UDDS motor torque obtained for 12/14 SPM

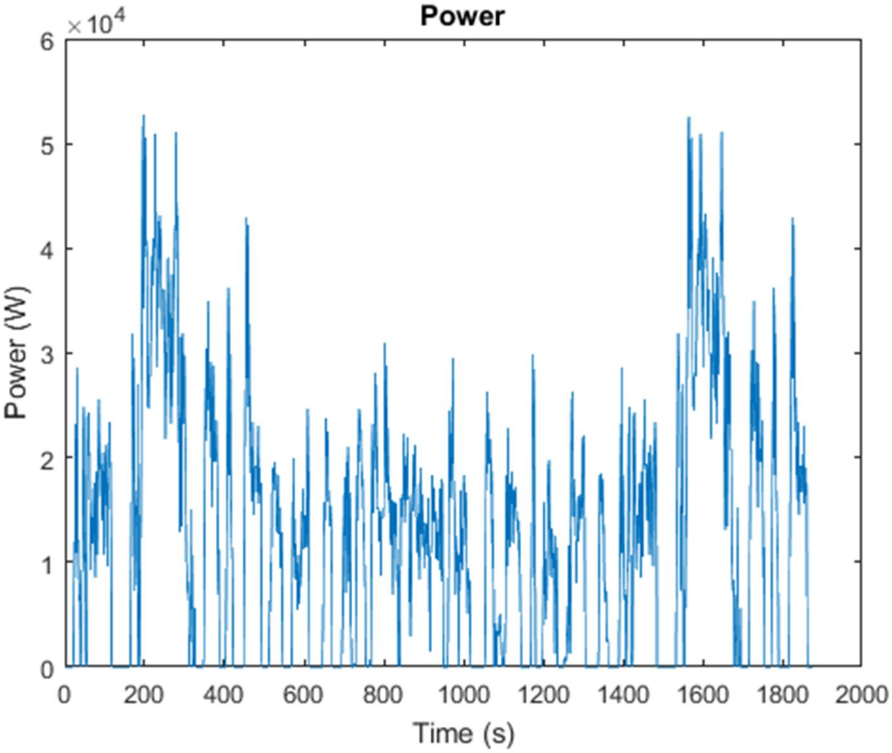

Fig. 7.7. UDDS output power obtained for 12/14 SPM.

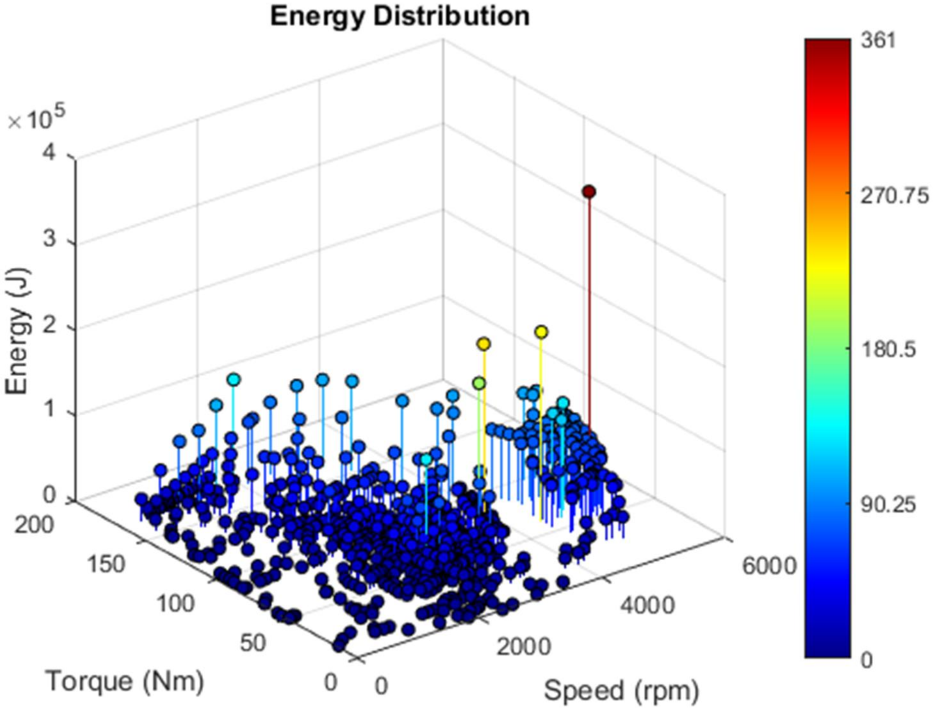

Fig. 7.8. UDDS energy distribution obtained for 12/14 SPM.

The resampling technique is applied to the dataset to ensure that each point has an equal magnitude of energy significance when being clustered. K-means clustering is applied to derive representative load points of the drive-cycle dataset. Gaussian mixture modelling is not used due to its increased computational burden in comparison to K-means clustering. Using the sum of squared error elbow method, six clusters prove to be sufficient for clustering the dataset. The clusters are visible in Fig. 7.9 and the location and energy significance of each centroid are listed in Table 7.3.

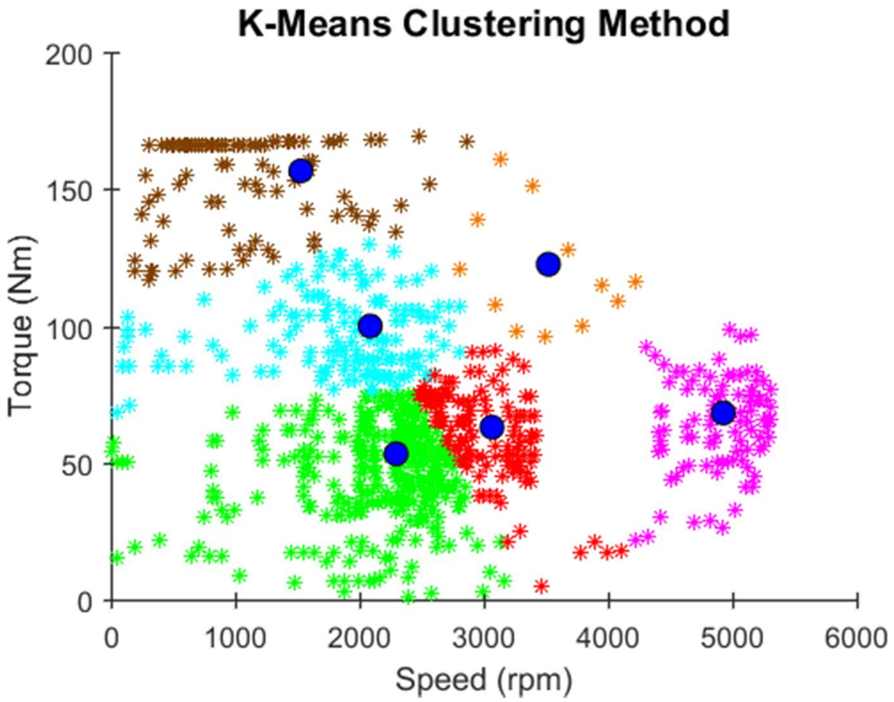

Fig. 7.9. K-means clustering result on the resampled dataset of the 12/14 SPM torque-speed load distribution.

TABLE 7.3

K-Means Clustering Result for Resampled Data

Speed (rpm)	Torque (Nm)	Normalized Energy (%)
1528.27	156.61	11.21%
2086.27	99.99	14.72%
2294.77	53.17	22.14%
3066.36	62.87	19.31%
3520.01	122.53	4.36%
4926.42	68.11	28.26%

7.2 Motor Current Selection and Inductance Parameter Determination

For an accurate inverter-motor system simulation, proper motor parameters need to be identified and modeled including all nonlinearities such as saturation of motor inductances. Further, *d*- and *q*-axis current excitations must be determined in order to get the desired output torque and speed from the machine to analyze at the desired representative load points. To perform this type of machine parameter determination, an efficiency map toolkit is used in the ANSYS FEA software. This toolkit incorporated MTPA and FW control strategies to select *d*- and *q*-axis current excitations and evaluate the machine at various load points across the torque-speed plane as seen in Fig. 7.10. During the loss FEA evaluation process, the toolkit derives the *d*- and *q*-axis inductances including all the accompanied nonlinear characteristics of saturation.

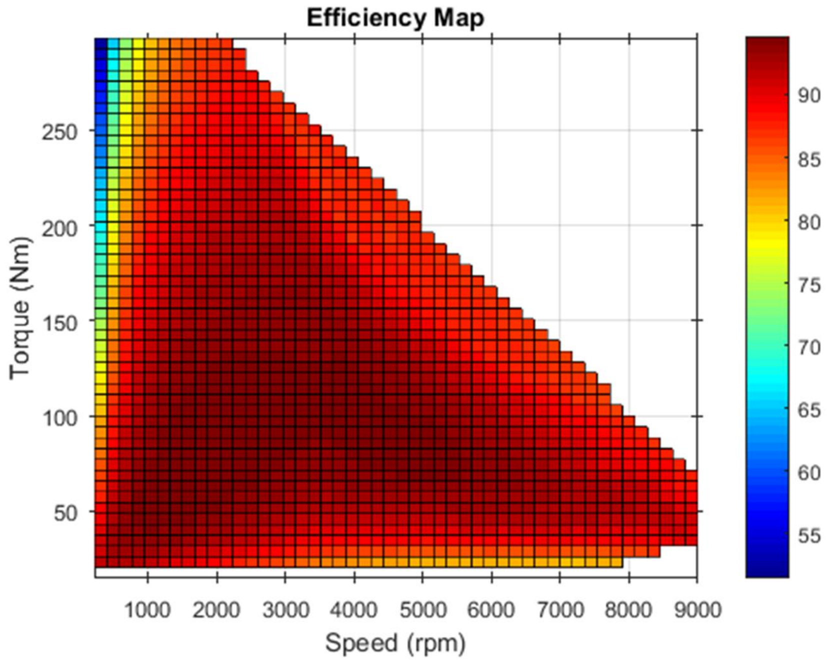

Fig. 7.10. Efficiency map of the 12/14 SPM.

Figures 7.11 and 7.12 display the variation of *d*- and *q*-axis current excitations across the torque speed plane. The results correspond to the theory of SPM control where I_q is proportional to the magnitude of torque production and $I_d = 0$ for all operating regions below the rated speed of 3000 rpm. The current excitation maps are created by curve-fitting the evenly distributed, discrete samples across the torque-speed plane that are evaluated by the toolkit. The maps are used as a lookup tables to determine the *d*- and *q*-

axis current excitations by using the speed and torque corresponding to each individual representative load point in the analysis.

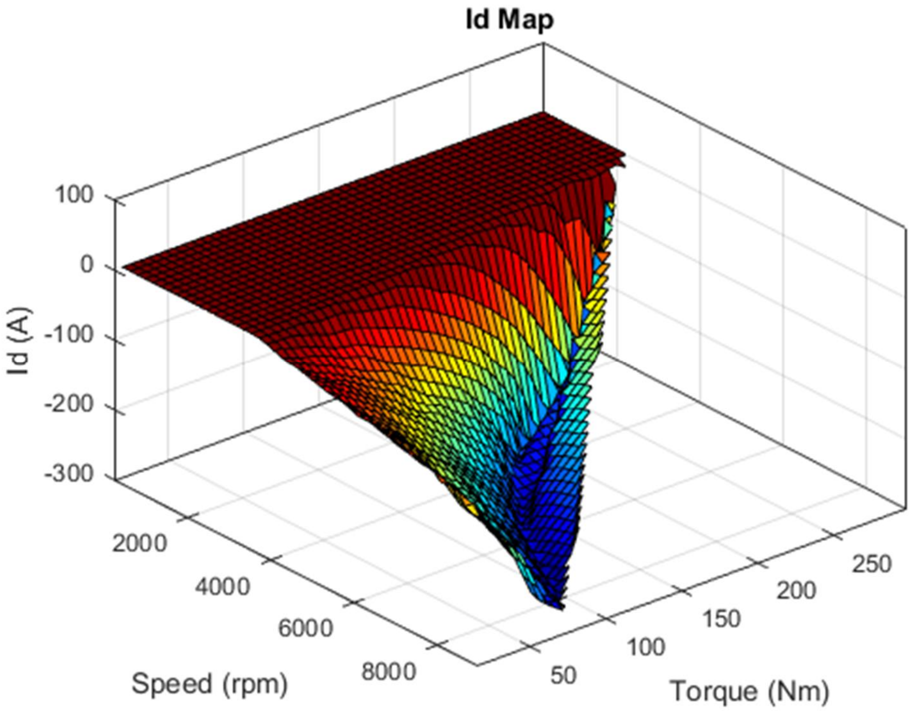

Fig. 7.11. Variation of I_d in the torque-speed plane.

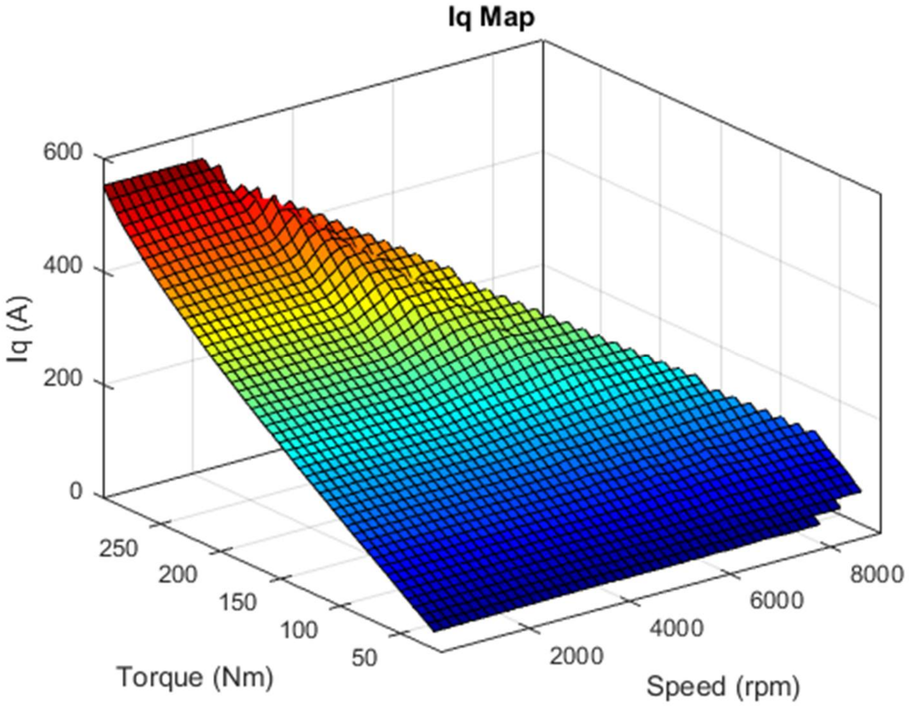

Fig. 7.12. Variation of I_q in the torque-speed plane.

Similarly, lookup tables are generated by curve fitting the *d*- and *q*-axis inductances across the torque-speed plane as seen in Figs. 7.13 and 7.14, respectively. Similarly, the corresponding values of inductance are determined for the individual clustered drive-cycle points. All motor determined motor parameters for the representative load points are summarized in Table 7.4.

TABLE 7.4

K-Means Clustering Result and Associated Motor Parameters

Cluster Point	1	2	3	4	5	6
Speed (rpm)	1,528.27	2,086.27	2,294.77	3,066.36	3,520.01	4,926.42
Torque (Nm)	156.61	99.99	53.17	62.87	122.53	68.11
Energy	11.21%	14.72%	22.14%	19.31%	4.36%	28.26%
I_d (A)	0	0	0	-0.61	-40.33	-92.94
I_q (A)	251.1	159.35	85.97	102.12	200.06	113.05
I_m (A)	251.1	159.35	85.97	102.12	204.09	146.35
Current Angle (deg)	0	0	0	0.34	11.4	39.42
L_d (uH)	207.85	207.87	207.62	207.73	212.48	218.29
L_q (uH)	196.1	192.86	189.77	190.37	195.41	192.36

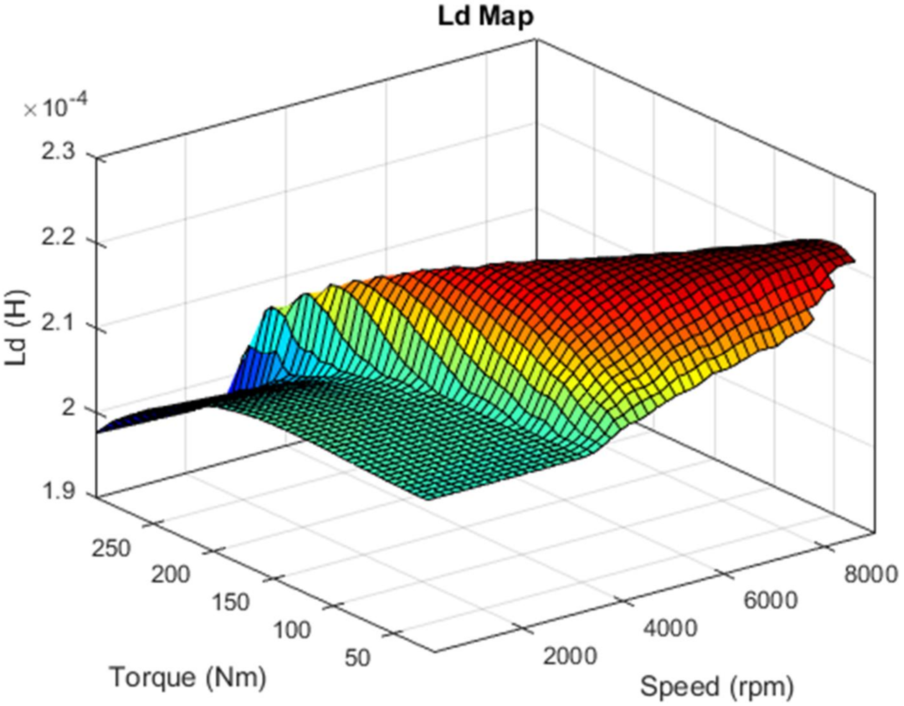

Fig. 7.13. Variation of L_d in the torque-speed plane.

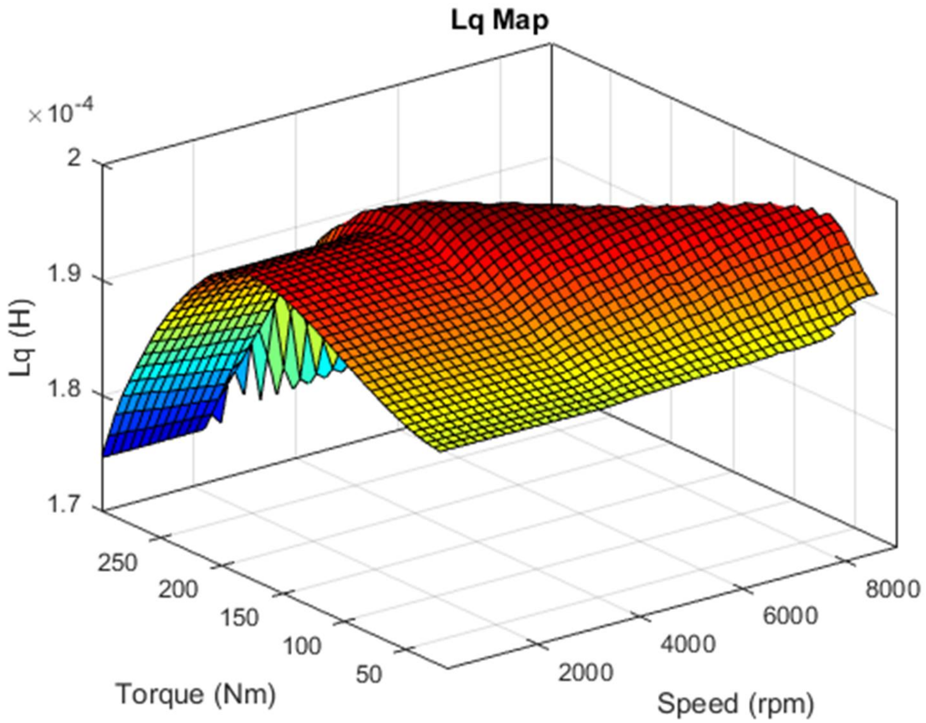

Fig. 7.14. Variation of L_q in the torque-speed plane.

7.3 PSIM Motor Drive Simulation

PSIM is an electronic circuit simulation software used mainly for modeling and analysis of power electronics and motor drive systems. It is employed to model the IGBT and GaN inverter to drive the parameterized motor model. The inverter device specifications used in the simulation are listed in Table 7.5. For the IGBT inverter, a two-level inverter module is used with a switching frequency of 10 kHz. For the GaN simulation, a two-level is constructed using individual switches. Twelve switches are used in parallel to match the power rating of the IGBT inverter.

The component overview of the simulation is displayed in Fig. 7.15. The simulation contains a current control loop to drive the inverter gate pulses through sine pulse width modulation (SPWM) and control the 12-14 SPM motor. The current control loop is necessary to obtain the proper magnitude of output current with PWM induced current ripple. The motor is connected to a dynamometer that maintains a constant speed and matches the torque output of the SPM that is generated from the applied current excitation.

TABLE 7.5

IGBT and GaN Specifications

	IGBT	**GaN**
Model Number	Infineon FS800R07A2E3	GaN Systems GS66516B
Voltage	650 V	650 V
ICE/IDS	800 A	720 A
RCE(on)/RDS(on)	630 mq	25 mq per switch
Bus Link Capacitor	1,000 εF	700 εF
Number of Parallel Devices	1	12 @ 60 A
Switching Frequency	10 kHz	30 kHz

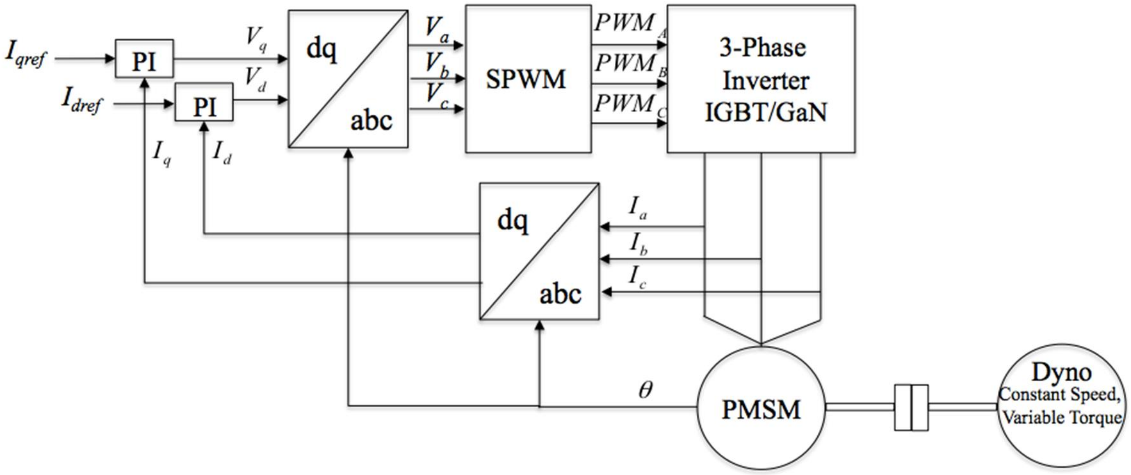

Fig. 7.15. Current control diagram for inverter-motor simulation.

Figures 7.16 and 7.17 show the PSIM simulation schematics developed for the system simulations that contain the current control loop, PWM generator, inverter, motor, and dynamometer.

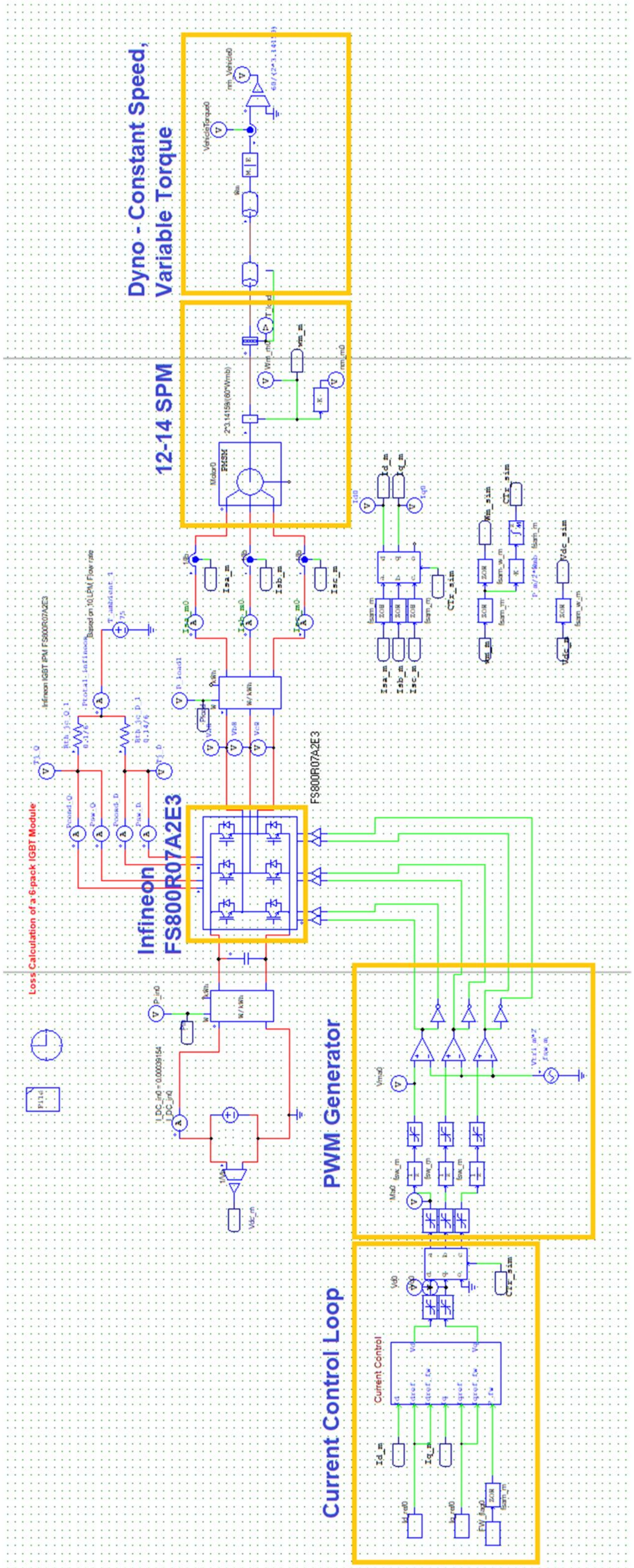

Fig. 7.16. PSIM schematic of two-level IGBT inverter.

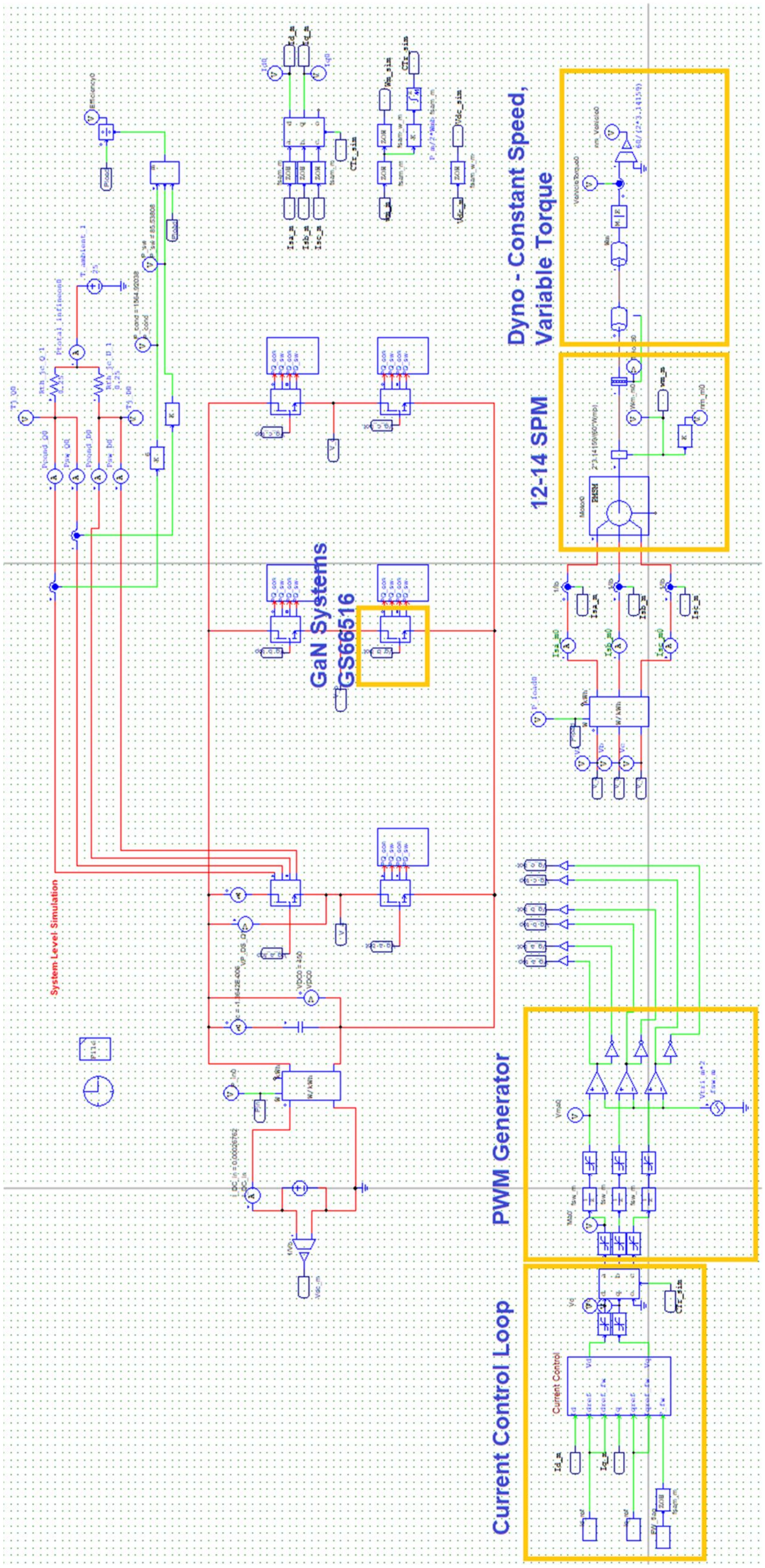

Fig. 7.17. PSIM schematic of two-level GaN inverter.

For each cluster point, the simulations are modified to the corresponding values of I_d, I_q, L_d, L_q, and the dynamometer speed as obtained in Table 7.4. In addition, the PI parameters of the control loop are dynamically updated, as in (7.1) ï (7.4), based on the value of d- and q-axis inductances to obtain better responses during the simulation of each representative load point [60].

$$P_d = \left(2\pi f_{sw} L_d\right)/10 \tag{7.1}$$

$$T_d = \left(10 L_d\right)/\left(2\pi f_{sw} R_s L_q\right) \tag{7.2}$$

$$P_q = \left(2\pi f_{sw} L_q\right)/10 \tag{7.3}$$

$$T_q = \left(10\right)/\left(2\pi f_{sw} R_s\right) \tag{7.4}$$

where f_{sw} is the switching frequency and R_s is the phase resistance. Figure 7.18 shows the PSIM result of the IGBT simulation for the first representative load point of the drive cycle. The figure shows that the current was properly controlled to the desired values of d- and q-axis excitations and that the motor is properly modeled since the output torque corresponds to the 156 Nm desired for the load condition. One period of the three phase current excitations is captured during the motorôs steady-state operation and exported as seen in Fig. 7.19. This current excitation contains all the inverter induced time harmonics that are injected into the machine while operating in this load condition. This time series of current excitation is imported into ANSYS to analyze the FEA derived effects of the time harmonics on the machine. This process is repeated for each of the representative load points and the entire procedure is also repeated for the GaN inverter and ideal sinusoidal excitations.

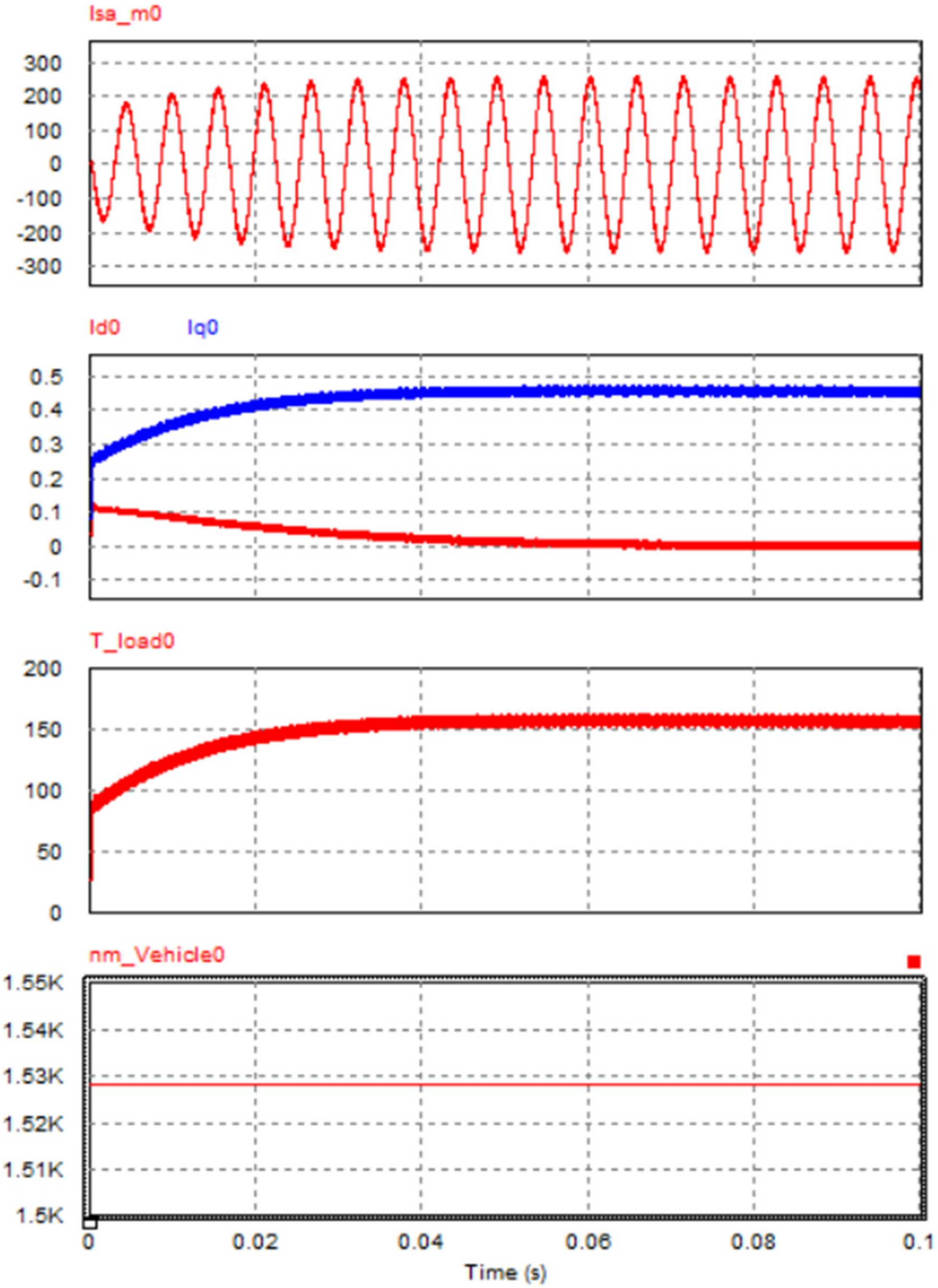

Fig. 7.18. PSIM results for the first cluster point of the IGBT simulation.

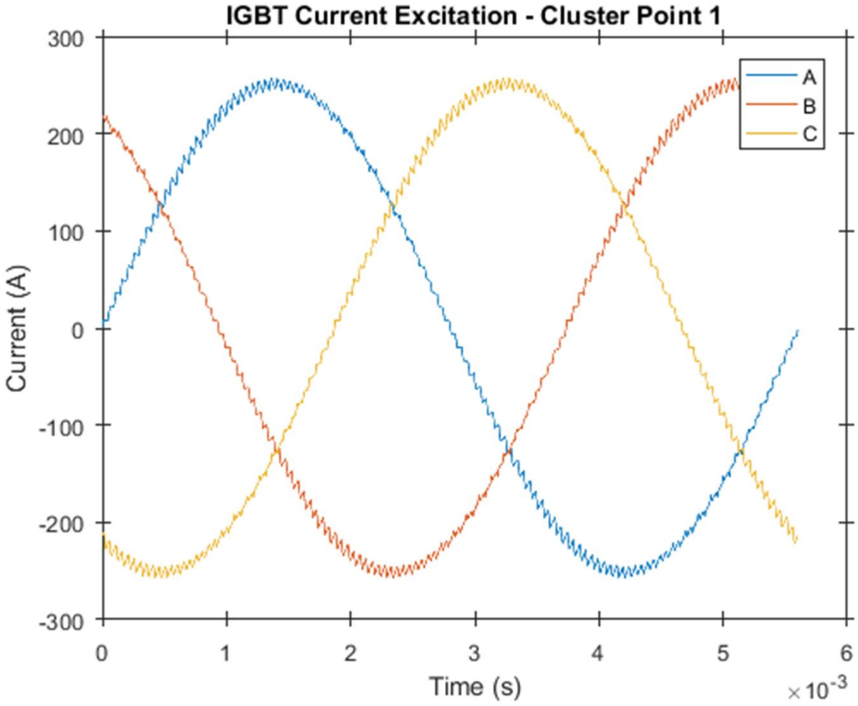

Fig. 7.19. Three-phase current excitation exported from PSIM.

7.4 FEA Motor Analysis of Time Harmonic Effects

Figure 7.20 displays the injected current excitations for each representative drive-cycle load condition, which were obtained from the PSIM simulations. It is evident from these plots that there is an increase in current ripple for all IGBT waveforms in comparison GaN. This has a direct effect on the torque ripple as indicated by the torque equationôs dependency on the instantaneous value current excitation as seen in (7.5) [38]. The variation of torque ripple in the motor for the three excitations at each load condition is shown in Fig. 7.21.

$$T_{em} = \frac{P}{2}\left(\begin{array}{l} i_a(\theta)\sum_{v=1}^{v_M} v\lambda_v \sin(v\theta+\phi_v) + i_b(\theta)\sum_{v=1}^{v_M} v\lambda_v \sin(v\theta+\phi_v-120°)+ \\ i_c(\theta)\sum_{v=1}^{v_M} v\lambda_v \sin(v\theta+\phi_v-240°) \end{array} \right) \tag{7.5}$$

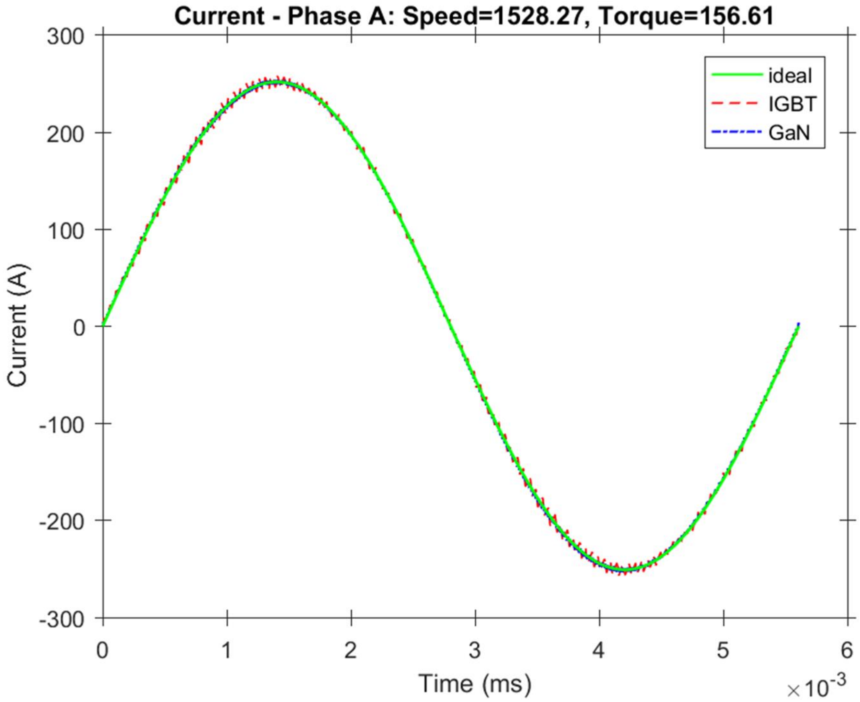

Fig. 7.20. Current excitation comparison for the first cluster point of ideal, IGBT, and GaN simulations.

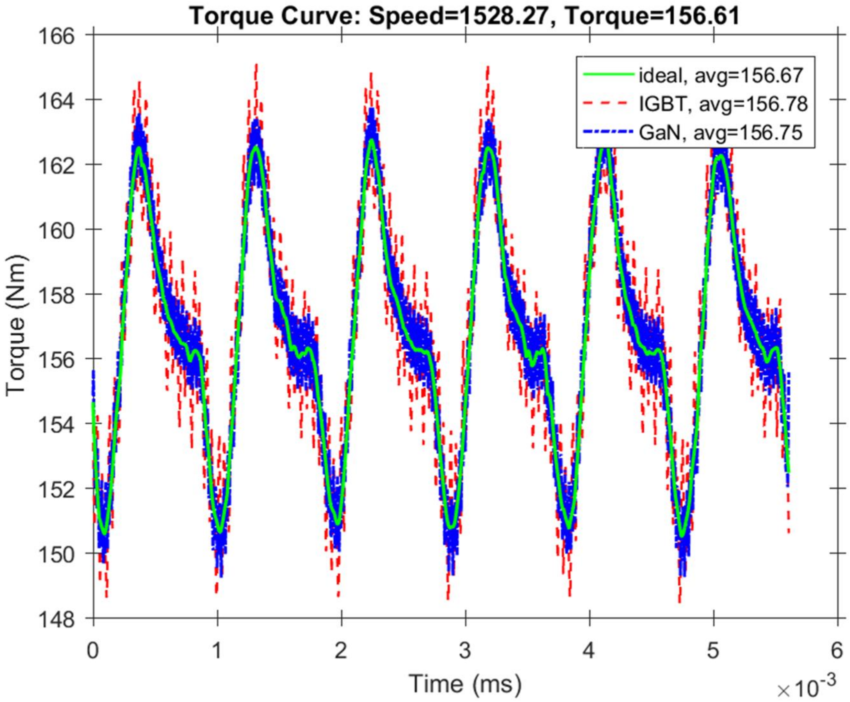

Fig. 7.21. Torque comparison for the first cluster point of ideal, IGBT, and GaN simulations.

Table 7.6 summarizes the substantial increase of torque ripple at each cluster point for IGBT and GaN with respect to a pure sinusoidal excitation. However, there is a significant reduction of torque ripple when comparing the GaN inverter with respect to IGBT.

TABLE 7.6
IGBT and GaN Torque Ripple Comparison

Cluster Point	**Speed (rpm)**	**Avg. Torque (Nm)**	**Torque Ripple (%)**				
			Ideal	**IGBT**	**% Rise IGBT from Ideal**	**GaN**	**% Rise GaN from Ideal**
1	1,528.27	156.61	7.82	10.63	35.93%	9.3	18.93%
2	2,086.27	99.99	9.91	16.16	63.07%	12.08	21.90%
3	2,294.77	53.17	15.27	23.32	52.72%	17.97	17.68%
4	3,066.36	62.87	13.61	22.24	63.41%	17.26	26.82%
5	3,520.01	122.53	9.28	15.21	63.90%	11.84	27.59%
6	4,926.42	68.11	12.94	25.36	95.98%	17.9	38.33%

The stranded (copper), core, and solid (magnet) losses for the first load condition obtained from the FEA simulation is displayed in Figs. 7.22 ï 7.24. The stranded loss is essentially the same for each load condition since the magnitude of current is equal in each case. However, the ferromagnetic core and magnets in the machine experience a harmonic loss component. Therefore, when more harmonics are present as in the IGBT excitation, there is a significant increase in core and magnet losses.

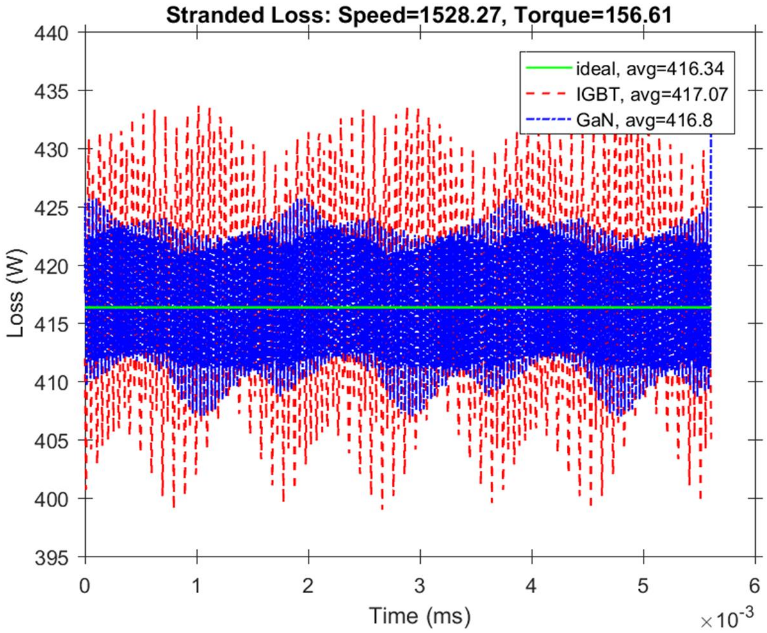

Fig. 7.22. Stranded loss comparison for the first cluster point of ideal, IGBT, and GaN simulations.

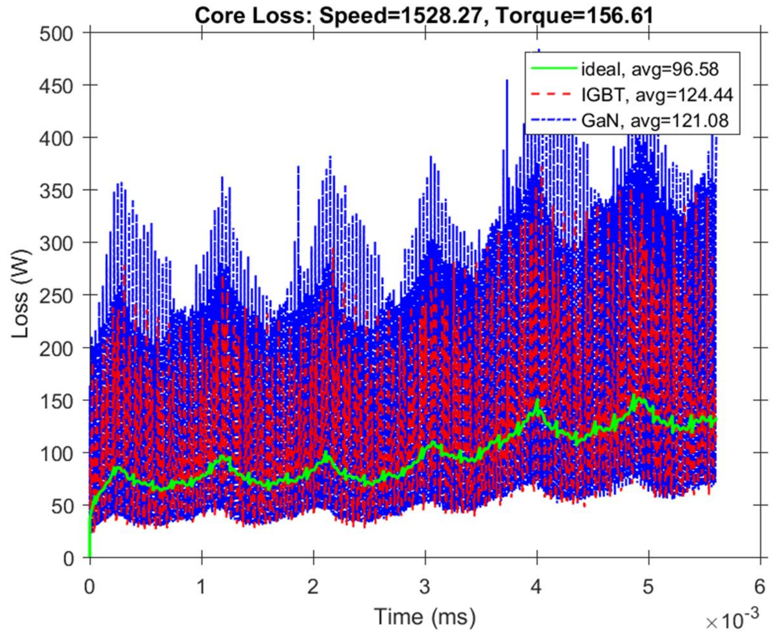

Fig. 7.23. Core loss comparison for the first cluster point of ideal, IGBT, and GaN simulations.

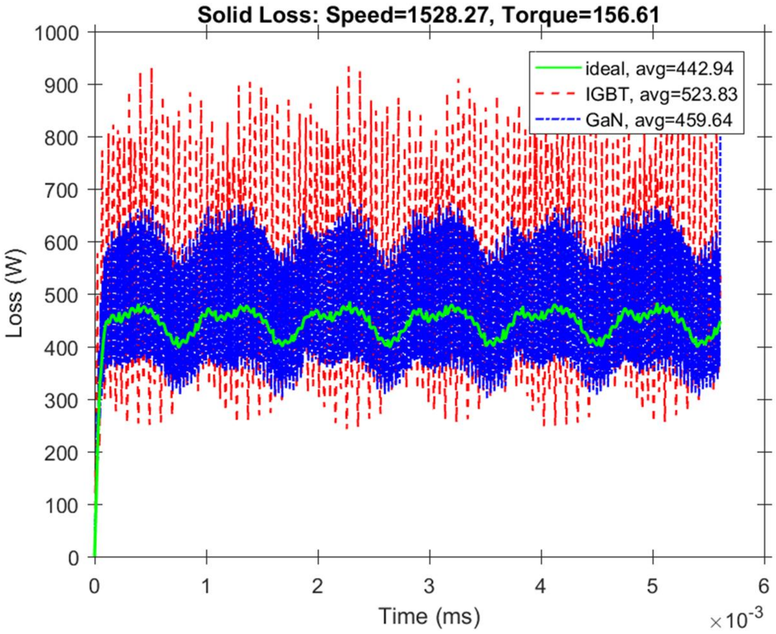

Fig. 7.24. Solid loss comparison for the first cluster point of ideal, IGBT, and GaN simulations.

Tables 7.7 ï 7.9 summarize the percentage increase of the three losses for IGBT and GaN with respect to a pure sinusoidal excitation. There is an evident decrease in loss for GaN driven motors in terms of core loss and a substantial decrease in solid or magnet losses.

TABLE 7.7

IGBT and GaN Stranded Loss Comparison

Cluster Point	Speed (rpm)	Avg. Torque (Nm)	Stranded Loss (W)				
			Ideal	IGBT	% Rise IGBT from Ideal	GaN	% Rise GaN from Ideal
1	1,528.27	156.61	416.34	417.07	0.18%	416.8	0.11%
2	2,086.27	99.99	167.67	167.95	0.17%	167.54	-0.08%
3	2,294.77	53.17	48.8	49.37	1.17%	48.83	0.06%
4	3,066.36	62.87	68.87	67.48	-2.02%	69.17	0.44%
5	3,520.01	122.53	275.02	273.28	-0.63%	275.25	0.08%
6	4,926.42	68.11	141.43	135.41	-4.26%	141.86	0.30%

TABLE 7.8

IGBT and GaN Core Loss Comparison

Cluster Point	Speed (rpm)	Avg. Torque (Nm)	Core Loss (W)				
			Ideal	IGBT	% Rise IGBT from Ideal	GaN	% Rise GaN from Ideal
1	1,528.27	156.61	96.58	124.44	28.85%	121.08	25.37%
2	2,086.27	99.99	141.74	169.58	19.64%	163.5	15.35%
3	2,294.77	53.17	157.48	188.08	19.43%	179.5	13.98%
4	3,066.36	62.87	253.99	285.29	12.32%	278.92	9.82%
5	3,520.01	122.53	310.81	373.12	20.05%	340.07	9.41%
6	4,926.42	68.11	420.46	483.14	14.91%	445.85	6.04%

TABLE 7.9

IGBT and GaN Solid Loss Comparison

Cluster Point	Speed (rpm)	Avg. Torque (Nm)	Solid Loss (W)				
			Ideal	IGBT	% Rise IGBT from Ideal	GaN	% Rise GaN from Ideal
1	1,528.27	156.61	442.94	523.83	18.26%	459.64	3.77%
2	2,086.27	99.99	510.52	595.04	16.56%	532.72	4.35%
3	2,294.77	53.17	447.08	550.64	23.16%	468.72	4.84%
4	3,066.36	62.87	838.96	931.27	11.00%	865.9	3.21%
5	3,520.01	122.53	1502.96	1720.35	14.46%	1548.01	3.00%
6	4,926.42	68.11	1127.6	1314.06	16.54%	1143.81	1.44%

Table 7.10 shows the total loss experienced by the motor for the three types of excitation. Using (7.6) ï (7.8) the efficiency of the motor at each representative drive-cycle point is determined.

$$P_{out} = T\omega \tag{7.6}$$

$$P_{in} = T\omega + P_{Cu} + P_{Fe} + P_{mech} \tag{7.7}$$

$$\eta = \frac{P_{out}}{P_{in}} \tag{7.8}$$

Finally, a weighted efficiency is calculated to determine the overall drive-cycle energy efficiency of the motor using (7.9). The results are summarized in Table 7.11.

$$\eta_w = \sum_i \frac{T_i \omega_i}{P_{in,i}} E_i \tag{7.9}$$

TABLE 7.10

IGBT and GaN Total Loss and Efficiency Comparison

Cluster Point	**Speed (rpm)**	**Avg. Torque (Nm)**	**Total Loss (W)**			**Efficiency (%)**		
			Ideal	**IGBT**	**GaN**	**Ideal**	**IGBT**	**GaN**
1	1,528.27	156.61	955.86	1,065.34	997.52	96.33	95.92	96.17
2	2,086.27	99.99	819.93	932.57	863.76	96.38	95.91	96.20
3	2,294.77	53.17	653.36	788.09	697.05	95.14	94.19	94.83
4	3,066.36	62.87	1,161.82	1,284.04	1,213.99	94.56	94.02	94.33
5	3,520.01	122.53	2,088.79	2,366.75	2,163.33	95.58	95.02	95.43
6	4,926.42	68.11	1,689.49	1,932.61	1,731.52	95.41	94.79	95.30

TABLE 7.11

IGBT and GaN Weighted Efficiency and UDDS Drive-Cycle Motor Energy Efficiency Comparison

Cluster Point	Speed (rpm)	Avg. Torque (Nm)	Energy Significance (%)	Weighted Efficiency (%)		
				Ideal	IGBT	GaN
1	1,528.27	156.61	11.21%	10.80%	10.75%	10.78%
2	2,086.27	99.99	14.72%	14.19%	14.12%	14.16%
3	2,294.77	53.17	22.14%	21.06%	20.85%	20.99%
4	3,066.36	62.87	19.31%	18.26%	18.16%	18.21%
5	3,520.01	122.53	4.36%	4.17%	4.14%	4.16%
6	4,926.42	68.11	28.26%	26.96%	26.79%	26.93%
Motor Energy Efficiency for UDDS Drive-Cycle:				**95.44%**	**94.81%**	**95.24%**

7.5 Conclusions

The overall analysis concludes that the motor energy efficiency when executing the UDDS drive-cycle will increase from 94.81% to 95.24% when replacing an IGBT inverter with a GaN inverter. The motor will also experience an average of 22.44% reduction in torque ripple across the various drive-cycle points in comparison to IGBT. There is a 5.68% reduction in core loss and an 11.49% reduction in solid losses for GaN inverters. This significantly improves efficiency at high speeds and low torque regions where core and magnet losses are dominant. In addition, the increased efficiency reduces the magnitude of heat production in the rotor of the machine where cooling is difficult to implement. Further improvement of overall system efficiency is tangible with GaN based inverters because of their higher inverter efficiencies due to low switching and conduction loss. This study's focus is on motor performance, therefore inverter efficiency is not considered in this analysis.

CHAPTER 8

Conclusions

This thesis proposed a vehicle dynamics model in chapter 2 to derive the motor output torque, speed, power, and energy to analyze the various load conditions the electric motor experiences during a drive-cycle. For computational efficiency when performing drive-cycle analysis, K-means clustering and Gaussian mixture modeling algorithms are implemented in chapter 3 to reduce the large amount of load points to a minimal number of representative points. These cluster points represent the cycle with a few torque-speed points that focus on areas with high energy consumption that are most significant for performance evaluation.

Chapter 4 introduces an enhanced finite element analysis technique to evaluate the machine performance across the clustered drive-cycle points in a computationally efficient manner. Employing FEA provides higher accuracy of machine evaluation by considering non-linear material properties such as saturation. Chapter 5 summarizes a procedure to create a lumped parameter thermal network of an electric machine and calculate steady-state temperatures for different operating conditions using the losses determined in the machine evaluation process. The evaluation procedure in chapter 4 and the thermal model in chapter 5 are implemented into a multi-objective differential evolution optimization algorithm in chapter 6. The baseline direct-drive machine geometry is optimized for drive-cycle energy efficiency, torque ripple, weight, cost, and average winding temperature. The optimization results show the trade-off between the various objectives and proved that the GMM clustering technique was superior for obtaining a machine with the highest drive-cycle energy efficiency.

Finally, the vehicle loading analysis in chapter 1 and the K-means clustering technique in chapter 2 are implemented into an inverter-motor simulation to analyze the effects of inverter generated time harmonics on motor performance. The study showed that the high-frequency operation of GaN is beneficial for reducing torque ripple and harmonic losses present in the core and magnets of the machine. The analysis quantified the increase of drive-cycle motor energy efficiency of GaN in comparison to the commonly used IGBT.

8.1 Future Work

Suggested future work includes:

1. Constructing a more comprehensive vehicle dynamics model that includes tire slip and other effects present in real driving conditions.
2. Considering regenerative capabilities in the evaluation procedure. This requires analysis of the power electronics and batteryôs capability of capturing the storing the instantaneous power generated during deceleration.
3. Considering inverter time harmonics and incorporating a harmonic loss model into the machine optimization procedure.
4. Derive thermal time constants to model and compare the transient behavior of the motor temperature.
5. Apply the machine optimization procedure to custom applications such as transport trucks or vehicles in high-traffic regions that consider various types of drive-cycles.
6. Performing drive-cycle analysis on various slot-pole combinations and rotor topologies.
7. Considering the effects of different gear ratios on drive-cycle efficiency and design a machine to locate the high efficiency regions below rated speed near areas of high-energy consumption for maximized drive-cycle energy efficiency.

REFERENCES/BIBLIOGRAPHY

[1] "Canada: Light-duty: Fuel Consumption and GHG | Transport Policy", *Transportpolicy.net*, 2018. [Online]. Available: https://www.transportpolicy.net/standard/canada-light-duty-fuel-consumption-and-ghg/. [Accessed: June 4, 2018].

[2] ñHow Automakers Will Meet 2016 CAFE Standardsò, 2018. [Online]. Available: https://www.caranddriver.com/features/how-automakers-will-meet-2016-cafe-standards. [Accessed: June 4, 2018].

[3] T. Finken, M. Felden and K. Hameyer, "Comparison and design of different electrical machine types regarding their applicability in hybrid electrical vehicles," *2008 18th International Conference on Electrical Machines*, Vilamoura, 2008, pp. 1-5.

[4] T. Finken, M. Hombitzer and K. Hameyer, "Study and comparison of several permanent-magnet excited rotor types regarding their applicability in electric vehicles," *2010 Emobility - Electrical Power Train*, Leipzig, 2010, pp. 1-7.

[5] M. Ehsani, Y. Gao, and A. Emadi, ñ*Modern Electric, Hybrid Electric and Fuel Cell Vehicles*ò CRC Press, 2010.

[6] S. J. Chapman, *Electric Machinery Fundamentals*, 4th Edition, McGraw ïHill Copyright 2005.

[7] S. Morimoto, Y. Takeda, T. Hirasa and K. Taniguchi, "Expansion of operating limits for permanent magnet motor by current vector control considering inverter capacity," *IEEE Transactions on Industry Applications*, vol. 26, no. 5, pp. 866-871, Sept.-Oct. 1990.

[8] Dongyun Lu and N. C. Kar, "A review of flux-weakening control in permanent magnet synchronous machines," *2010 IEEE Vehicle Power and Propulsion Conference*, Lille, 2010, pp. 1-6.

[9] N. Bianchi and A. Canova, "FEM analysis and optimisation design of an IPM synchronous motor," *2002 International Conference on Power Electronics, Machines and Drives (Conf. Publ. No. 487)*, Sante Fe, NM, USA, 2002, pp. 49-54.

[10] Q. Li, T. Fan, X. Wen, Y. Li, Z. Wang and J. Guo, "Design optimization of interior permanent magnet sychronous machines for traction application over a given driving cycle," *IECON 2017 - 43rd Annual Conference of the IEEE Industrial Electronics Society*, Beijing, 2017, pp. 1900-1904.

[11] K. Fujisaki, M. Sakai and S. Takeda, "Motor loss increment of induction motor driven by PWM inverter in comparison with inverter circuit loss," *2012 15th International Conference on Electrical Machines and Systems (ICEMS)*, Sapporo, 2012, pp. 1-6.

[12] M. Ehsani, Y. Gao, and A. Emadi, *Modern Electric, Hybrid Electric, and Fuel Cell Vehicles*, CRC Press, USA, 2010, pp. 30-51, 105-108.

[13] M. G. Carignano, J. M. Cabello and S. Junco, "Sizing and performance analysis of battery pack in electric vehicles," *2014 IEEE Biennial Congress of Argentina (ARGENCON)*, Bariloche, 2014, pp. 240-244.

[14] The US Environmental Protection Agency Website. [Online]. Available: https://www.epa.gov/vehicle-and-fuel-emissions-testing/dynamometerdriveschedules#Economic. [Accessed: June 7, 2018]

[15] Car Engineer Website. [Online]. Available: http://www.car-engineer.com/the-different-driving-cycles/. [Accessed: June 7, 2018]

[16] Ford Fiesta 2014 Specifications. [Online]. Available: https://media.ford.com. [Accessed: June 14, 2018]

[17] BorgWarner Drivetrain Systems, 2018. [Online]. Available: http://www.evwest.com/support/borgwarneredrive.pdf. [Accessed: June 14, 2018]

[18] ñElectric traction ï Rotating electrical machines for rail and road vehicles - Part4,ò IEC Standard, IEC 60349-4, pp. 28, 2012.

[19] T. M. Jahns, ñThe expanding role of PM machines in direct-drive applications,ò *IEEE Inter. Conf. on Elec. Mach. and Sys*., 2011.

[20] Y. Li, X. Lu, and N. C. Kar, ñRule-based control strategy with novel parameters optimization using nsga-ii for power-split phev operation cost minimization,ò *IEEE Transaction on Vehicular Technology*, vol. 63, pp. 3051-3061, 2014.

[21] P. Lazari, J. Wang, and L. Chen, "A computationally efficient design technique for electric-vehicle traction machines," *IEEE Transactions on Industry Applications*, vol. 50, no. 5, pp. 3203-3213, Sept.-Oct. 2014.

[22] A. Fatemi, N. A. O. Demerdash, D. M. Ionel, and T. W. Nehl, "Large-scale electromagnetic design optimization of PM machines over a target operating cycle," *IEEE Energy Conversion Congress and Exposition*, Montreal, QC, 2015, pp. 4383-4390.

[23] Error Sum of Squares (SSE). [Online]. Available: https://hlab.stanford.edu/brian/error_sum_of_squares.html. [Accessed: June 17 2018]

[24] P. Lazari, J. Wang, and L. Chen, "A computationally efficient design technique for electric-vehicle traction machines," *IEEE Transactions on Industry Applications*, vol. 50, no. 5, pp. 3203-3213, Sept.-Oct. 2014.

[25] L. Chen, X. Chen, J. Wang, and P. Lazari, "A computationally efficient multi-physics optimization technique for permanent magnet machines in electric vehicle traction applications," *IEEE International Electric Machines & Drives Conference*, Coeur d'Alene, ID, 2015, pp. 1644-1650.

[26] E. Carraro, M. Morandin, and N. Bianchi, "Optimization of a traction PMASR motor according to a given driving cycle," *IEEE Transportation Electrification Conference and Expo*, Dearborn, MI, 2014, pp. 1-6.

[27] "Gaussian Mixture Model | Brilliant Math & Science Wiki", *Brilliant.org*, 2018. [Online]. Available: https://brilliant.org/wiki/gaussian-mixture-model/. [Accessed: July 16 2018]

[28] J. A. Bilmes, *A Gentle Tutorial of the EM Algorithm and its Application to Parameter Estimation for Gaussian Mixture and Hidden Markov Models*. Berkeley CA: 1998.

[29] M. A. T. Figueiredo, J. M. N. Leitao1, and A. K. Jain, ñOn fitting mixture modelsò, *Energy Minimization Methods in Computer Vision and Pattern Recognition*, E. Hancock and M. Pellilo (Eds.), pp. 54-69, Springer-Verlag, 1999.

[30] D. M. Ionel and M. Popescu, ñFinite element surrogate model for electric machines with revolving field application to IPM motors,ò 2009 *IEEE Energy Conversion Congress and Exposition*, San Jose, CA, 2009, pp. 178-186.

[31] N. Demerdash and T. Nehl, ñFlexibility and economics of implementation of the finite element and difference techniques in nonlinear magnetic fields of power devices," *IEEE Transactions on Magnetics*, vol. 12, no. 6, pp. 1036-1038, 1976.

[32] N. A. Demerdash, T. W. Nehl, ñAn evaluation of the methods of finite elements and finite differences in the solution of nonlinear electromagnetic fields in electrical machines," *IEEE Transactions on Power Apparatus and Systems*, vol. PAS-98, no. 1, pp. 74-87, 1979.

[33] K. L. V. Iyer, H. Dhulipati, S. Mukundan, K. Mukherjee, J. Tjong and N. C. Kar, "Design approach incorporating MTPA and winding function theories for on-board direct-drive surface PM machines with concentrated windings in EVs," *2016 XXII International Conference on Electrical Machines (ICEM)*, Lausanne, 2016, pp. 1499-1505.

[34] H. Dhulipati, K. L. V. Iyer, S. Mukundan, K. Mukherjee, J. Tjong, and N. C. Kar, "Investigation of 6-phase surface PM machines with concentrated windings for reduction in space harmonics, leakage inductance and magnet loss in direct-drive EV," *XXII International Conference on Electrical Machines (ICEM)*, Lausanne, 2016, pp. 811-817.

[35] K. L. V. Iyer, S. Mukundan, H. Dhulipati, K. Mukherjee, B. Minaker and N. C. Kar, "Design considerations for permanent magnet machine drives for direct-drive electric vehicles," *2015 IEEE International Electric Machines & Drives Conference (IEMDC)*, Coeur d'Alene, ID, 2015, pp. 1170-1176.

[36] W. Fei and P. Luk, ñA new technique of cogging torque suppression in direct-drive permanent-magnet brushless machines,ò *IEEE Transactions on Industrial Applications*, vol. 46, pp. 1332-1340, 2010.

[37] W. Fei and P. Luk, ñTorque ripple reduction of a direct-drive permanent-magnet synchronous machine by material-efficient axial pole pairing,ò *IEEE Transactions on Industrial Electronics*, vol. 59, pp. 2601-2611, 2012.

[38] G. Y. Sizov, D. M. Ionel, and N. A. O. Demerdash, ñModeling and parametric design of permanent-magnet ac machines using computationally efficient finite-element analysis,ò *IEEE Transactions on Industrial Electronics*, vol. 59, no. 6, pp. 2403-2413, June 2012.

[39] P. Zhang et al., ñMulti-objective tradeoffs in the design optimization of a brushless permanent magnet machine with fractional-slot concentrated windings,ò *2013 IEEE Energy Conversion Congress and Exposition*, Denver, CO, 2013, pp. 2842-2849.

[40] L. Chen, J. Wang, P. Lazari, and Xiao Chen, ñOptimizations of a permanent magnet machine targeting different driving cycles for electric vehicles,ò *2013 International Electric Machines & Drives Conference*, Chicago, IL, 2013, pp. 855-862.

[41] K. Ellsworth, "Temperature Coefficient of Copper", *Cirris.com*, 2018. [Online]. Available: https://www.cirris.com/learning-center/general-testing/special-topics/177-temperature-coefficient-of-copper. [Accessed: July 22 2018]

[42] C. Kim, M. Koo, J. Kim, J. Ahn, K. Hong and J. Choi, "Core loss analysis of permanent magnet synchronous generator with slotless stator," *IEEE Transactions on Applied Superconductivity*, vol. 28, no. 3, pp. 1-4, April 2018

[43] M. Sarma, *Electric Machines: Steady-State Theory and Dynamic Performance*. West Publishing Company, 1994.

[44] "Properties of NdFeB Magnets", *Magnetsales.com*, 2018. [Online]. Available: http://www.magnetsales.com/neo/neoprops.htm. [Accessed: July 26 2018]

[45] ñDensity of Copperò, 2018. [Online]. Available: https://www.amesweb.info/Materials/Density_of_Copper.aspx. [Accessed: July 26 2018]

[46] "Non-oriented Electrical Steels", *Aksteel.com*, 2018. [Online]. Available: https://www.aksteel.com/our-products/electrical-steel/non-oriented-electrical-steels. [Accessed: July 26 2018]

[47] E. L. Brancato, "Estimation of lifetime expectancies of motors," in *IEEE Electrical Insulation Magazine*, vol. 8, no. 3, pp. 5-13, May-June 1992.

[48] "Conduction, Convection, and Radiation - 3 Modes of Heat Transfer", *ScienceStruck*, 2018. [Online]. Available: https://sciencestruck.com/3modes-of-heat-transfer-conduction-convection-radiation. [Accessed: July 19, 2018].

[49] G. Sooriyakumar, R. Perryman and S. J. Dodds, "Analytical thermal modelling for permanent magnet synchronous motors," *2007 42nd International Universities Power Engineering Conference*, Brighton, 2007, pp. 192-196.

[50] T. Bäuml, C. Jungreuthmayer and C. Kral, "An innovative parametrization method for a thermal equivalent circuit model of an interior permanent magnet synchronous machine," *IECON 2011 - 37th Annual Conference of the IEEE Industrial Electronics Society*, Melbourne, VIC, 2011, pp. 1746-1751.

[51] M. J. Pieterse, ñDevelopment of a thermal model for an inner stator type reluctance motor,ò M. S. thesis, University of Waterloo, 2009.

[52] A. Qing, *Differential Evolution: Fundamentals and Applications in Electrical Engineering*. John Wiley & Sons, 2009, pp. 62-64.

[53] S. Minami, M. Sanada, S. Morimoto and Y. Inoue, "Influence of ratio of external diameter to stack length on torque and efficiency in outer rotor SPMSMs," *2015 IEEE Energy Conversion Congress and Exposition (ECCE)*, Montreal, QC, 2015, pp. 1834-1839.

[54] D. Wu and Z. Q. Zhu, "Design tradeoff between cogging torque and torque ripple in fractional slot surface-mounted permanent magnet machines," *IEEE Transactions on Magnetics*, vol. 51, no. 11, pp. 1-4, Nov. 2015

[55] K. Chen, S. Ji and L. Zhang, "Two-level three-phase voltage source inverter fed low-power AC induction motor based on unipolar pulse-width modulation method," in *IET Power Electronics*, vol. 9, no. 3, pp. 435-440, 9 3 2016.

[56] H. Järvisalo, J. Korhonen, J. Honkanen and P. Silventoinen, "Considerations for a high-speed PMSM drive featuring a GaN-ANPC inverter," *2017 19th European Conference on Power Electronics and Applications (EPE'17 ECCE Europe)*, Warsaw, 2017, pp. P.1-P.6.

[57] K. Kumar, "Efficiency improvement of three phase traction inverter through GaN devices for PMSM," *2016 IEEE International Conference on Power Electronics, Drives and Energy Systems (PEDES)*, Trivandrum, 2016, pp. 1-6.

[58] K. Kumar and S. B. Santra, "Performance analysis of three phase propulsion inverter for evs using gan semiconductor devices," *IEEE Transactions on Industry Applications*.

[59] C. Zhang, W. Zhu and Dong Yugang, "Loss analysis of rotor magnet with PWM controller switching frequency variation," *2014 IEEE Conference and Expo Transportation Electrification Asia-Pacific (ITEC Asia-Pacific)*, Beijing, 2014, pp. 1-8.

[60] A. A. S. Ahmad, M. S. Zainal, L. N. Ismail, W. S. Saidon, and A. Idzwan Tajudin, ñCurrent PI-gain determination for permanent magnet synchronous motor by using particle swarm optimization,ò *2017 Indonesian Journal of Electrical Engineering and Computer Science*, vol. 6. no. 2, pp. 412-421.

APPENDICES

Appendix A
Permission for using IEEE Publications

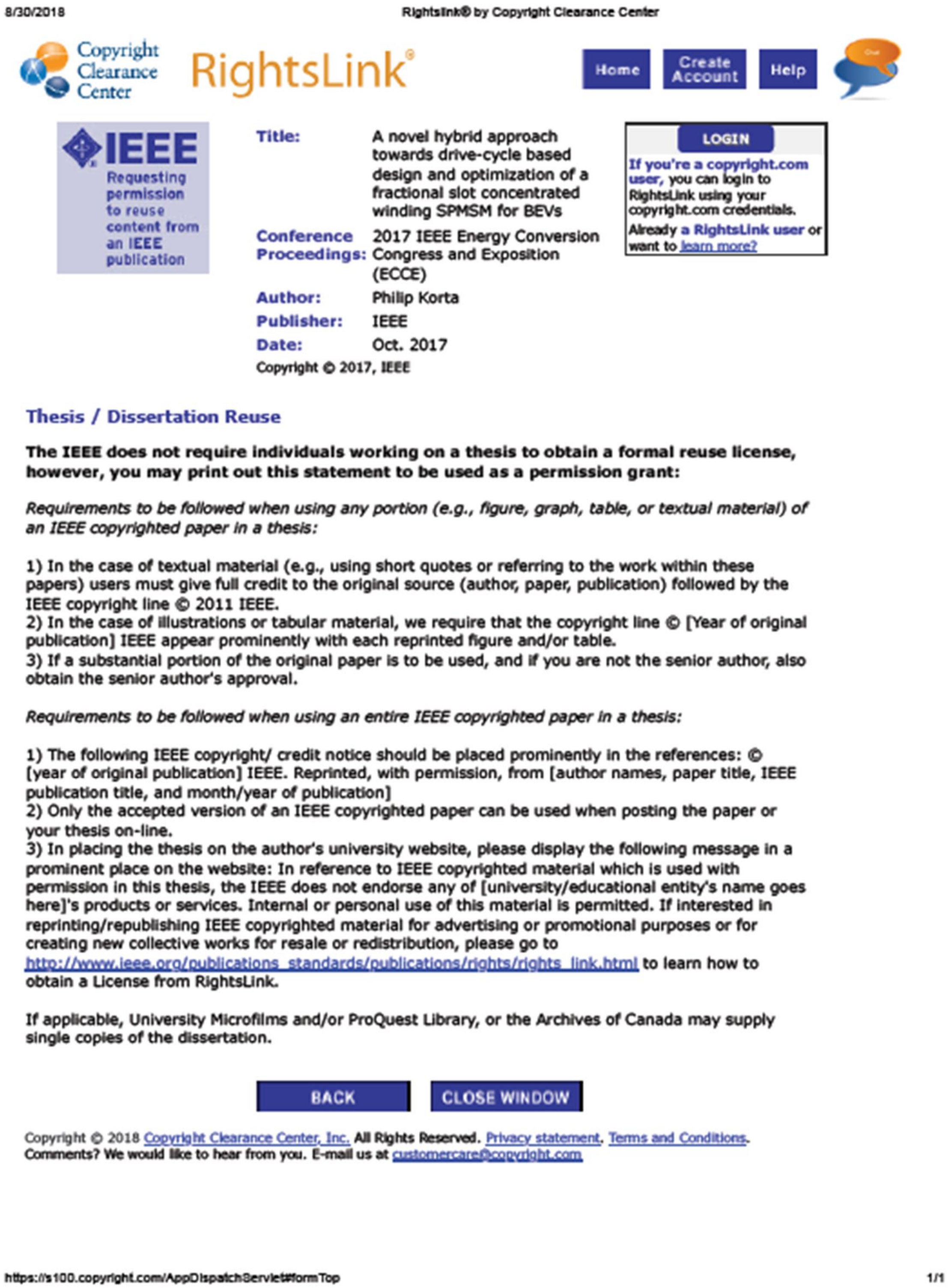

8/30/2018 Rightslink® by Copyright Clearance Center

IEEE Requesting permission to reuse content from an IEEE publication

Title: A novel hybrid approach towards drive-cycle based design and optimization of a fractional slot concentrated winding SPMSM for BEVs

Conference Proceedings: 2017 IEEE Energy Conversion Congress and Exposition (ECCE)

Author: Philip Korta

Publisher: IEEE

Date: Oct. 2017

Copyright © 2017, IEEE

If you're a copyright.com user, you can login to RightsLink using your copyright.com credentials. Already a RightsLink user or want to learn more?

Thesis / Dissertation Reuse

The IEEE does not require individuals working on a thesis to obtain a formal reuse license, however, you may print out this statement to be used as a permission grant:

Requirements to be followed when using any portion (e.g., figure, graph, table, or textual material) of an IEEE copyrighted paper in a thesis:

1) In the case of textual material (e.g., using short quotes or referring to the work within these papers) users must give full credit to the original source (author, paper, publication) followed by the IEEE copyright line © 2011 IEEE.
2) In the case of illustrations or tabular material, we require that the copyright line © [Year of original publication] IEEE appear prominently with each reprinted figure and/or table.
3) If a substantial portion of the original paper is to be used, and if you are not the senior author, also obtain the senior author's approval.

Requirements to be followed when using an entire IEEE copyrighted paper in a thesis:

1) The following IEEE copyright/ credit notice should be placed prominently in the references: © [year of original publication] IEEE. Reprinted, with permission, from [author names, paper title, IEEE publication title, and month/year of publication]
2) Only the accepted version of an IEEE copyrighted paper can be used when posting the paper or your thesis on-line.
3) In placing the thesis on the author's university website, please display the following message in a prominent place on the website: In reference to IEEE copyrighted material which is used with permission in this thesis, the IEEE does not endorse any of [university/educational entity's name goes here]'s products or services. Internal or personal use of this material is permitted. If interested in reprinting/republishing IEEE copyrighted material for advertising or promotional purposes or for creating new collective works for resale or redistribution, please go to http://www.ieee.org/publications_standards/publications/rights/rights_link.html to learn how to obtain a License from RightsLink.

If applicable, University Microfilms and/or ProQuest Library, or the Archives of Canada may supply single copies of the dissertation.

Copyright © 2018 Copyright Clearance Center, Inc. All Rights Reserved. Privacy statement. Terms and Conditions.
Comments? We would like to hear from you. E-mail us at customercare@copyright.com

https://s100.copyright.com/AppDispatchServlet#formTop 1/1

VITA AUCTORIS

NAME:	Philip Korta
PLACE OF BIRTH:	Windsor, ON, Canada
YEAR OF BIRTH:	1994
EDUCATION:	2018: Master of Applied Science in Electrical and Computer Engineering, University of Windsor, Windsor, ON 2016: Bachelor of Applied Science in Electrical and Computer Engineering, University of Windsor, Windsor, ON 2012: St. Anne High School, Windsor, ON